THE EFFECTS OF VIBRONIC COUPLING ON THE PHOTOPHYSICS OF EXCITONS AND POLARONS IN ORDERED AND DISORDERED π-CONJUGATED MOLECULAR AGGREGATES

A Dissertation submitted to

the Temple University Graduate Board

in Partial Fulfillment

of the Requirements for the Degree of

Doctor of Philosophy

by

Christopher Pochas

May 2015

Examining Committee Members:

Professor Frank C. Spano, Advisory Chair, Department of Chemistry

Professor Spiridoula Matsika, Department of Chemistry

Professor Vincent Voelz, Department of Chemistry

Professor Theodore W. Burkhardt, Department of Physics

UMI Number: 3703079

All rights reserved

INFORMATION TO ALL USERS
The quality of this reproduction is dependent upon the quality of the copy submitted.

In the unlikely event that the author did not send a complete manuscript
and there are missing pages, these will be noted. Also, if material had to be removed,
a note will indicate the deletion.

UMI 3703079

Published by ProQuest LLC (2015). Copyright in the Dissertation held by the Author.

Microform Edition © ProQuest LLC.
All rights reserved. This work is protected against
unauthorized copying under Title 17, United States Code

ProQuest LLC.
789 East Eisenhower Parkway
P.O. Box 1346
Ann Arbor, MI 48106 - 1346

©
Copyright
2014

by

Christopher Pochas
All Rights Reserved

ABSTRACT

A theoretical model describing photophysics of π-conjugated aggregates, such as molecular crystals and polymer thin films, is developed. A Holstein-like Hamiltonian expressed with a multi-particle basis set is used to evaluate absorption and photoluminescence (PL) spectra of neutral excitons as well as charge modulation spectra (CMS) and transient absorption spectra (TAS) of positively charges hole-type polarons. The results are used to develop a better theoretical understanding of the organic electronics being studied and their photophysics, and also to probe the morphology of poly(3-hexylthiophene) (P3HT) thin films, which are used in photovoltaic devices.

ACKNOWLEDGMENTS

First I would like to thank the Spano group members for all they have done for me over the years. Prof. Frank Spano encouraged me from my very first day onward, and he has given me every opportunity to succeed during my graduate studies. Next I would like to thank Dr. Hajime Yamagata, who gave so much of his own time and imparted so much of his hard earned knowledge to me, and never asked for anything in return. I couldn't have done it without Haj. Finally I would like to thank Nicholas Hestand, for offering advice and helping me improve my thesis, my defense, my ORP, and just for putting up with me.

Next I would like to thank my lovely girlfriend and soon to be fiance' Danah Al-Awadi. Her consistent love and support over the years was both my inspiration and my motivation to finish my graduate studies and finish them well, so I can be with her.

Last but not least, I would like to thank my family. My mother sacrificed so much for me not just during graduate school but during my entire life, and I can never repay her selflessness and generosity. I'd also like to thank my father, grandmother, and brother for always being supportive and encouraging of my career decisions.

TABLE OF CONTENTS

LIST OF FIGURES

LIST OF TABLES

LIST OF EQUATIONS

CHAPTER 1

INTRODUCTION

1-1 Organic Materials as Electronics Devices

Organic electronics is an emerging technology with enormous potential that is attracting growing interest. The first known organic electronic conductor was a polyacetylene polymer discovered in 1977 by Alan J. Heeger, Alan G. Macdiarmid, and Hideki Shirakawa for which they received the Nobel prize in chemistry.[1] Devices made from this novel class of materials offer several advantages over inorganic materials including higher efficiency (in light emitting devices), and a low cost of raw materials. In general, they can be used for any application in which an inorganic semiconductor can be used, including circuit components such as transistors[3, 9-13], light emitting diodes (LEDs, or OLEDs to specify organic LEDs)[2, 14-17], and photovoltaic cells[18-25]. Additionally, compared to inorganic materials these organic materials are light, flexible, and more easily manufactured since they can be processed in solution and made into films easily with spin casting or other methods.

Along with the great potential of this technology comes a unique set of drawbacks and challenges to be overcome. In many polymer based devices, significant disorder is present in the molecular matrix and takes several forms which tend to have the effect of decreasing the mobility of excitations and the overall efficiency of the device. This is of particular concern for devices made with poly(3-hexylthiophene) (P3HT) which is currently the best known solar absorber and electron donor in organic photovoltaics.[4] Yet many of the properties of the molecular nanostructures of these thin films remain unknown, because they are not immediately apparent from experiments that measure

spectra or electrical currents. Also, X-ray diffraction can only be used to get an average structure, wherein some of the peculiarities of an inhomogeneous phase-like structure of a polymer film which might be crystalline in one place, paracrystalline in another place, and amorphous in yet another place, are lost in the averaging.[26]

As such, a solid theoretical model must be created to be able to interpret the results of experiments which produce an observable, in a way that includes the structure of the molecular matrix of a device, as well as the structure of the excitation in that device. However the nature of these systems is such that an excitation may be delocalized over hundreds of molecules, and so meticulous quantum mechanical methods that seek to account for each individual electron are often not well suited to this kind of problem, because of computational limits. Our model takes a more course-grained approach, wherein only a few electronic states are retained for each chromophore, rather than an approach that accounts for every electron, and every energy level. Our approach does not reveal the finer atomic details of more conventional quantum chemical approaches, but it does allow a reproduction of the salient experimental features by simulating large systems with electronic coupling, vibronic coupling, and disorder.

1-2 π-Conjugated Chromophores

Here we introduce the specific materials of interest that are investigated throughout this writing, as well as the kinds of aggregates they form. They are all organic semiconductors with a π-conjugation network wherein the first electronic excitation is characterized as a π-π^* transition with a transition energy in the optical range (2-3 eV). Because π orbitals are delocalized along all the C-C bonds in the conjugation

network, the π-π^* electronic transition is strongly coupled to the vinyl stretching vibrational transition, usually around 1400 cm^{-1}, and this is the reason why vibronic transitions are observed, rather than pure electronic transitions.

Aggregates formed by these materials are generally classified into one of two categories, J- or H-aggregates. Generally, the absorption and emission spectra undergo significant changes when molecules interact in an aggregated phase. The J- or H- like character is usually expressed in spectral shifts of the aggregate compared to the single molecule, as well as a redistribution of vibronic peak intensities. An important characteristic of H- and J-aggregates is that, in an ideal J-aggregate, the lowest state has the most oscillator strength, while in an ideal H-aggregate, the highest state has the most oscillator strength. As a result, an H-aggregate typically experiences a blueshift in the absorption spectrum relative to the monomer, as well as an attenuation of the 0-0 peak relative to the other peaks, while a J-aggregate, named after E.E. Jelley[31], shows a redshift, and an increased intensity in the 0-0 peak. Mathematically, H or J character is determined by the sign of the coupling between neighbors in a stack of molecules, with a positive coupling leading to an H-aggregate, and a negative coupling leading to a J-aggregate. Many aggregates show a combination of J- and H- characteristics, some of which are the subject of a more detailed study in this writing. See figure 1-1 for energy level diagrams depicting H- and J-aggregation in the simplest possible case, a dimer of parallel molecules.

Figure 1-1

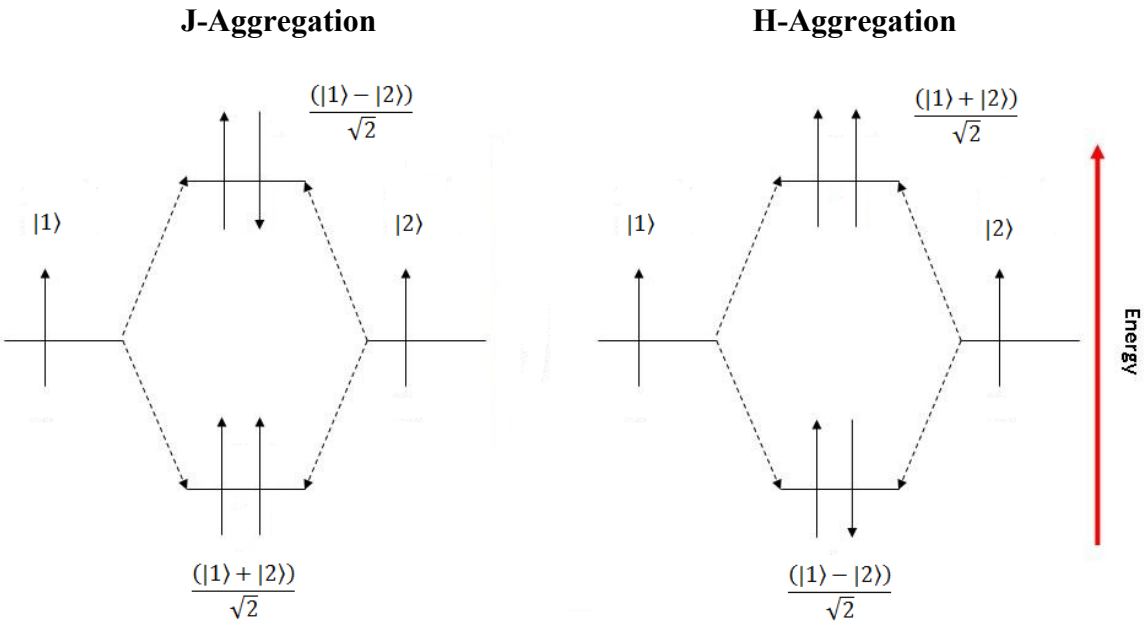

Figure 1-1 depicts the energy level diagrams for a J- and H-aggregate in the case of a dimer. The arrows shown in the diagram represent the orientations of the transition dipole moments of each molecule, before and after allowing the molecules to interact. Intermolecular electronic coupling leads to a splitting of the monomer level into in-phase and out-of-phase states. The optically allowed in-phase state has parallel transition dipoles, while the out of phase state has anti-parallel dipoles. Note that in J-aggregates, the lowest energy state has the most oscillator strength, while the opposite is true in H-aggregation.

The main focus of our small molecule studies were perylene diimide (PDI) complexes. PDI-based chromophores have high quantum yields and well-resolved vibronic spectra and readily self-assemble into a variety of geometries leading to both J- and H-aggregates[32-34], making them ideal chromophores for studying the impact of aggregation on photophysical properties. Covalently linked PDI complexes also display J- and H-aggregate behavior and serve as model systems with which to study charge transport excimer formation, and energy migration.[35-41]

As previously mentioned, P3HT is another π-conjugated chromophore of particular importance.[4] On the nanoscale, it can form various structures which may also exhibit both H- and J- like behavior.[42] When made into thin films, P3HT forms long-range disordered amorphous structures with some highly crystalline short-range regions called π-stacks[26]. P3HT is strongly emissive but is best known for its role in high performance photovoltaic cells[18-25]. Several conditions are known to affect the material properties and spectral line shapes, such as the solvent used, the processing method (spin cast, cooled in solution, etc), and the regioregularity of the alkyl side chains.[22, 23, 27] See figure 1-2 for the molecular structures of PDI and P3HT.

Figure 1-2

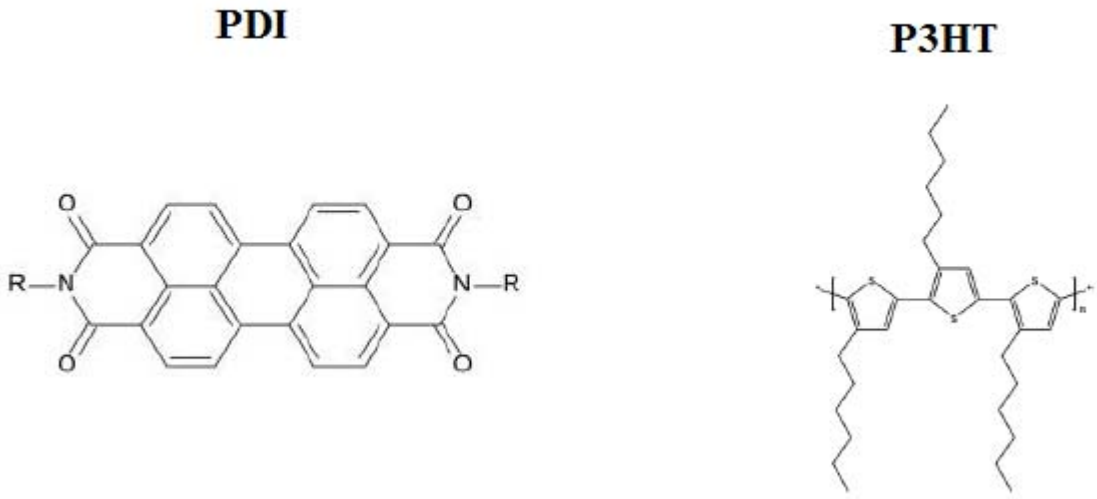

Figure 1-2. the 2 organic semiconductor materials most studied in this writing, with PDI on the left, and P3HT on the right.

1-3 Single Excitation Holstein Hamiltonian and its Applications

In this section we introduce the model used predominantly throughout the rest of this writing. Though it is often modified from the version presented here, the modifications are usually minor and specific to a system, implemented in order to account for the unique properties of that system. Throughout the work presented here, a Holstein Hamiltonian is employed with a basis set consisting of a single electronic excitation, (a neutral exciton or a charge) with the possibility of one or more vibrational excitations. The basis set consists of one- and two- particle states wherein a one-particle state consists of an electronic excitation on a site that may or may not be additionally vibrationally excited, while a two particle state consists of the same (a vibronically excited molecule), plus another vibrational excitation on a chromophore that is in the electronic ground state. We use a canonical ensemble, in which the number of chromophores and electronic excitations is constant. This simple model, with only one excitation, nearest neighbor coupling, and a straightforward vibronic coupling from the Holstein Hamiltonian, is very robust and versatile and is readily used for a wide range of applications, from small disorder free systems, to large disordered multidimensional systems.[28-30, 42]

The site based Holstein Hamiltonian model employed herein assumes nuclear potentials for molecular vibrations in the ground (S_0) and excited (S_1) electronic states. These potentials are shifted harmonic wells of identical curvature. In the vector subspace containing a single electronic excitation within an aggregate of N chromophores, the general form of the Hamiltonian is as follows:

$$H = \hbar\omega_0 \sum_n b_n^\dagger b_n + \hbar\omega_0 \lambda \sum_n (b_n^\dagger + b_n)|n\rangle\langle n| + \sum_{m,n} J_{mn}|m\rangle\langle n| + \hbar\omega_0 \lambda^2$$

(1-1)

The first term represents the vibrational energy, with the operators $b_n^\dagger$ and b_n, respectively creating and annihilating vibrational excitations on the *n*th chromophore. The vibrational mode is taken to be the symmetric vinyl stretching mode with $\hbar\omega_0$= 1400 cm^{-1}. The Huang-Rhys factor λ^2 represents the shift along a vibrational coordinate axis between the ground and excited state harmonic wells, and can usually be derived from the absorption spectrum of a single chromophore. The second term represents the linear vibronic coupling, and the third term represents the electronic coupling with |n> indicating a state wherein the nth chromophore is excited and all other chromophores are in the ground state. J_{mn} represents the electronic coupling between chromophores m and n, which is usually taken to be zero unless m and n are nearest neighbors.

The basis set used to represent H in eq 1-1 consists of the so-called single- and two-particle states. In a single-particle state, denoted as |n, ṽ>, the nth chromophore is electronically excited with ṽ vibrational quanta in its shifted potential well. The remaining N − 1 chromophores are in their vibrationless ground states. In a two-particle state, denoted |n, ṽ; n′, v′ >, chromophore n is electronically excited with ṽ excited-state vibrational quanta, while molecule n′ is vibrationally excited with v’ > 0 vibrational quanta in the shifted potential. The remaining N − 2 chromophores are in their vibrationless ground states. Three-and higher- particle states for complexes with three or

more chromophores can also be included, but their impact is negligible. The αth eigenstates of H in eq 1-1 can then be expanded as

$$|\Psi^{\alpha}\rangle = \sum_{n,\tilde{\nu}} c_{n,\tilde{\nu}}^{(\alpha)} |n,\tilde{\nu}\rangle + \sum_{n,\tilde{\nu}} \sum_{n',\nu'} c_{n,\tilde{\nu};n',\nu'}^{(\alpha)} |n,\tilde{\nu};n',\nu'\rangle \tag{1-2}$$

We have applied this Hamiltonian and basis set to a wide range of problems presented in this writing. It was used to calculate the eigenstates, absorption, and emission spectra of a Frenkel exciton in a small aggregates of covalently linked perylene diimide (PDI) chromophores. In these systems, *ab initio* type quantum chemistry methods were used to calculate the couplings J_{mn}. Because the PDI complexes exhibit very low disorder, these systems were useful in showing just how quantitatively accurate the model used herein can be, when the parameters of the system are well known to the theorist. However, when microscopic properties are unknown, and disorder is present in the system of interest, the problem becomes more challenging. This is demonstrated in the second half of this thesis, wherein we examine the charge modulation spectra (CMS) of hole-type polarons in poly(3-hexylthiophene) (P3HT) films which are known to be both good absorbers and electron donors in organic photovoltaic cells,[18-22] but P3HT films are also known to be rather disordered at the molecular level in real systems.[26] These systems were useful for showing how our model can be used to gain insight into the nanostructure of the polymer matrix, as well as the electronic structure of the polaron in it, both of which are not immediately apparent from the spectra produced in experiments.

For example, by studying a chiral PDI dimer using the Holstein Hamiltonian,

we were able to identify both H-aggregate and J-aggregate behavior at the same time, based on the polarization of absorbed light. Because of the transition dipoles of the chromophores, which are related via a C_2 rotation, are not parallel, the aggregate is neither fully H-like nor fully J-like and so it displays Davydov splitting, where the polarized components of the absorption spectrum exhibit either pure H- or pure J-like properties (See figure 1-3 from Ref. 28).

Figure 1-3

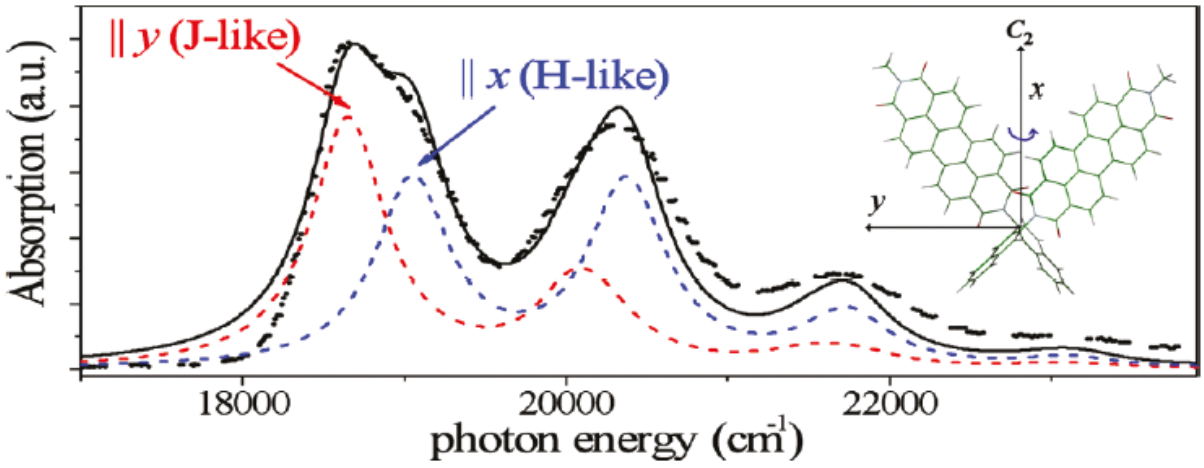

Figure 1-3. Calculated unpolarized absorption spectrum (black) and components polarized along the x axis (blue) and y axis (red). The measured spectrum from ref 8 is also shown (black dots). Parameters used in the calculation: $J_{12} = 371\ cm^{-1}$, $\lambda^2 = 0.57$, $\omega 0 = 1400\ cm^{-1}$ and $\omega_{0\text{-}0} + D = 18900\ cm^{-1}$ (D = _100 cm^{-1}). The line shape used is Lorentzian with fwhm =0.4ω0. In the inset, the line shape is Gaussian with full width (1/e) = $0.4\omega_0$.

This dual behavior is readily understood by considering that, because the system is a dimer, the electronic eigenstates consist of two states that are either symmetric or anti-symmetric with respect to C_2 rotation. The symmetric (J-like) eigenstates are redshifted relative to monomer absorption, while the anti-symmetric (H-like) eigenstates are

blueshifted relative to monomer absorption, and this pattern is repeated in each vibronic band (see Figure 1-4).

Figure 1-4

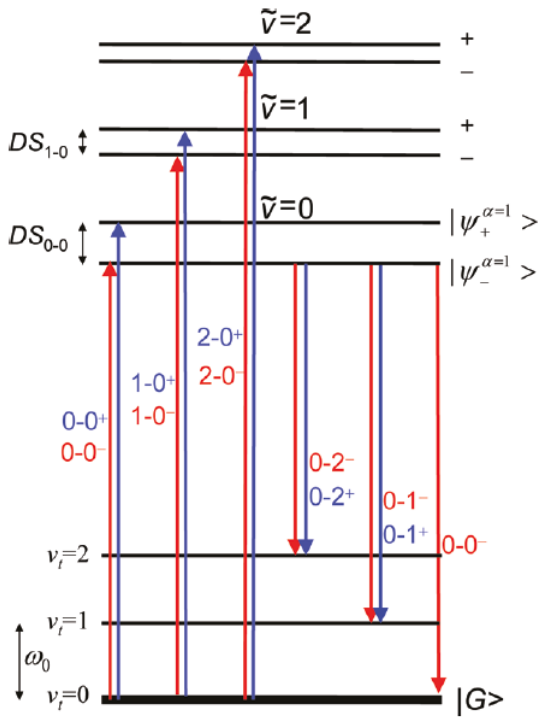

Figure 1-4. Energy level diagram for PDI_2 in the limit of weak excitonic coupling and low temperature showing absorption transitions (left) and emission transitions (right). Blue (red) transitions are x- (y-) polarized. Energy level ordering is consistent with $J_{12} > 0$. Only ground and excited electronic levels with two or fewer vibrational quanta are shown. Note that the optical gap is not to scale.

In this way, the reproduced spectrum is useful as evidence that the underlying model is correct, and it produces the correct vibronic eigenstates to describe the system,

so we can use it to gain insight into both the structure of the aggregate itself, as well as the structure of the excitation within it.

This line of work was continued with a series of small PDI aggregates of some very basic and fundamental structures, in order to understand the structure of the vibronic eigenstates in these more complex systems.[29] These aggregates are divided into a linear series consisting of a dimer, trimer, and tetramer, and a star-shaped symmetric series including a dimer, trimer, and tetramer (See Figure 1-5). Although there was no experimental data for a linear tetramer, it was simulated with the theory presented here.

Figure 1-5

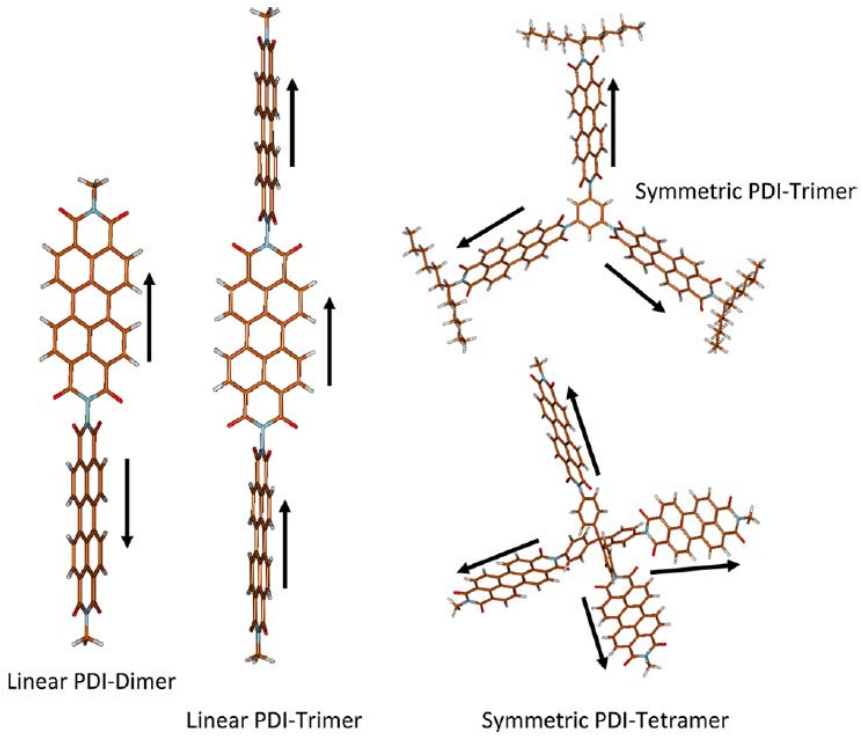

Figure 1-5. Geometry-optimized PDI complexes considered in this work. Also shown is our adapted phase convention, as indicted by the directions of the PDI transition dipole moments. Note that the symmetric tetramer is in a "caltrop" like geometry, reminiscent of a sp3 hybrid orbital.

A good deal of insight about these complexes and their spectra can be gained by applying the Holstein Hamiltonian to these aggregates, while using an exciton site-basis without vibrations, and nearest neighbor coupling. When our model is applied with the appropriate inter-chromophore couplings, the following series of eigenstates and eigenenergies is produced (See figures 1-6 and 1-7). Keep in mind that absorption occurs from a ground state common to all these systems, not shown in figures 1-6 and 1-7.

Figure 1-6

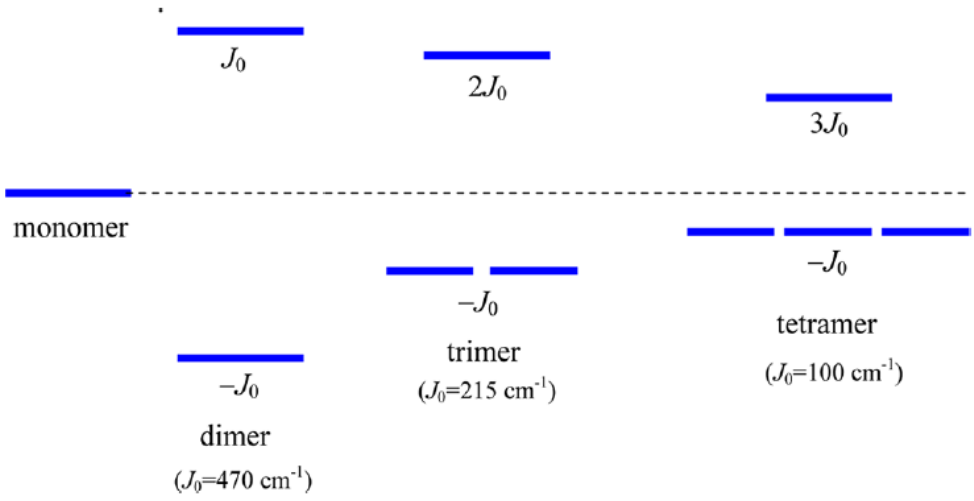

Figure 1-6. Exciton energy levels in the symmetric series of chromophores in the absence of vibronic coupling. For the dimer, trimer, and tetramer, the lower states are optically allowed from the ground state, while the upper state is optically forbidden. Generally, a symmetric N-mer has N−1 degenerate bright states at the band bottom. The unique coupling J_0 is evaluated numerically (see chapter 2) and is positive with our chosen phase convention. Note that the exciton bandwidth, NJ_0, decreases with increasing N.

Figure 1-7

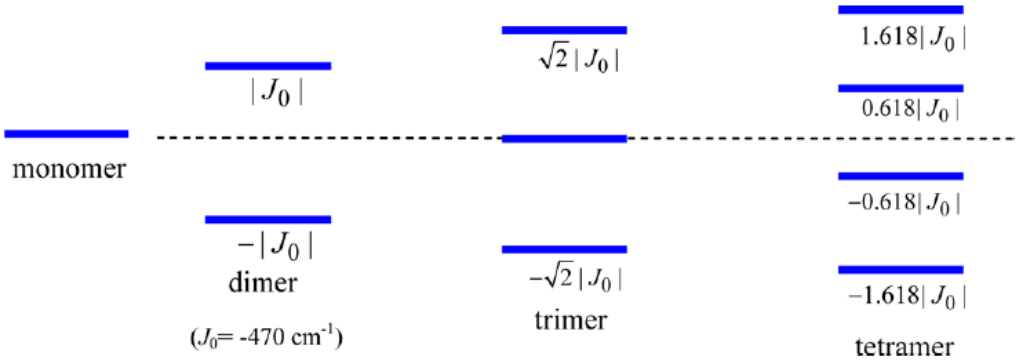

Figure 1-7. Exciton energy levels in the linear series of chromophores assuming nearest-neighbor-only coupling equal to J_0 and no vibronic coupling. Unlike the symmetric series, the value of J_0 remains constant throughout the series and the red shift of the lowest energy exciton increase with N. Consistent with our chosen phase convention for linear complexes, J_0 is negative (see chapter 2). In all cases the lowest energy exciton is the most strongly allowed

These energy level diagrams, without vibrations in the basis states is useful for predicting the position of the 0-0 peak in real absorption spectra, but it obviously fails to account for the positions and intensities other vibronic bands. The positions of the vibronic bands in the spectra are important, because they tell us about the H- or J- like structure of the aggregate, while the relative intensities of the vibronic peaks give information about the spatial coherence of the exciton[30]. This information can be obtained from obtaining a full numerical solution that uses the Hamiltonian of equation 1 and the basis set of equation 2. When the full numerical model is applied to these systems, spectra are generated that reproduce experiments remarkably well (see figure 1-8).

Figure 1-8

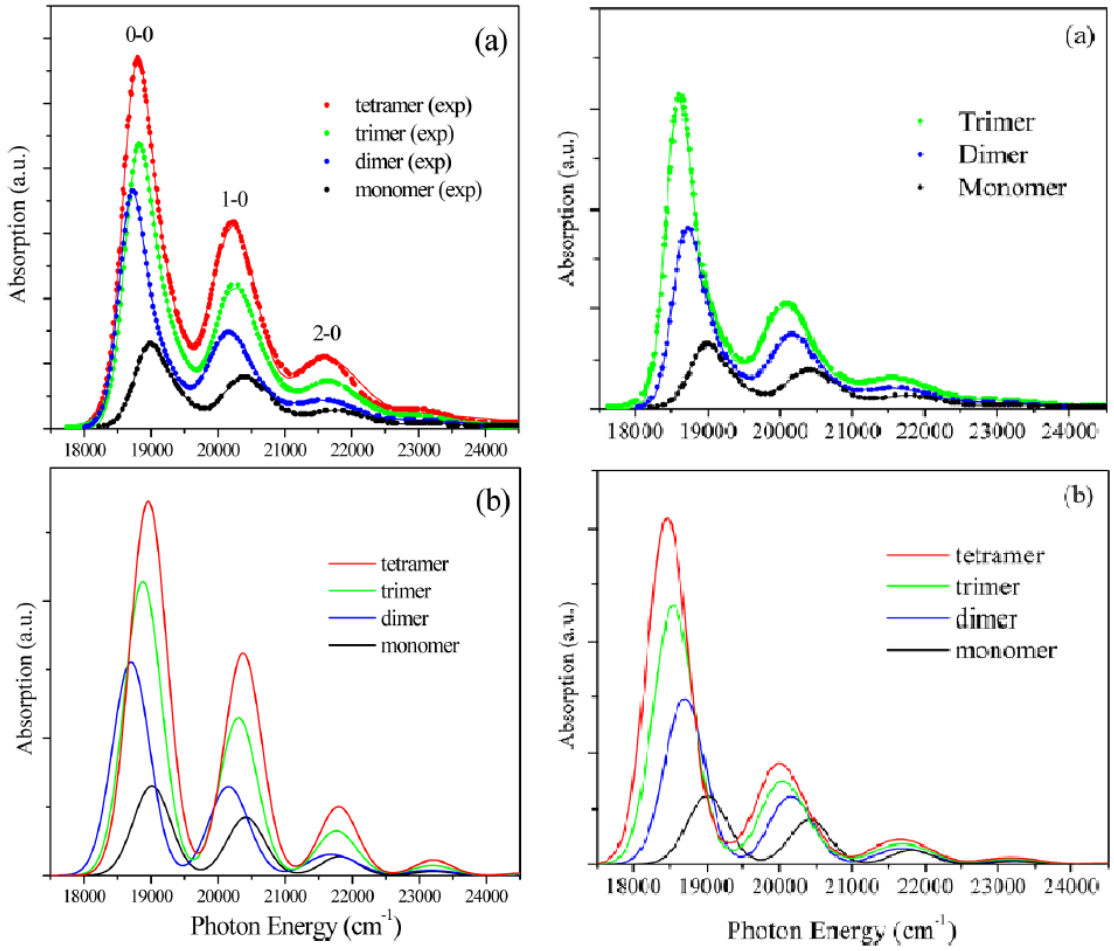

Figure 1-8. (a) Measured (dots) and fitted (lines) absorption spectra of the symmetric (left) and linear (right) series of PDI complexes. (b) Calculated spectra using a Gaussian line shape in eq 11 with a full width (at the 1/e point) of 800 cm^{-1} (see text for details).

With the degree of accuracy exhibited in these spectra, we were able to move on to larger, more complex, more disordered systems with confidence that the underlying model is quantitatively correct. Particularly, the complex systems of most interest to us are organic photovoltaic cell materials. P3HT is used in the most efficient organic solar

cells known today, and so a study in to the charge transport properties of P3HT, and the spatial coherence of polarons in P3HT are of particular interest. We found that charge modulation spectra (CMS) are a good probe for coherence lengths in P3HT, and can even be used to resolve inter-chain and intra-chain coherence separately. It also serves as a good observable for testing the accuracy of our model.

CMS, as used in the experiments cited below, is a technique whereby positively charged hole-type polarons are generated in a film of P3HT either by illumination with EM radiation or by applying a voltage across the film. These polarons are mobile and readily absorb low energy photons (IR-microwave) to generate a CMS spectrum. See figure 1-9 below for two selected CMS spectra, one of a high molecular weight P3HT film, and the other of low molecular weight.

Figure 1-9

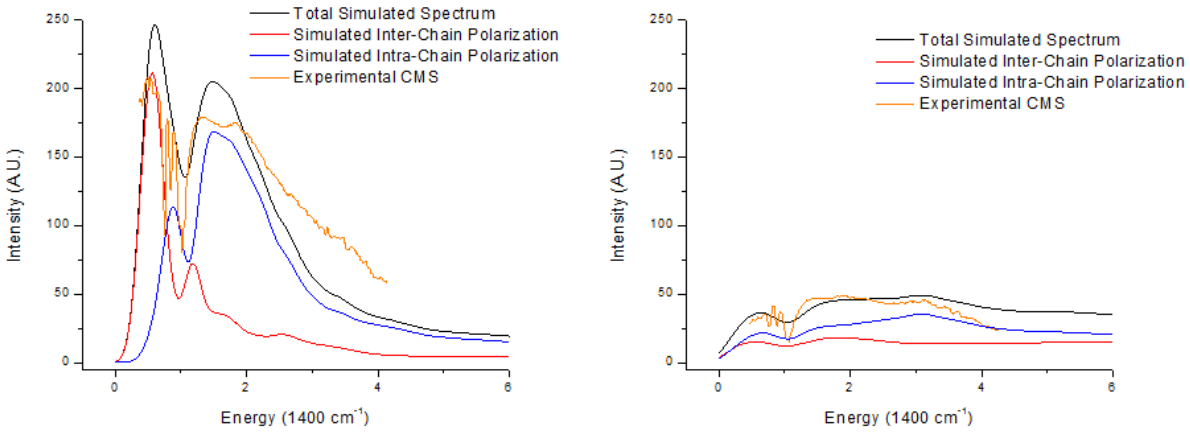

Figure 1-9. Orange curves correspond to the experimental CMS of the Sirringhaus Reference for high (37kD, left) and low (15kD, right) MW P3HT films spin cast from trichlorobenzene. Black curves are calculated absorption spectra for 2 dimensional 5x5 π-stacks (5 thiophene repeat units by 5 chains), while red and blue curves are the inter- and intra-chain polarizations, respectively. For the high MW spectrum, t_{inter} = -.15 eV and t_{intra} = -.36 eV. The homogeneous line width is .018 eV. For the low molecular weight

spectrum, t_{inter} = -.15 eV and t_{intra} = -.26 eV, and the homogeneous linewidth is .03 eV. In both low and high MW spectra, ω_{vib} = .174eV/$\hbar$ and λ^2 = 1. Two thousand randomly generated disorder configurations were averaged together to create the spectra (see chapter 4 for disorder details).

Using the parameters that produced these CMS, we were able to produce coherence functions of 2-dimensional polarons in the P3HT π-stacks. These functions indicate the extent of spatial coherence of the polaron, i.e. the length over which the polarons maintain wave-like motion. Coherence lengths are of great interest in organic electronics[30] because the mobility of excitations is directly related to the coherence length. In this way, we show that CMS is a means of probing the coherence lengths, since a greater intensity in the CMS spectrum indicates a greater mobility for the polarons therein, and a larger spatial coherence length. Furthermore, because intrachain coupling is higher than interchain coupling in P3HT π-stacks, the low energy peak in these CMS indicate the interchain coherence length, while the broader high energy peak indicates the intrachain coherence length, as is indicated by the polarized components of the spectra. So not only is CMS a probe of the coherence length of hole-type polarons in P3HT, it also has directional sensitivity. The coherence functions for the two P3HT films are presented below in figure 1-10.

Figure 1-10

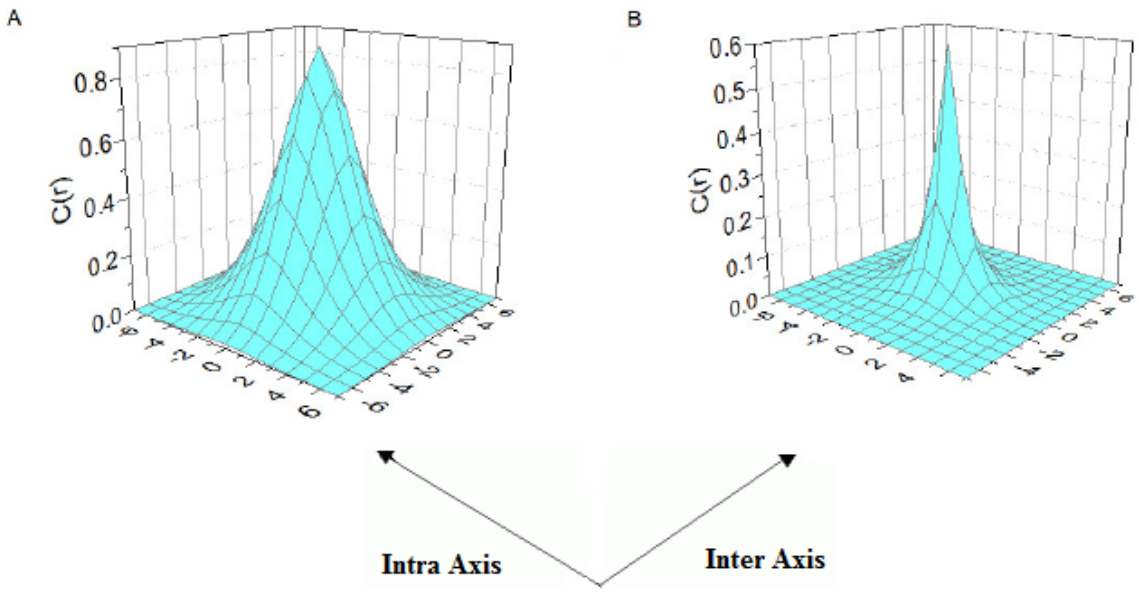

Figure 1-10 depicts the coherence function of a hole in a high MW, 37 kiloDaltons(KD), and low disorder system. Its interchain and intrachian coherence numbers are 6.22 and 5.66, respectively. Figure 2B depicts the coherence function of a hole in a high MW, 15 KD, and high disorder system. Its interchain and intrachain coherence numbers are 2.22 and 2.83, respectively.

All of the aforementioned materials and applications are explored in full detail in the following chapters, along with additional systems and models not mentioned here for the sake of brevity. In the next chapter, the bichromophore of Figure 1-3 is explored in greater detail. The sophisticated method for calculating the Coulombic coupling, which is a great improvement over the simple dipole-dipole approximation, is explored in detail, as is the full vibronic modelling of the PDI bichromophore.

REFERENCES

1. Shirakawa, H., et al., Journal of the Chemical Society-Chemical Communications, **1977**(16): p. 578-580.

2. Burroughes, J.H., et al., Nature, 1990. **347**: p. 539-541.

3. Sirringhaus, H., et al., Nature, 1999. **401**(6754): p. 685-688.

4. Coakley, K.M. and M.D. McGehee, Chemistry of Materials, 2004. **16**(23): p. 4533-4542.

5. Scholes, G.D. and G. Rumbles, Nature Materials, 2006. **5**(9): p. 683-696.

6. Heeger, A.J., Chemical Society Reviews, 2010. **39**(7): p. 2354-2371.

7. Bredas, J.-L., et al., Acc. Chem. Res., 2009. **42**(11): p. 1691-1699

8. Malliaras, G. and R.H. Friend, Physics Today, 2005. **58**(5): p. 53-58.

9. Bao, Z., A. Dodabalapui, and A.J. Lovinger, Appl. Phys. Lett., 1996. **69**: p. 4108-4110.

10. Sirringhaus, H., N. Tessler, and R.H. Friend, Science, 1998. **280**: p. 1741-1744.

11. Tsumura, A., H. Koezuka, and T. Ando, Appl. Phys. Lett., 1986. **49**: p.1210-1212.

12. Zen, A., et al., Adv. Funct. Mater., 2004. **14**: p. 757-764.

13. Bao, Z., Adv. Mater., 2000. **12**: p. 227-230.

14. Mullen, K. and U. Scherf, eds. 2006, Wiley: New York.

15. Friend, R.H., et al., Nature, 1999, **397**: p. 121-128.

16. Z.H. Kafafi Proceedings of SPIE. 2002, **4464** Washington: Society of Photo-optical Instrumentation Engineers.

17. Adachi, C., et al., J. Appl. Phys., 2001. **90**: p. 5048-5052.

18. Liang, Y.Y. and L.P. Yu, Accounts of Chemical Research, 2010. **43**(9): p. 1227-1236.

19. Yu, G., et al., Science, 1995. **270**: p. 1789-1791.

20. Yang, X. and J. Loos, Macromolecules, 2007. **40**(5): p. 1353-1362.

21. Granstrom, M., et al., Nature, 1998. **395**: p. 257-260.

22. Kim, Y., et al., Nature Materials, 2006. **5**(3): p. 197-203.

23. Kim, J.Y., et al., Science, 2007. **317**(5835): p. 222-225.

24. Brabec, C.J., Solar Energy Materials and Solar Cells, 2004. **83**(2-3): p. 273-292.

25. Brabec, C.J., et al., 2003, Heidelberg: Springer.

26. Stingelin, N., et al., 2014, **47** (19), pp 6730–6739

27. Niles, E.T., et al., J. Phys. Chem. Lett., 2012. **3**(2): p. 259-263.

28. Kistler, K.A.; Pochas, C.M.; Yamagata, H.; Matsika, S.; Spano, F.C. Journal of Physical Chemistry B, 2012, **116** (1): p. 77-86

29. Pochas, C.M.; Kistler, K.A.; Yamagata H.; Spano, F.C. Journal of The Amercian Society, 2013, **135**, 8, p. 3056-3066.

30. Spano, FC.; Yamagata, H. Journal of Physical Chemistry B, 2011, **115** (18) p. 5133-5143.

31. Jelley, E.E, Nature, 1936 **138**, p. 1009-1010.

32. Kaiser, T. E.; Stepanenko, V.; Wurthner, F. J. Am. Chem. Soc. 2009, **131**, p. 6719-6732.

33. Ghosh, S.; Li, X.-Q.; Stepanenko, V.; Wurthner, F. Chem.—Eur. J. 2008, **14**, p. 11343–11357.

34. Shaller, A. D.; Wang, W.; Gan, H. Y.; Li, A. D. Q. Angew. Chem., Int. Ed. 2008, **47**, p. 7705–7709.

35. Rybtchinski, B.; Sinks, L. E.; Wasielewski, M. R. J. Phys. Chem A 2004, **108**, p. 7497.

36. Veldman, D.; Chopin, S. M. A.; Meskers, S. C. J.; Groeneveld, M. M.; Williams, R. M.; Janssen, R. A. J. J. Phys. Chem A 2008, **112**, p. 5846.

37. Giaimo, J.M.; Lockard, J. V.; Sinks, L. E.; Scott, A. M.;Wilson, T. M.; Wasielewski, M. R. J. Phys. Chem. A 2008, **112**, p. 2322.

38. Schlosser, F.; Sung, J.; Kim, P.; Kim, D.; Wurthner, F. Chem. Sci. 2012, **3**, p. 2778.

39. Montgomery, N. A.; Hedley, G. J.; Ruseckas, A.; Denis, J.-C.; Schumacher, S.; Kanibolotsky, A. L.; Skabara, P. J.; Galbraith, I.; Turnbull, G. A.; Samuel, I. D. W. Phys. Chem. Chem. Phys. 2012, **14**, p. 9176.

40. Metivier, R.; Nolde, F.; Mullen, K.; Basche, T. Phys. Rev. Lett. 2007, **98**, p. 047802.

41. Yoo, H.; Furumaki, S.; Yang, J.; Lee, J.-E.; Chung, H.; Oba, T.; Kobayashi, H.; Rybtchinski, B.; Wilson, T. M.; Wasielewski, M. R.; Vacha, M.; Kim, D. J. Phys. Chem. B 2012, **116**, p. 12878.

42. Yamagata, H., & Spano, F. J. Chem Phys. 2012, **136**(18), p. 184901.

CHAPTER 2

ABSORPTION, CIRCULAR DICHROISM, AND PHOTOLUMINESCENCE IN PERYLENE DIIMIDE BICHROMOPHORES: POLARIZATION-DEPENDENT H- AND J-AGGREGATE BEHAVIOR

2-1 Introduction

The classification of J- versus H-aggregates, developed many decades ago largely through the efforts of Kasha and co-workers,[1-3] was a key development in understanding the relationship between morphology and photophysical function in molecular assemblies. Electronic interactions between molecules induce delocalized excited states, or Frenkel excitons, which are identified through a red shift (blue shift) of the main absorption peak in J- (H-) aggregates compared to isolated molecules in solution. Radiative properties are also affected quite differently in the two aggregate types: In J- (H-) aggregates, the symmetry of the lowest-energy exciton dictates enhanced (depressed) radiative decay rates relative to the monomer.

The aggregation-induced shift in the absorption spectrum is not always a reliable indicator of J- or H-aggregation. In the case of weakly coupled H-aggregates, the excitonic blue shift can easily be dominated by a much larger red shift due to nonresonant interactions,[4] the so-called gas-to-crystal shift. In polymer H-aggregates, the red shift due to the enhanced planarization of the polymers within an aggregate can also dominate the weak blue shift, as happens in poly(3-hexylthiophene) thin films.[5,6] Moreover, J versus H assignments based on radiative decay rates are not straightforward: The radiative decay rate must be disentangled from nonradiative rates, which often requires rather delicate measurements of the temperature-dependent absolute quantum yield.

Fortunately, additional spectral signatures for J- and H-aggregates can be identified from the way vibronic coupling in molecules is altered by intermolecular interactions.[7] In many aggregate-forming dye molecules and π-conjugated molecules in general, the main $S_0 \rightarrow S_n$ electronic transitions are coupled to the symmetric vinyl stretching mode (or cluster of modes) with frequencies near 1400 cm^{-1}, resulting in pronounced vibronic progressions in the absorption and photoluminescence (PL) spectra. In aggregates, additional signatures arise from the opposing manners in which the progression is distorted upon H- or J-aggregation, as outlined in Ref. 7. Briefly, the ratio of the oscillator strengths of the first two vibronic peaks in the absorption spectrum, I_A^{0-0}/I_A^{1-0}, increases (decreases) in J- (H-) aggregates relative to the monomer. In the PL spectrum, the line strength ratio, $I_{PL}^{0-0}/I_{PL}^{0-1}$, decreases (increases) with increasing temperature and increasing disorder in J- (H-) aggregates. Although these properties are strictly valid in ideal aggregates containing one moecule per unit cell, we show in this article how they are modified when there are two molecules per unit cell. We focus on a simple dimer complex in which the two molecules are related by a C_2 rotation. Our results can be directly applied to the popular herringbone packing lattices adopted by many organic chromophores, where the two molecules in a unit cell are related by a 2-fold screw rotation or glide plane translation.

In this chapter, we analyze in detail the absorption, circular dichroism (CD), and PL spectra of a chiral perylene diimide (PDI) complex consisting of two PDI chromophores covalently bonded through a naphthalene bridge.[8] PDI chromophores have been extensively studied because of their near-unit quantum yields and their ability to readily self-assemble in a variety of geometries leading to both J- and H-aggregates,

depending mainly on the attached side groups.[9-11] There has also been significant interest in covalently linked PDI complexes(citations) and PDI/DNA complexes.[8, 12-17] Theoretical analysis of the impact of vibronic coupling on the absorption spectrum of molecular dimers began with the work of Witkowski[21] and Fulton and Gouterman.[22, 23] The CD spectrum of dimers was originally treated by Weigang.[24, 25] Several recent theoretical works have successfully described many of the salient features of the absorption and emission spectral line shapes of PDI dimers[26-29] and crystals based on perylene derivatives,[30-31] including the effects of vibronic coupling.

For packing arrangements with one molecule per unit cell, the I_A^{0-0}/I_A^{1-0} ratio is primarily determined by the Huang_Rhys (HR) factor corresponding to the vinyl stretching mode and the free exciton bandwidth, W, which measures the strength of the intermolecular couplings. The HR factor is easily obtained from the absorption spectrum of the monomer in solution. Hence, from the measured value of I_A^{0-0}/I_A^{1-0}, one can readily deduce W. This method was successfully applied to determine the exciton bandwidth in polythiophene π-stacks.[5, 6]

In packing arrangements with two molecules per unit cell, oscillator strength is generally deposited at the top and bottom of the exciton bands, giving rise to the two Davydov components in the absorption spectrum.[32-33] The two components are polarized differently, and each one yields a separate value for I_A^{0-0}/I_A^{1-0}. As we show herein, the vibronic progression corresponding to the lower-energy Davydov component is identical to that of an ideal J-aggregate, with I_A^{0-0}/I_A^{1-0} increasing with W, whereas the vibronic progression corresponding to the higher-energy Davydov component is identical to that of an ideal H-aggregate, with I_A^{0-0}/I_A^{1-0} decreasing with W. Although measuring

the individual polarized components for a PDI complex in solution is not possible because of the isotropic distribution of molecular orientations, in a fixed crystalline lattice, such as the herringbone lattice, it is possible. The PL spectrum for aggregates with two molecules per unit cell generally contains both polarization components: a J-like component in which the 0-0 emission is allowed and an H-like component in which the 0-0 emission is absent (as long as the symmetry is preserved, i.e., there is no disorder). We have recently shown that the ratio of the line strengths of the first two vibronic peaks, $I_{PL}^{0-0}/I_{PL}^{0-1}$, in the J-like component provides a direct measure of the exciton coherence number.[47]

The more conventional way of determining W from the absorption spectrum is directly from the Davydov splitting (DS). However, in packing arrangements with one molecule per unit cell, there is no DS (as one component carries no oscillator strength), making the ratio method a more robust technique for obtaining W. In the PDI bichromophore in the present study, the two PDI molecules are almost at right angles to each other. Hence, this system presents a unique opportunity to evaluate the two methods for obtaining W. We also compare the values of W extracted from the absorption spectrum with the value computed using a novel transition charge density technique.

2-2. Absorption in PDI Complexes

We begin by reviewing the salient features of the absorption and CD spectra of the naphthalene-bridged PDI_2 bichromophore shown in Figure 2-1. The solution-phase spectra of the PDI monomer (with 1-hexylheptyl end groups) and the PDI_2 complex from (citation) are reproduced in Figure 2-2. The spectra derive from the electronic $S_0 \rightarrow S_1$

transition and are characterized by a pronounced vibronic progression due to the vinyl stretching mode with frequency $\hbar\omega_0 \approx 0.17$ eV (1400 cm^{-1}). In the monomer, the vibronic peaks are labeled as 0←0, 1←0, 2←0, and so on (abbreviated as 0-0, 1-0, 2-0, etc.) in order of increasing energy. The monomer absorption spectral line shape is well-described using an expression based on shifted S_0 and S_1 nuclear potential wells of identical curvature,

$$A_{mon}(\omega) = \sum_{n=0,1,2,\ldots} \frac{e^{-\lambda^2}\lambda^{2n}}{n!} W_{LS}(\omega - \omega_{0-0} - n\omega_0)$$

(2-1)

where ω_{0-0} is the solution-phase 0-0 transition energy and the prefactors of the line shape function W_{LS} are the familiar Franck-Condon factors. The HR factor λ^2 that best reproduces the relative vibronic intensities in the measured (solvated) PDI spectrum is $\lambda^2 \approx 0.57$.

Figure 2-1

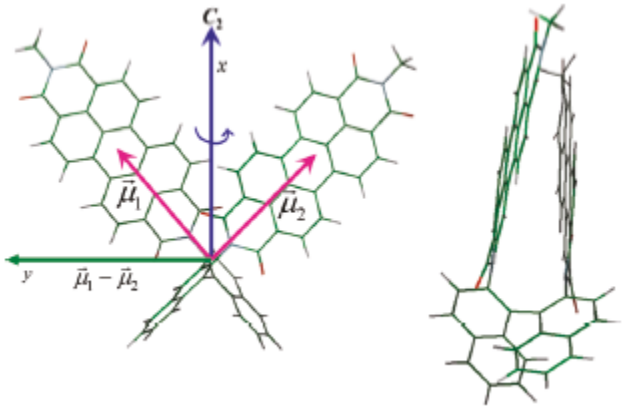

Figure 2-1. Structure of PDI_2, optimized at the PM3 level, from two side views. The C_2 axis is shown as a blue arrow in the left view, along with the two PDI transition dipoles, $\vec{\mu}_1$ and $\vec{\mu}_2$, shown as magenta arrows,

and the , $\vec{\mu}_1$ - $\vec{\mu}_2$ vector, shown as a green arrow. ($\vec{\mu}_1$ + $\vec{\mu}_2$ coincides with the C2 axis or x axis). The angle between $\vec{\mu}_1$ and $\vec{\mu}_2$ is approximately $\phi = 86°$

Figure 2-2

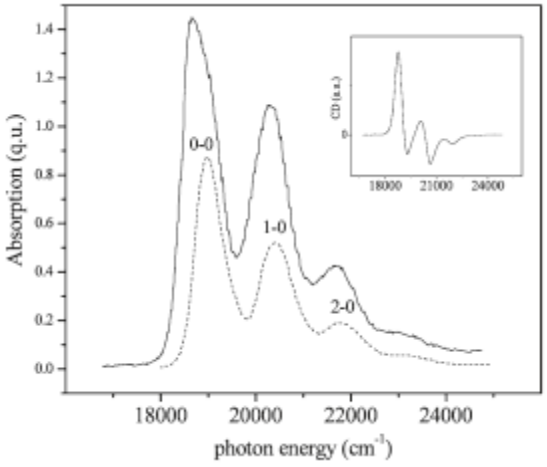

Figure 2-2. Measured absorption spectra for the PDI monomer (dotted) and the PDI_2 complex of Figure 9 in chloroform from ref 8. Inset: Measured CD spectrum for the right-handed PDI_2 complex.

The PDI_2 complexes show quite different spectra. Although the concentrations of the monomer and dimer complex were taken to be equal in Figure 2-2, the dimer complex is clearly not simply twice the monomer spectrum. First, the relative vibronic intensities are different; for example, the dimer complex would require an effective HR factor of roughly 0.76 to account for the relative intensities of the first two peaks. In addition, there is a clear shoulder on the blue side of the first main absorption peak due to the Davydov splitting caused by the excitonic interactions between the two chromophores.

The CD spectrum, also reproduced from Ref. 8, is shown in the inset of Figure 2-2. The spectrum also displays significant vibronic activity and corresponds to the right-handed enantiomer. The vibronic peaks can be crudely described as a series of bisignate

peaks and reflect the presence of substantial excitonic coupling between the PDI chromophores.

2-3 Model

In this section, we introduce the Hamiltonian for PDI_2, which treats each PDI molecule as an individual chromophore within a through-space coupled dimer, that is, a Frenkel dimer. Each chromophore is taken to be an electronic two-level system coupled to a symmetric intramolecular vibration of frequency ω_0. The nuclear potentials corresponding to the ground (S_0) and excited (S_1) states are taken to be harmonic, with the S_1 well shifted with respect to the S_0 well, leading to the nuclear relaxation energy $\hbar\lambda^2\omega_0$.

The PDI_2 Hamiltonian employed in this work is the Holstein-like Hamiltonian.[35] For the subspace containing one singlet excitation, H reads

$$H = \omega_0 \sum_{n=1}^{2} b_n^\dagger b_n + \omega_0 \lambda \sum_{n=1}^{2} (b_n^\dagger + b_n) \, |n\rangle\langle n| + J_{12}(|1\rangle\langle 2| + |2\rangle\langle 1|) + D + \omega_{0-0} + \omega_0 \lambda^2 \tag{2-2}$$

where $\hbar = 1$ is taken. $b_n^\dagger(b_n)$ is the creation (destruction) operator corresponding to the symmetric vibration on chromophore n. The pure electronic state, $|n\rangle$, indicates that chromophore n (=1, 2) is electronically excited to the state S_1 while the other chromophore remains in its electronic ground state, S_0. In eq 2-2, the first term represents the vibrational energy, and the second term represents the local linear exciton-vibrational (EV) coupling. The third term represents the excitonic coupling between the two PDI

chromophores. Finally, D denotes the nonresonant interaction between the two chromophores.

The excitonic coupling, J_{12}, between two chromophores can be theoretically well-approximated by the Coulombic interaction between their monomeric transition densities. Although such a calculation would provide accurate interchromophore coupling, less computationally expensive approximations, especially with aggregate systems of large chromophores, are of practical interest. The simplest approximations, such as the point-dipole approximation, where the coupling is based on the interaction of the monomeric transition dipoles, break down for interchromophore distances on the order of the length of the chromophore and lack much of the spatial character of a full transition density. In an effort to capture much of that spatial character while maintaining computational efficiency, we used a method in which Mulliken population analysis (MPA) is applied to the monomeric transition density of the bright $\pi\pi^*$ excited state (S_1) for each PDI. Here, the monomeric transition density is derived from a single-reference excited-state calculation using time dependent density functional theory (TDDFT), by expanding the excited-state wave function in terms of its single-excitation Slater determinants and their corresponding configuration interaction (CI) coefficients. This has been done recently for carbon nanotubes within the TDDFT regime,[36] although the transition densities from other single-excitation excited-state methods have also been used.[36-39] The MPA analysis of the transition density decomposes the density to point charges, q^t, located at the atomic positions of the chromophore, much as applying MPA to the ground-state density gives partial atomic charges for the ground state molecule. Within the MPA framework, the q^t values (in atomic units) are calculated as

$$q_P^t = 2\sum_{b}^{N_p}\sum_{c}^{N}\sum_{j}^{unoccupied}\sum_{i}^{occupied} A_{ij}c_i^{Pb}c_j^c S_{Pb,c} \quad (2\text{-}3)$$

where, for an atom *P, b* is the atomic-orbital (AO) index for that atom; N_P is its number of AOs; *c* is the AO index for an entire molecular orbital (MO); *N* is the total number of AOs making up an MO; and A_{ij} is the CI coefficient for the determinant where an electron is excited from occupied MO *i* to unoccupied MO *j*, with the total sum of A_{ij} normalized to a value of 1. Furthermore, c_i^{Pb} is the *b*th AO coefficient centered on atom *P* of the *i*th occupied MO; c_j^c is the *c*th AO coefficient of the *j*th unoccupied MO; $S_{Pb,c}$ is the overlap between these two AOs; and *i* and *j* span the total number of occupied and unoccupied MOs, respectively. The atomic orbital basis set used was Dunning's cc-pVDZ basis.[40] Although it is well-known that atomic charges derived from MPA of the ground-state density can predict inaccurate ground-state dipole moments and are also very sensitive to the AO basis set chosen, q^t derived from MPA do not, in general, have these problems. Indeed, the stability of the method with respect to basis set has been mentioned previously,[36] and in a forthcoming publication, we will demonstrate this comprehensively for a variety of chromophore types in a benchmark theoretical study. In addition, the transition dipole magnitude for PDI is predicted well from MPA-derived q^t values using the TDDFT transition density, at 8.4 D, compared to experiment (8.5 D).

The coupling, J_{12}, between chromophores 1 and 2 appearing in eq 2-2 can then be efficiently calculated from a simple Coulombic charge-charge interaction between the transition charges on one chromophore with those of the other, such that

$$J_{12} = \sum_i \sum_j \frac{q_i^t q_j^t}{\left| R_i^{(1)} - R_j^{(2)} \right|}$$

(2-4)

where *i* and *j* are the atom indices corresponding to chromophores 1 and 2, respectively; $R_i^{(m)}$ is the position of the ith atom on chromophore m. The bichromophore PDI_2 in Figure 9 was optimized at the PM3 level, and then the binaphthalene portion was removed, and reasonable methyl groups were attached to the nitrogens previously attached to the binaphthalene ring carbons, creating two separate N,N-dimethyl PDI chromophores with the same PDI atomic positions as in PDI_2. In this manner, we evaluated the coupling (in cm^{-1}) between the two PDI portions to be

$$J_{12} \equiv \langle 1|H|2\rangle = 371 \text{ cm}^{-1}$$

(2-5)

The positive sign of the coupling assumes that the relative phases of the localized wave functions are defined through the relation, $|2\rangle = \hat{C}_2|1\rangle$, where $\hat{C}_2$ represents a 2-fold rotation about the symmetric C_2 axis (see Figure 2-1).

The Hamiltonian in eq 2-2 is represented in a one- and two-particle basis set.[41, 42] Single-particle excitations, $|n, \tilde{v}\rangle$, consist of a vibronically excited chromophore at site *n* with $\tilde{v}$ excited-state quanta in the (shifted) excited-state nuclear potential. The other molecule is electronically and vibrationally unexcited. A vibronic/vibrational pair excitation, denoted $|n, \tilde{v}; n'v'\rangle$, is a two-particle state because it involves excitations on both molecules. In addition to a vibronic excitation at *n*, this state includes a vibrational excitation at $n'(\neq n)$ with $v'(\geq 1)$ quanta in the ground-state potential. For a dimer, there are no three- or higher particle states. In all calculations that follow, we impose an

upper limit of six on the total number of vibrational quanta. Because of the inherent C_2 symmetry of the dimer of Figure 2-1, all eigenfunctions are either symmetric (+) or antisymmetric (-) under C_2 rotation. Hence, the αth symmetric or antisymmetric eigenstate of H can be written in the form

$$|\Psi_{\pm}^{\alpha}\rangle = \sum_{\tilde{\nu}} c_{\pm,\tilde{\nu}}^{(\alpha)} \left(|1,\tilde{\nu}\rangle \pm |2,\tilde{\nu}\rangle\right) + \sum_{\tilde{\nu}}\sum_{\nu'} c_{\pm,\tilde{\nu},\nu'}^{(\alpha)} \left(|1,\tilde{\nu};2,\nu'\rangle \pm |2,\tilde{\nu};1,\nu'\rangle\right)$$

2-6

where α = 1, 2, ..., in order of increasing state energy. The transition energies of the states $|\Psi_{+}^{\alpha}\rangle$ and $|\Psi_{-}^{\alpha}\rangle$ are denoted as $\omega_{+,\alpha}$ and $\omega_{-,\alpha}$, respectively (note that we take $\hbar$=1 here.)

When vibronic coupling is absent in the bichromophoric complex, there are just two excited states: an antisymmetric exciton shifted by $-J_{12}$ due to intermolecular coupling and a higher-energy symmetric exciton shifted by $+J_{12}$. In the absorption spectrum, the two peaks give rise to the so-called Davydov components. The magnitude of the energetic separation between the components is referred to as the Davydov splitting (DS). In the free exciton limit (no vibronic coupling), the DS is simply $2J_{12}$ (recall $J_{12} > 0$). When vibronic coupling is activated (and $J_{12} \ll \lambda^2\omega_0$), each n-0 vibronic peak in the monomer spectrum is split into a lower and upper Davydov component with the splitting approximately equal to

$$DS_{n-0} \approx 2J_{12}e^{-\lambda^2}\lambda^{2n}/n!$$

(2-7)

as demonstrated in the energy level diagram in Figure 2-3. The symmetric (upper Davydov) states are polarized in the direction of $\boldsymbol{\mu}_1 + \boldsymbol{\mu}_2$ (defined as the x axis), whereas the antisymmetric (lower Davydov) states are polarized in the direction of $\boldsymbol{\mu}_1 - \boldsymbol{\mu}_2$ (defined as the y axis). Here, $\boldsymbol{\mu}_1$ and $\boldsymbol{\mu}_2$ are the longaxis- polarized $S_0 \rightarrow S_1$ transition

dipole moments of molecules 1 and 2, respectively (see Figure 2-1). Because the molecular dipoles are of equal magnitude, the two polarization directions are orthogonal. In cases where the two PDI molecules are perfectly cofacially overlapping, $\boldsymbol{\mu}_1$ and $\boldsymbol{\mu}_2$ point along a common direction, and the lower Davydov component is forbidden.

Figure 2-3

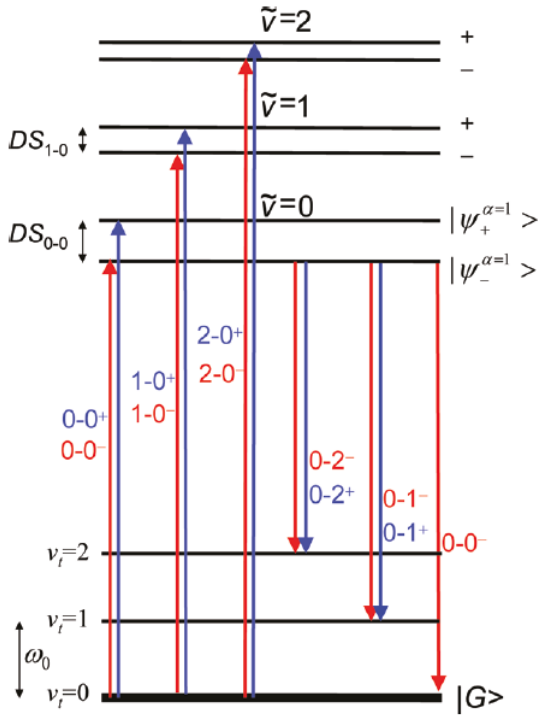

Figure 2-3. Energy level diagram for PDI2 in the limit of weak excitonic coupling and low temperature showing absorption transitions (left) and emission transitions (right). Blue (red) transitions are x- (y-) polarized. Energy level ordering is consistent with $J_{12} > 0$. Only ground and excited electronic levels with two or fewer vibrational quanta are shown. Note that the optical gap is not to scale.

2-4 Absorption

The Davydov components are clearly identified by decomposing the unpolarized (dimensionless) absorption spectrum A(ω) into its components $A_+(\omega)$ and $A_-(\omega)$ along the x and y axes, respectively, as defined in Figure 2-1

$$A(\omega) = A_{+}(\omega) + A_{-}(\omega)$$

(2-8)

with

$$A_{\pm}(\omega) = \frac{1}{\mu_1^2}\sum_{\alpha}\left|\left\langle G\left|\widehat{M}_{\pm}\right|\Psi_{\pm}^{(\alpha)}\right\rangle\right|^2 W_{LS}(\omega - \omega_{\pm,\alpha})$$

(2-9)

Here, $|G\rangle$ is the vibrationless ground state consisting of the product of the pure electronic ground state, $|g\rangle = |g_1 g_2\rangle$, and the vacuum vibrational state (relative to S_0) and W_{LS} is a symmetric line shape function. M_+ and M_- are the symmetry-adapted components of the transition dipole moment (tdm) operator, $\widehat{M} \equiv \widehat{M}_+ + \widehat{M}_-$, with

$$\widehat{M}_{\pm} = \frac{1}{2}(\mu_1 \pm \mu_2)(|g\rangle\langle 1| \pm |g\rangle\langle 2| + h.c.)$$

(2-10)

In eq 2-10, h.c. indicates the Hermitian conjugate.

2-5 Absorption: Comparison to Experiment

Figure 2-4 shows the measured absorption spectrum for PDI_2 from ref. 8 alongside the calculated unpolarized absorption spectrum A(ω) obtained using the computed coupling (J_{12} = 371 cm^{-1}) and the HR factor (λ^2 = 0.57) determined from the monomer solution spectrum in Figure 2-2. Because $\hbar$ = 1, one can view ω as the photon energy and express it in wavenumbers.

Figure 2-4

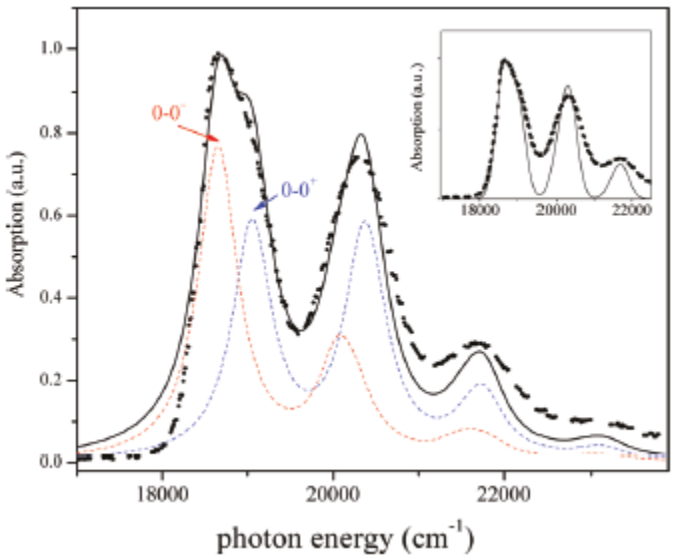

Figure 2-4. Calculated unpolarized absorption spectrum (black) and components polarized along the x axis (blue) and y axis (red). The measured spectrum from ref 8(citation) is also shown (black dots). Parameters used in the calculation: J_{12} = 371 cm_1, λ2 = 0.57, ω_0 =1400 cm^{-1} and $\omega_{0\text{-}0}$ + D = 18900 cm^{-1} (D = -100 cm^{-1}). The line shape used is Lorentzian with fwhm =0.4ω_0. In the inset, the line shape is Gaussian with full width (1/e) = 0.4ω_0.

In Figure 2-4, we used a peak-normalized Lorentzian line shape function with a full width at half-maximum of 0.4ω_0. In the inset, a Gaussian line shape with a full width (1/*e,*) equal to 0.4ω_0 was used. Overall, the calculated spectrum in Figure 2-4 does an excellent job in reproducing the relative vibronic peak intensities, as well as the blue shoulder in the main absorption peak. It is clear from the inset that a Gaussian function does a superior job in reproducing the spectral line shape of the main absorption peak, especially the blue shoulder; the line widths of the subsequent peaks are, however, too narrow compared with experiment and are better described using the single Lorentzian. Most likely, the higher-energy sidebands show broadening as a result of the involvement

of several closely spaced vibrational modes in the vicinity of the vinyl stretch. Our inclusion of a single vibrational mode is, in fact, an approximation and should be viewed as an effective mode.[43] In a more sophisticated multimode calculation, the first vibrational sideband (second main peak) would be composed of several closely spaced Gaussians, one for each mode. Nevertheless, our single-mode theory with an effective HR factor of 0.57 manages to reproduce the relative vibronic oscillator strengths, as determined by the vibronic peak areas.

Figure 2-4 also shows the calculated polarized absorption spectra corresponding to light polarized along the x and y axes defined in Figure 2-1 due to the symmetric and antisymmetric excitons, respectively. Vibronic progressions corresponding to the symmetric (antisymmetric) excitons are labeled as $0\text{-}0^{+}$, $1\text{-}0^{+}$, $2\text{-}0^{+}$, ... ($0\text{-}0^{-}$, $1\text{-}0^{-}$, $2\text{-}0^{-}$, ...), in order of increasing energy, see Figure 2-3. The DS corresponding to the first main absorption peak was determined to be

$$DS_{0-0} = \hbar\omega_{+,1} - \hbar\omega_{-,1} = 403\ cm^{-1} \qquad 2\text{-}11$$

which agrees well with 420 cm^{-1} predicted from eq 2-7 using an HR factor of 0.57. The DS values for subsequent peaks are significantly smaller and cannot be discerned from the unpolarized spectrum.

The two polarized line shapes in Figure 2-4 are quite different; in the x-polarized absorption spectrum due to the symmetric exciton, the ratio of the origin to the first sideband oscillator strengths, $I_A^{(0-0)+}/I_A^{(1-0)+}$, is approximately unity, much smaller than the corresponding value of 1.75 measured in the monomer spectrum (see Figure 2-2). By contrast, the ratio corresponding to the y-polarized spectrum (antisymmetric exciton) is

much larger than the monomer value, $I_A^{(0-0)-}/I_A^{(1-0)-} \approx 2.48$. In Ref. 7, it was shown that a readily identifiable spectral signature of ideal J- (H-) aggregates is an increase (decrease) in the ratio of oscillator strengths $I_A^{(0-0)}/I_A^{(1-0)}$ upon aggregation. In this regard, the higher energy (x-) polarized component of the dimer spectrum strongly resembles that of an ideal H-aggregate, while the lower energy (y-) polarized component resembles that of an ideal J-aggregate.

2-6 Analysis of the Absorption Spectrum

To more firmly establish the relationship between the absorption spectra of the polarized components of the chiral dimer and those of ideal J- and H-aggregates, we appeal to first-order perturbation theory. A systematic analysis of the effect of excitonic interactions on the vibronic line strengths in various aggregates was previously considered in Refs. 4, 6, 7, 45, and 46. A perturbative expression for the oscillator strength ratio of the first two vibronic peaks was derived for H-aggregates with nearest-neighbor coupling only.[45, 46] A more general expression, valid for extended interactions and for any aggregate type (J or H) was recently presented in Ref. 7. For an ideal J- or H-aggregate containing an arbitrary number of molecules and extended couplings, the 0-0/0-1 line strength ratio is determined from

$$\frac{I_{\mathrm{A}}^{0-0}}{I_{\mathrm{A}}^{1-0}} = \frac{1}{\lambda^2}\left[\frac{1 - G(0;\lambda^2)\mathrm{e}^{-\lambda^2\tilde{J}_{k=0}/\omega_0}}{1 - G(1;\lambda^2)\mathrm{e}^{-\lambda^2\tilde{J}_{k=0}/\omega_0}}\right]^2 \quad |\tilde{J}_{k=0}| \ll \omega_0 \tag{2-12}$$

where periodic boundary conditions are assumed. In eq 2-12, the k = 0 interaction sum is given by,

$$\tilde{J}_{k=0} = \sum_{s} J_{n,n+s}$$

(2-13)

where s = ±1, ±2, ..., runs over all neighbors, and the vibrational function $G(\nu_t;\lambda^2)$ is defined as

$$G(\nu_t;\lambda^2) \equiv \sum_{\substack{u=0,1,\ldots \\ (u\neq\nu_t)}} \frac{\lambda^{2u}}{u!(u-\nu_t)} \qquad \nu_t = 0,1,2,\ldots$$

(2-14)

Equation 2-14 reduces to our previously derived expression for polymer H-aggregates[6] when the HR factor is set to unity and only nearest-neighbor couplings are retained. Under the latter condition, $\tilde{J}_{k=0}$ in eq 2-11 can be replaced by W/2, where $W \equiv |\tilde{J}_{k=0} - \tilde{J}_{k=\pi}|$ is the exciton bandwidth. (For nearest-neighbor coupling, $\tilde{J}_{k=0} = 2J_{12}$, and $\tilde{J}_{k=\pi} = -2J_{12}$. Hence, $W = 4J_{12}$, and $\tilde{J}_{k=0} = W/2$.)

Equation 2-12 applies directly to the cofacial dimer ($\phi = 0°$) when $\tilde{J}_{k=0} = +J_{12}$. For the chiral dimer ($\varphi \neq 0$) with C_2 symmetry, an equation identical to eq 2-14 holds for the symmetric (antisymmetric) component of the spectrum if $\tilde{J}_{k=0}$ is replaced by $+J_{12}$ ($-J_{12}$). Hence, in the general case of arbitrary ϕ, we obtain

$$\frac{I_A^{(0-0)^{\pm}}}{I_A^{(1-0)^{\pm}}} = \frac{1}{\lambda^2}\left[\frac{1-G(0;\lambda^2)e^{-\lambda^2}J_{\pm}/\omega_0}{1-G(1;\lambda^2)e^{-\lambda^2}J_{\pm}/\omega_0}\right]^2 \qquad |J_{\pm}| \ll \omega_0$$

(2-15)

where $J\pm \equiv J_{12}$. After inserting the values

$$G(\tilde{\nu}_t = 0; \lambda^2 = 0.57)e^{-0.57} = 0.375$$

and

$$G(\tilde{\nu}_t = 1; \lambda^2 = 0.57)e^{-0.57} = -0.464$$

into eq 17, we obtain

$$\frac{I_A^{(0-0)^{\pm}}}{I_A^{(1-0)^{\pm}}} = \frac{1}{0.57}\left(\frac{1 - 0.375J_{\pm}/\omega_0}{1 + 0.464J_{\pm}/\omega_0}\right)^2 \qquad |J_{\pm}| \ll \omega_0$$

2-16

which gives

$$\frac{I_A^{(0-0)^{+}}}{I_A^{(1-0)^{+}}} = 1.13 \quad \text{and} \quad \frac{I_A^{(0-0)^{-}}}{I_A^{(1-0)^{-}}} = 2.76$$

2-17

for J_{12} = 371 cm^{-1}. These values compare favorably with the numerically calculated values of 1.01 and 2.48 for the x- and y-polarized spectra, respectively.

The nature of the polarized spectra can be further appreciated by varying the interchromophore angle ϕ from 0° to 180° about an axis containing the carbon atoms of each PDI chromophore, which are directly bonded to the naphthalene bridge. (In this calculation, we treat separate PDI molecules; that is, we replace the bridge with N-methyls, as described in the Model section.) In this manner, the aggregate evolves from an ideal H-aggregate (ϕ = 0°, side-by-side) to an ideal J-aggregate (ϕ = 180°, head-totail). The corresponding changes in the absorption spectra are shown in Figure 2-5. The insets report the calculated couplings, J_{12}, which steadily decrease as ϕ increases but remain

positive throughout. We note that a similar analysis of the ϕ-dependent (but unpolarized) absorption spectrum was conducted by Seibt et al.,[26] with spectra qualitatively similar to those in Figure 2-6.

In the ideal H-aggregate limit (ϕ = 0°) shown in Figure 2-5a, only the x-polarized spectrum from the symmetric, high-energy excitons are optically allowed. The spectrum shows a substantially weakened $0\text{-}0^{+}$ peak relative to the second vibronic peak ($1\text{-}0^{+}$) due to the strong excitonic coupling, J_{12} = 1169 cm^{-1}, resulting from cofacial overlap. The spectrum of Figure 13a, with its depressed 0-0/1-0 peak ratio compared to the monomeric PDI spectrum (see Figure 2-2), is very typical of many PDI dimers where the molecules significantly overlap.[10,11,13,17,19] With increasing ϕ value, the ratio $I_A^{(0-0)+}/I_A^{(1-0)+}$ increases in response to the decreasing excitonic coupling, characteristic of H-aggregates (see eq 2-16).

Figure 2-5

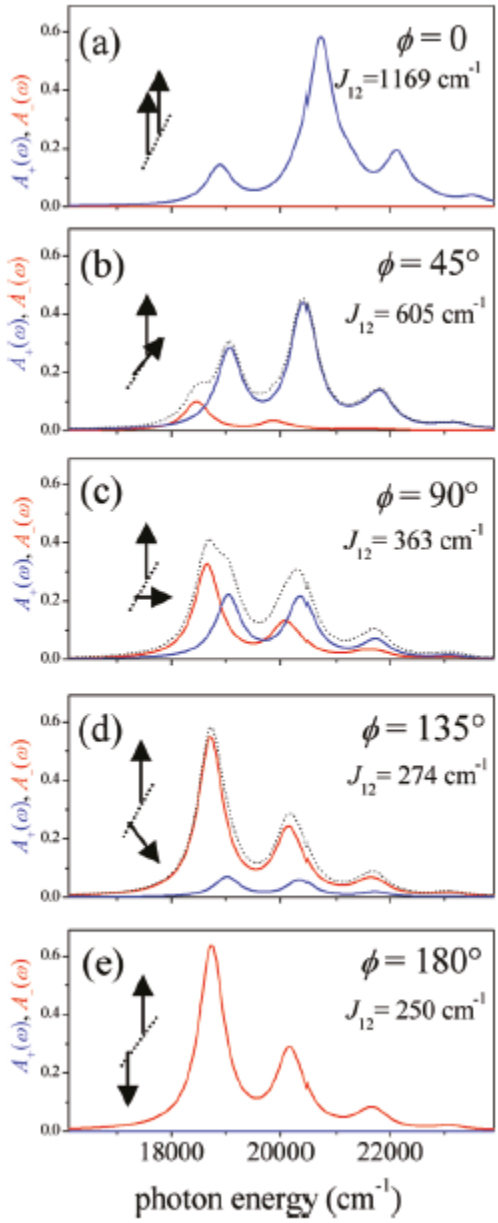

Figure 2-5. Calculated absorption spectra for PDI2 complexes with increasing interchromophore angle, ϕ. Black arrows denote the two molecular transition dipolemoments, μ_1 and μ_2. The blue (red) spectrum is the x- (y-) polarized component. (See Figure 1; recall that the x axis is the C_2 axis). The dotted curve is the unpolarized sum. The remaining parameters are the same as in Figure 2-4. Lorentzian line shapes were used with fwhm = $0.4\omega_0$.

As the angle ϕ increases in Figure 2-5, one also observes the growth of the y-polarized spectrum from the antisymmetric exciton showing clear J-aggregate signatures: The spectrum red shifts with increased excitonic coupling and, in marked contrast to the H-like x-polarized spectrum, is dominated by the first vibronic peak (0-0$^-$). As ϕ increases, the y-polarized spectrum continues to grow relative to the x-polarized spectrum until, when ϕ = 180°, the aggregate becomes an ideal J-aggregate, and only the y-polarized spectrum is observed. Moreover, as the exciton coupling decreases in going from Figure 2-5b to Figure 2-5e, the ratio $I_A^{(0-0)-}/I_A^{(1-0)-}$ also decreases (from approximately 2.8 to 2.2), as expected for ideal J-aggregates (see eq 2-16).

2-7. Photoluminescence Spectrum: Theory vs. Experiment

In this section, we consider the PL spectrum of the bichromophoric PDI complexes. As for the absorption spectrum, the emission spectrum can be divided into components $S_+(\omega)$ and $S_-(\omega)$ polarized along x and y, respectively

$$S(\omega) = S_+(\omega) + S_-(\omega) \tag{2-18}$$

with

$$S_\pm(\omega) = \sum_{v_t = 0, 1, 2, \ldots} I_{\mathrm{PL}}^{(0 - v_t)^\pm} W_{LS}(\omega - \omega_{-, \alpha=1} + v_t\omega_0) \tag{2-19}$$

Equation 2-18 assumes the low-temperature limit where emission takes place from just the lowest exciton, namely, the antisymmetric exciton with α = 1. Emission terminates on the ground electronic state with any number of purely vibrational excitations, forming a

vibronic progression, as demonstrated in Figure 2-3. To focus entirely on the impact of aggregation on the oscillator strengths, we have also neglected in eq 2-19 the cubic frequency dependence found in the Einstein spontaneous emission expression, as well as any influence of a frequency-dependent index of refraction. Hence, we refer to the PL spectrum in eq 2-19 as a reduced PL spectrum. Equation 2-19 contains the dimensionless emission line strength for the 0-ν_t transition, given by

$$I_{\mathrm{PL}}^{(0-\nu_t)^{\pm}} \equiv \frac{1}{{\mu_1}^2} \sum_{\nu_1,\nu_2=0,1,2,\ldots}{}' \left| \left\langle g_1\nu_1, g_2\nu_2 \left| \hat{\mathbf{M}}_{\pm} \right| \psi_{-}^{(\alpha=1)} \right\rangle \right|^2 \tag{2-20}$$

where the prime on the summation indicates that the total number of vibrational quanta in the terminal state, $|g_1\nu_1 = 0, g_2\nu_2 = 0\rangle$, satisfies $\nu_t = \nu_1 + \nu_2$. Simple group theory shows that the 0-0 transition is always y-polarized, because the terminal state, $|g_1\nu_1 = 0, g_2\nu_2 = 0\rangle$, is symmetric under a C_2 rotation. For sideband transitions, however, a mixture of polarizations is possible because the terminal states with one or more vibrational quanta can be symmetric or antisymmetric. Consider, for example, the 0-1 transition. It can terminate on either of two states

$$\frac{1}{\sqrt{2}}\left(|g_1\nu_1 = 0, g_2\nu_2 = 1\rangle \pm |g_1\nu_1 = 1, g_2\nu_2 = 0\rangle\right) \tag{2-21}$$

Group theory then shows that the 0-1 sideband contains a component polarized along x when the terminal state in eq 2-20 is antisymmetric and a component polarized along y when the terminal state in eq 2-20 is symmetric.

Equations 2-19 and 2-20 are written in a local basis set with respect to the terminal states. This is possible because we neglect any interactions between ground-state vibrations: they are Einstein phonons with no dispersion. Hence, the 0-ν_t line strength is independent of the basis set chosen for the terminal states.

Figure 2-6 shows the calculated (reduced) PL spectra as a function of the angle ϕ for the PDI_2 complexes of Figure 2-5. Several properties are immediately apparent: For an ideal H-aggregate ($\phi = 0°$), the two molecular transition dipoles are parallel; hence, there can be no y-polarized component because $\mu_1 - \mu_2 = 0$. Equation 2-20 further shows that the surviving x-polarized spectrum cannot support a 0-0^+ peak because of the symmetry mismatch between the antisymmetric emitting state and the symmetric dipole moment μ_+ (the terminal state, $|G\rangle$, is symmetric in 0-0 emission); see Figure 2-3. In addition, the sideband progression is very weak because of the strong coupling. All of these properties are consistent with ideal H-aggregates.[7]

As ϕ increases, $\mu_1 - \mu_2$ is no longer zero, allowing the antisymmetric component polarized along y to develop. This y-polarized spectrum is dominated by strong 0-0^- emission, which is allowed by symmetry, just as for an ideal J-aggregate. When $\phi = 180°$, an ideal J-aggregate results. Here, $\mu_1 + \mu_2 = 0$, and there can only be y-polarized emission polarized along $\mu_1 - \mu_2$. In this case, the two transition dipole moments in the antisymmetric emitting state, μ_1 and $-\mu_2$, are equal. (In an ideal J-aggregate, this is often described as the k = 0 state, where k is the wave vector.)

Hence, in the general case, emission from a chiral dimer complex is both x- and y-polarized. The symmetric (x-polarized) component has the spectral profile of an ideal H-aggregate, and the antisymmetric (y-polarized) component has the spectral profile of

an ideal J-aggregate. Note that, if, for some physical reason, the sign of J_{12} becomes negative, then the emitting state would be symmetric, and $\phi = 0°$ (180°) would correspond to an ideal J- (H-) aggregate.

One of the most remarkable features of the y-polarized (J-like) spectrum in Figure 2-6 is the invariance of the ratio $I_{PL}^{(0-0)-}/I_{PL}^{(1-0)-}$ to the angle ϕ and, therefore, to the coupling strength, J_{12}. In Figure 2-6a-e, the ratio is approximately 3.51, which is equal to $2/\lambda^2$ for $\lambda^2 = 0.57$. We have verified that

$$I_{\mathrm{PL}}^{(0-0)^-}/I_{\mathrm{PL}}^{(0-1)^-} = 2/\lambda^2 \tag{2-22}$$

holds for any λ^2, independent of ϕ and J_{12}. In Ref. 34, we showed that, for aggregates containing two molecules per unit cell (with periodic boundary conditions), the PL ratio is given by

$$I_{\mathrm{PL}}^{(0-0)_\rho}/I_{\mathrm{PL}}^{(0-1)_\rho} = N/\lambda^2 \tag{2-23}$$

where N is the total number of chromophores (which must be even for an integral number of unit cells) and ρ indicates the polarization direction of the lower Davydov component. The validity of eq 23 further requires no disorder and T = 0 K, so that only the lowest exciton (lower Davydov component) emits. Equation 2-22 is therefore a special case of eq 2-23 when N = 2.

Figure 2-6

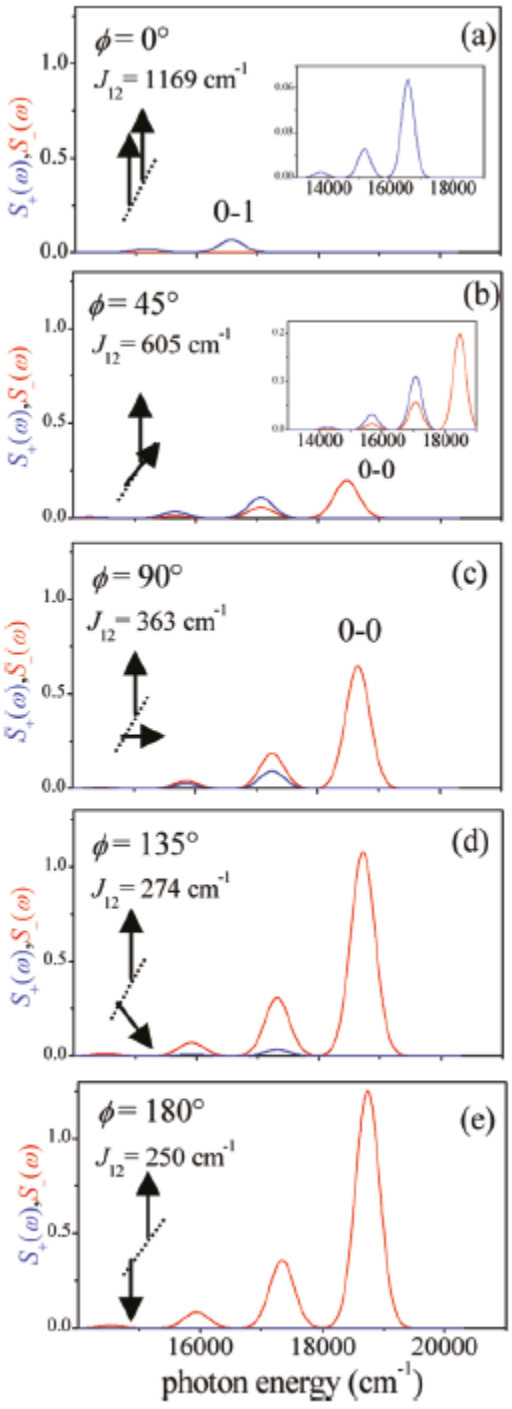

Figure 2-6. Calculated PL spectra for PDI2 complexes with increasing interchromophore angle, ϕ. Black arrows denote the two molecular transition dipole moments, μ_1 and μ_2. The blue (red) spectrum is the x- (y-) polarized component. Insets in (a) and (b) show the magnified spectra. Note the total lack of a 0-0

component in panel a. Gaussian line shapes were used with full width (1/e) = $0.4\omega_0$. The remaining parameters are the same as in Figure 2-4.

In Figure 2-7, we compare our calculated reduced PL spectrum with that derived from the experimental PL spectrum from Ref. 8. Because the latter was originally reported as a function of wavelength, we first converted to photon energy, which required multiplying the spectrum by the square of the wavelength, λ^2 (because $d\omega$ is proportional to $d\lambda/\lambda^2$) and then divided by the cube of the energy (from the Einstein spontaneous emission expression) to give the reduced PL spectrum. Also shown in Figure 2-7 are the calculated x- and y-polarized components of the PL spectrum.

Figure 2-7

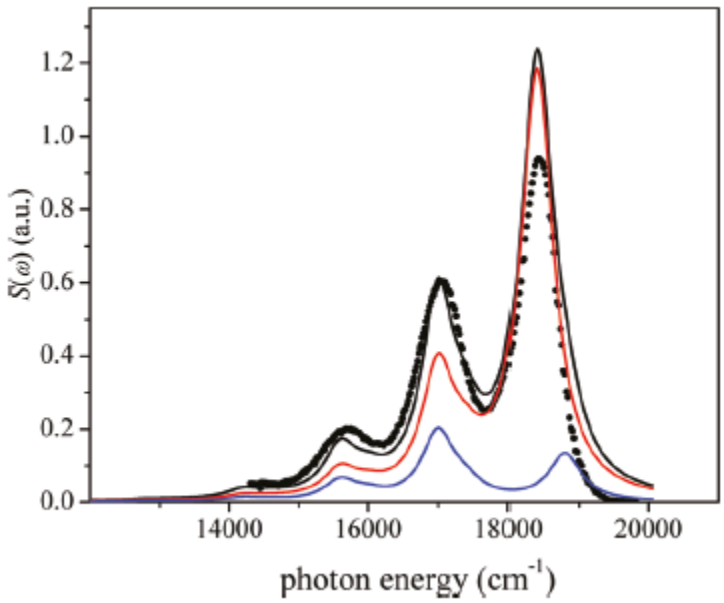

Figure 2-7. Calculated (reduced) unpolarized PL spectrum (black) and its resolution into x-polarized (blue) and y-polarized (red) components at T = 300 K using Lorentzian line shapes. Also shown is the measured spectrum from Ref. 8 (see text for details). All parameters used in the calculated spectra are identical to those used in Figure 12, except ω_{0-0}^{+} D = 18650 cm^{-1}. The calculated unpolarized spectrum and the measured spectrum were normalized to the 0-1 peak.

The calculated spectra in Figure 2-7 also contain a Boltzmann average over the emitting states. This is required because the experimental spectra were obtained at 300 K and, at this temperature, there is some thermal excitation of the symmetric state, $|\Psi_+^{\alpha=1}\rangle$ (see Figure 2-3), that can subsequently emit. The most important thermal effect is the nonzero 0-0 emission observed in the symmetric (x-polarized) spectrum sourced by $|\Psi_+^{\alpha=1}\rangle$. This is in accord with the basic property that 0-0 emission increases with temperature in H-aggregates. In contrast, the 0-0 component of the y-polarized spectrum is reduced compared to the spectrum at T = 0 K, fully consistent with what is expected for ideal J-aggregates.[34, 47]

Figure 2-7 shows that the theory and experiment are generally in good agreement, with the largest disparity involving a significantly larger calculated 0-0 peak intensity. We expect that the measurements might be susceptible to reabsorption because the optical density of the samples is near unity. There might also be some disorder in the sample, which would make the frequencies of the two chromophores slightly different. Such inhomogeneous broadening will act, similarly to increasing temperature, to reduce the predominant 0-0$^-$ peak.[7, 34]

2-8. Discussion and Conclusions

Absorption and emission in chiral dimer complexes in which the two chromophores are related by a C_2 symmetry operation can be understood in terms of ideal H- and J-aggregate behavior. When exciton coupling is weak compared to the nuclear relaxation energy, oscillator strength is generally divided between the top and bottom of each vibronic exciton band, giving rise to the two Davydov components as depicted in

Figure 2-3; in the limiting extremes of ideal H- and J aggregates, where the chromophore transition dipoles are aligned ($\phi = 0°$ and 180°), oscillator strength is concentrated at the top and bottom of each band, respectively, and only a single Davydov component is observed in each vibronic band. Nevertheless, we found that, in the general case for arbitrary ϕ, the absorption component polarized along the direction of the lower Davydov component (y) displays vibronic structure identical to that of an ideal J-aggregate: The oscillator strength ratio, $I_A^{(0-0)-}/I_A^{(1-0)-}$, increases as the exciton bandwidth increases (see eq 2-16). By contrast, the absorption component polarized along the direction of the upper Davydov component (x) is characteristic of an ideal H-aggregate: The oscillator strength ratio, $I_A^{(0-0)+}/I_A^{(1-0)+}$, decreases with increasing exciton bandwidth. In addition, the spectral centroid of the upper (lower) Davydov component blue (red) shifts with increasing bandwidth as expected for H- (J-) aggregates. The PL for a dimer complex can be understood in a similar way. Emission originating from the lowest-energy exciton is generally polarized along x and y. Nevertheless, the component polarized in the same direction as the upper (lower) Davydov component strongly resembles ideal H- (J-) aggregate emission with respect to the spectral signatures outlined in Ref. 7. In the H-like component the $0\text{-}0^+$ peak is disallowed by symmetry and the rest of the progression is depressed with increasing exciton bandwidth. Rising temperature serves to increase the ratio $I_{PL}^{(0-0)+}/I_{PL}^{(1-0)+}$ through thermal activation of the upper Davydov component. (Increasing disorder has the same effect.) By contrast, in the J-like component, the ratio $I_{PL}^{(0-0)-}/I_{PL}^{(1-0)-}$ is exactly equal to $2/\lambda^2$ (when T = 0 K and disorder is absent) independent of the exciton bandwidth. The ratio decreases with increasing temperature (or the addition of disorder) in exact opposition to the H-like spectral component.[34]

For the PDI_2 complexes of Ref. 8, our single-mode Holstein Hamiltonian, with a through-space excitonic coupling of J_{12} = 371 cm^{-1} evaluated quantum mechanically, provides a quantitative account of the absorption, PL, and CD spectral line shapes. The calculated DS of the 0-0 transition is in excellent agreement with the measured DS of approximately 400 cm^{-1}. The success is, in part, due to the large angle of ϕ=86° between the PDI long axes, which prevents significant interchromophore charge transfer, an effect that was not taken into account in the present model. For sandwich-type PDI complexes ($\phi \approx 0$), emission is often dominated by excimers.[13, 14] Seibt et al.[27] showed that, in self-assembled PDI sandwich dimers, exciton self-trapping along an intermolecular torsional coordinate is a primary cause of excimer emission.

The dimer complex can be viewed as the basic building block of the herringbone lattice, a common packing motif for many rod-shaped conjugated molecules. In a (two-dimensional) herringbone lattice, the two molecules in a unit cell are usually related through a glide translation or screw rotation, giving rise to the two Davydov components with exciton shift energies $\tilde{J}_{11} \pm \tilde{J}_{12}$.[32, 33] Here, $\tilde{J}_{11}$ represents the (k = 0) dipole sum involving interactions between equivalent molecules, whereas $\tilde{J}_{12}$. represents the (k = 0) dipole sum involving interactions between inequivalent molecules. Hence, the vibronic structure of the polarized absorption and emission spectra of dimer complexes and herringbone aggregates are very similar, provided that the inequivalent sum is dominant ($|\tilde{J}_{12}| > |\tilde{J}_{11}|$). In such aggregates, the two excitonic shifts have opposite signs: The lower Davydov component shifted by $\tilde{J}_{11}$ - $|\tilde{J}_{12}|$ will always resemble ideal J-aggregate absorption while the upper component shifted by $\tilde{J}_{11}$ + $|\tilde{J}_{12}|$ will always resemble ideal

H-aggregate absorption. Here, the absorption ratios are simply obtained by inserting the two k = 0 exciton energies ($\tilde{J}_{11} \pm \tilde{J}_{12}$) into eq 2-13.

Oligothiophenes, OTn, with an even number of thiophene rings (n) crystallize in herringbone layers,[48] with dominant inequivalent interactions leading to a very large Davydov splitting of the order of 1 eV.[49, 50] For even n, the molecular symmetry is C_{2h}, and the transition dipole moment corresponding to the lowest optical transition is not aligned with the long (inertial) axis, leading to a slight misalignment of the two transition dipoles in the monoclinic unit cell.[51-53] The *ac*-polarized absorption spectrum is dominated by the blue-shifted H-band, with a much weaker ac-polarized peak near the origin (A_0).[54] By contrast, the b-polarized spectrum is much weaker (because of the nearly parallel transition dipoles) but dominated by the origin vibronic peak as expected for an ideal J-aggregate. (There is, however, significant complexity at higher energies in the b-polarized spectrum introduced by charge-transfer transitions.[55] Emission contains both components, a b-polarized origin (J-like) followed by ac polarized sidebands (H-like).[51] Overall, the behavior qualitatively resembles a chiral dimer with a small value of ϕ; see Figures 2-5 and 2-6.

A second example is crystalline anthracene. In molecular anthracene, the transition dipole moment (tdm) corresponding to the lowest optical transition is along the short molecular axis. In the crystal phase, the two tdm's in the unit cell form an angle of approximately 60°. Although the exciton shifts from throughspace coupling are dominated by a large and negative equivalent lattice sum, the introduction of charge transfer between the two molecules in a unit cell acts as an effective "superexchange" contribution to the inequivalent lattice sum, allowing the latter to dominate.[56] Hence, we

expect J- and H-like polarized absorption similar to Figure 2-5b,c, which is indeed the case:[57] The lower energy component is polarized along the b axis and is dominated by a 0-0 peak that is about twice as large as the 1-0 peak. By contrast, in the higher-energy *ac* polarized component, the 0-0 and 1-0 peaks are of roughly equal intensity. Emission is almost entirely b-polarized and, at early times (following impulsive excitation), strongly resembles a J aggregate with a 0-0 peak several times larger than the 0-1 peak.[58] Very similar behavior is also observed in tetracene.[59]

Finally, we emphasize the importance of eq 2-23, which relates the 0-0/0-1 PL oscillator strength ratio to the number of chromophores in a disorder-free linear or herringbone aggregate at T = 0 K. In Ref. 34, we showed that, when disorder is present and/or the temperature is nonzero, eq 2-23 becomes

$$I_{\mathrm{PL}}^{(0-0)_\rho} / I_{\mathrm{PL}}^{(0-1)_\rho} \approx N_{\mathrm{coh}}/\lambda^2 \tag{2-24}$$

where N_{coh} is the number of coherently connected molecules in the emitting exciton, which, in an aggregate containing N chromophores, can range between N and unity as disorder (or temperature) is increased. Hence, eq 2-24 allows a straightforward determination of N_{coh} directly from the PL spectrum. In future works, we will investigate the utility of eq 24 in evaluating the coherence number in PDI J-aggregates that strongly fluoresce with a dominant 0-0 PL peak.[9-10]

In the next chapter this model is applied to a larger variety of covalently bound PDI complexes. These small PDI systems are divided into two groups, a linear series and a symmetric series, based on the geometry and orientations of the PDI molecules. We show that there are clear trends exhibited by both series, for example the linear series

shows the behavior of a canonical J-aggregate. In studying this large variety of structures, we show that the model presented herein is versatile while still remaining accurate, and we show that the two particle approximation is still a valid approach even in a system with more than two chromophores.

REFERENCES

1. Hochstrasser, R. M.; Kasha, M. Photochem. Photobiol. 1964, **3**, p. 317–331.

2. Kasha, M. Radiat. Res. 1963, **20**, p. 55–70.

3. McRae, E. G.; Kasha, M. J. Chem. Phys. 1958, **28**, p. 721–722.

4. Spano, F. C. J. Am. Chem. Soc. 2009, **131**, p. 4267–4278.

5. Spano, F. C.; Clark, J.; Silva, C.; Friend, R. H. J. Chem. Phys. 2009, **130**, p. 074904.

6. Clark, J.; Silva, C.; Friend, R. H.; Spano, F. C. Phys. Rev. Lett. 2007, **98**, p. 206406.

7. Spano, F. C. Acc. Chem. Res. 2010, **43**, p. 429–439.

8. Langhals, H.; Hofer, A.; Bernhard, S.; Siegel, J. S.; Mayer, P. J. Org. Chem. 2011, **76**, p. 990–992.

9. Kaiser, T. E.; Stepanenko, V.; Wurthner, F. J. Am. Chem. Soc. 2009, **131**, p. 6719 6732.

10. Ghosh, S.; Li, X.-Q.; Stepanenko, V.; Wurthner, F. Chem.—Eur. J. 2008, **14**, p. 11343–11357.

11. Shaller, A. D.; Wang, W.; Gan, H. Y.; Li, A. D. Q. Angew. Chem., Int. Ed. 2008, **47**, p. 7705–7709.

12. Langhals, H.; Gold, J. Liebigs Ann./Rec. 1997, p. 1151–1153.

13. Giaimo, J. M.; Lockard, J. V.; Sinks, L. E.; Scott, A. M.; Wilson, T. M.; Wasielewski, M. R. J. Phys. Chem. A 2008, **112**, p. 2322–2330.

14. Veldman, D.; Chopin, S. M. A.; Meskers, S. C. J.; Groeneveld, M. M.; Williams, R. M.; Janssen, R. A. J. J. Phys. Chem. A 2008, **112**, p. 5846–5857.

15. Kawai, T.; Kawamura, K.; Tsumatori, H.; Ishikawa, M.; Naito, M.; Fujiki, M.; Nakashima, T. Chem Phys Chem 2007, **8**, p. 1465–1468.

16. Tsumatori, H.; Nakashima, T.; Kawai, T. Org. Lett. 2011, **12**, p. 2362–2365.

17. Wang, W.; Shaller, A. D.; Li, A. D. Q. J. Am. Chem. Soc. 2008, **130**, p. 8271–8279.

18. Zeidan, T. A.; Hariharan, M.; Siegmund, K.; Lewis, F. D. Photochem. Photobiol. Sci. 2010, **9**, p. 916–922.

19. Hariharan, M.; Zheng, Y.; Long, H.; Zeidan, T. A.; Schatz, G. C.; Vura-Weis, J.; Wasielewski, M. R.; Zuo, X.; Tiede, D. M.; Lewis, F. D. J. Am. Chem. Soc. 2009, **131**, p. 5920–5929.

20. Zheng, Y.; Long, H.; Schatz, G. C.; Lewis, F. D. Chem. Commun. 2005, p. 4795–4797.

21. Witkowski, A.; Moffitt, W. J. Chem. Phys. 1960, **33**, p. 872–875.

22. Fulton, R. L.; Gouterman, M. J. Chem. Phys. 1961, **35**, p. 1059.

23. Fulton, R. L.; Gouterman,M. J. Chem. Phys. 1964, **41**, p. 2280–2286.

24. Weigang, O. E. J. Chem. Phys. 1965, **43**, p. 3609.

25. Weigang, O. E. J. Chem. Phys. 1965, **43**, p. 71.

26. Seibt, J.; Marquetand, P.; Engel, V.; Chen, Z.; Dehm, V.; Wurthner, F. Chem. Phys. 2006, **328**, p. 354–362.

27. Fink, R. F.; Seibt, J.; Engel, V.; Renz,M.; Kaupp,M.; Lochbrunner, S.; Zhao, H. M.; Pfister, J.;Wurthner, F.; Engels, B. J. Am. Chem. Soc. 2008, **130**, p. 12858.

28. Guthmuller, J.; Zutterman, F.; Champagne, B. J. Chem. Phys. 2009, **131**, p. 154302.

29. Gao, F.;Zhao, Y.; Liang,W. J. Phys.Chem. B 2011, **115**, p. 2699–2708.

30. Hoffmann, M.; Soos, Z. G. Phys. Rev. B 2002, **66**, p. 024305.

31. Heinemeyer, U.; Scholz, R.; Gisslen, L.; Alonso, M. I.; Osso, J. O.; Garriga, M.; Hinderhofer, A.; Kytka, M.; Kowarik, S.; Gerlach, A.; Schreiber, F. Phys. Rev. B 2008, **78**, p. 085210.

32. Davydov, A. S. Theory of Molecular Excitons; Plenum Press: New York, 1971.

33. Agranovich, V. M. Excitations in Organic Solids; Oxford University Press: New York, 2009.

34. Spano, F. C.; Yamagata,H. J. Phys. Chem. B 2011, **115**, p. 5133–5143.

35. Holstein, T. Ann. Phys. 1959, **8**, p. 325–342.

36. Wong, C. Y.; Curutchet, C.; Tretiak, S.; Scholes, G. D. J. Chem. Phys. 2009, **130**, p. 081104.

37. Chang, J. C. J. Chem. Phys. 1977, **67**, p. 3901.

38. Patwardhan, S.; Sengupta, S.; Wurthner, F.; Siebbeles, L. D. A.; Grozema, F. J. Phys. Chem. C 2010, **114**, p. 20834–20842.

39. Li, H.; Malinin, S. V.; Tretiak, S.; Chernyak, V. Y. J. Chem. Phys. 2010, **132**, p. 124103.

40. Dunning, T. H. J. Chem. Phys. 1989, **90**, p. 1007–1023.

41. Philpott, M. R. J. Chem. Phys. 1971, **55**, p. 2039–2054.

42. Spano, F. C. J. Chem. Phys. 2002, **116**, p. 5877–5891.

43. Roden, J.; Eisfeld, A.; Dvorak,M.; Bunermann,O.; Stienkemeier, F. J. Chem. Phys. 2011, **134**, p. 054907.

44. Zhao, J.-S.; Ruan, Y.-B.; R., Z.; Jiang, Y.-B. Chem. Sci. 2011, **2**, p. 937–944.

45. Spano, F. C. J. Chem. Phys. 2005, **122**, p. 234701.

46. Spano, F. C. Chem. Phys. 2006, **325**, p. 22–35.

47. Yamagata, H.; Spano, F. C. J. Chem. Phys. 2011, **135**, p. 054906.

48. Taliani, C.; Gebauer, W., Handbook of Oligo and Polythiophenes; Wiley-VCN: Weinheim, Germany, 1999.

49. Petelenz, P.; Andrzejak, M. Chem. Phys. Lett. 2001, **343**, p. 139–142.

50. Sun, X. H.; Zhao, Z.; Spano, F. C.; Beljonne, D.; Cornil, J.; Shuai, Z.; Bredas, J.-L. Adv. Mater. 2003, **15**, p. 818–821.

51. Meinardi, F.; Cerminara,M.; Sassella, A.; Borghesi, A.; Spearman, P.; Bongiovanni, G.; Mura, A.; Tubino, R. Phys. Rev. Lett. 2002, **89**, p. 157403-1–157403-4.

52. Spano, F. C. J. Chem. Phys. 2003, **118**, p. 981–994.

53. Spano, F. C. Annu. Rev. Phys. Chem. 2006, **57**, p. 217–243.

54. Muccini, M.; Schneider, M.; Taliani, C.; Sokolowski, M.; Umbach, E.; Beljonne, D.; Cornil, J.; Bredas, J. L. Phys. Rev. B 2000, **62**, p. 6296–6300.

55. Stradomska, A.; Kulig, W.; Slawik, M.; Petelenz, P. J. Chem. Phys. 2011, **134**, 224505.

56. Yamagata, H.; Norton, J.; Hontz, E.; Olivier, Y.; Beljonne, D.; Bredas, J. L.; Silbey, R. J.; Spano, F. C. J. Chem. Phys. 2011, **134**, p. 204703.

57. Clark, L. B.; Philpott, M. R. J. Chem. Phys. 1970, **53**, p. 3790–3801.

58. Ahn, T. S.; Muller, A. M.; Al-Kaysi, R. O.; Spano, F. C.; Norton, J. E.; Beljonne, D.; Bredas, J. L.; Bardeen, C. J. J. Chem. Phys. 2008, **128**, p. 054505.

59. Lim, S.-H.; Bjorklund, T. G.; Spano, F. C.; Bardeen, C. J. Phys. Rev. Lett. 2004, **92**, p. 107402.

CHAPTER 3

CONTRASTING PHOTOPHYSICAL PROPERTIES OF STAR-SHAPED VS LINEAR PERYLENE DIIMIDE COMPLEXES

3-1 Introduction

Star-shaped complexes of π-conjugated chromophores are currently generating significant interest for use in optoelectronic devices,[1] which take advantage of isotropic absorption[2, 3] and charge transport[4, 5] without the sometimes disadvantageous effects of aggregation. Such molecules are also templates for higher-generation energy-funneling dendrimers, which are of significant interest theoretically[6-8] and practically as active materials for nonlinear optics, catalysis, drug delivery, and sensors.[8-10]

We present here a theoretical analysis of the excited states and absorption spectra of a series of linear and star-shaped covalently linked perylene diimide (PDI) complexes.[11-15] PDI-based chromophores have high quantum yields and well-resolved vibronic spectra and readily self-assemble into a variety of geometries leading to both J- and H-aggregates,[16-18] making them ideal chromophores for studying the impact of aggregation on photophysical properties. Covalently linked PDI complexes also display J- and H-aggregate behavior and serve as model systems with which to study charge transport,[11-19] excimer formation,[20-21] and energy migration.[22-25]

Previously, we conducted a theoretical investigation[26] of absorption and emission in a chiral PDI bichromophore,[27] using a Holstein Hamiltonian with a basis set consisting of single and two-particle states. Electronic couplings were determined from time-dependent density functional (TDDFT) transition charge densities; that study quantitatively accounted for the Davydov splitting observed in the measured absorption

spectrum[27] and showed that the spectral line shapes of the low- and high-energy Davydov components strongly resemble the line shapes expected for J- and H-aggregates, respectively. Here, we extend our investigation to include linear and higher-symmetry PDI complexes.[11-15]

The simplest molecule in the linear series is a head-to-tail dimer in which the two PDI's are covalently linked through the nitrogen head atoms. The addition of another PDI molecule using the same bonding motif results in the linear trimer.[11-13] The nonlinear complexes considered in this work include a cyclic trimer consisting of three PDI chromophores bound to a phenyl core[12, 14] and a tetrahedral complex of phenyl-PDI chromophores linked to a central sp 3-hybridized carbon atom.[12, 15] In such a symmetric series of star-shaped complexes the coupling between the constituent PDI chromophores is characterized by a single value. For example, any of the four chromophores in the tetrahedral complex are coupled to any of the others with the same coupling constant. Note that the dimer is a member of both the linear and symmetric series.

In Ref. 12, Langhals observed that in chloroform solutions of the aforementioned linear and symmetric complexes, the (0−0) peak molar absorptivity exceeds N times the peak absorptivity of monomeric PDI. Here, N is the number of PDI chromophores comprising the complex. Interestingly, the enhancement increases in going from the dimer to linear trimer but decreases in going from the dimer to the cyclic trimer. Such curious observations provided the stimulus for the present work. In what follows, we will show that the linear series exhibits canonical J- aggregate behavior, as expected for a head-to-tail arrangement of chromophores,[28] while the symmetric series shows entirely unique photophysical behavior, neither J- nor H-like. In the linear complexes, oscillator

strength is concentrated in the transition to the lowest energy exciton which is nondegenerate. Absorption and emission are polarized entirely along the long molecular axis. Although the oscillator strength remains concentrated in the lowest energy exciton in the star-shaped trimers and tetramers, the degeneracy of the band-bottom exciton increases in going from the trimer (two-fold degenerate) to the tetramer (three- fold degenerate), leading to polarized absorption and emission along two and three molecular frame axes, respectively. Moreover, in linear trimers and tetramers the energy of the lowest energy exciton red-shifts with increasing N, consistent with what is expected for J-aggregates, whereas in the symmetric series, the lowest energy exciton has no explicit N dependence. As we will find, fundamental differences in the exciton band structure endow the symmetric complexes with photophysical properties differing substantially from linear J-aggregates. With such differences at hand, we will evaluate the impact of molecular nonlinearity on the radiative decay rate and the efficiency of photon absorption, important considerations in solar cell design.

A secondary goal of the current analysis is to rigorously test the accuracy of our theoretical approach for evaluating the absorption spectral line shapes of molecular aggregates.[26] The approach begins with the calculation of the excitonic interactions between PM3-minimized chromophores using TDDFT determined transition-charge densities. The electronic couplings are subsequently inserted into a Holstein-like Hamiltonian for treating vibronic coupling involving the ubiquitous vinyl stretching mode. In what follows, our calculated spectra for the aforementioned PDI complexes will be compared directly to the measured spectra of Langhals et al.[12-15] We will also generalize a previously derived expression[29, 30] for the ratio of 0−0 to 1−0 vibronic line

strengths to include the symmetric PDI complexes. The formula is applicable whenever the exciton bandwidth is smaller than the nuclear relaxation energy and has been successfully applied to aggregates of conjugated polymers,[31] carotenoid assemblies,[32] and, most recently, to chiral PDI complexes.[26]

3-2 Model

In this section, we introduce the Hamiltonian for the geometry optimized PDI complexes shown in Figure 3-1. Since the torsional angle between adjacent PDI chromophores is almost 90°, each PDI can be treated as an individual chromophore within a through-space coupled aggregate; excitations are therefore analogous to Frenkel excitons in molecular aggregates and crystals. In order to account for the linear electron-vibrational coupling involving the progression-forming vinyl stretching mode, we employ a site-based Holstein Hamiltonian, where the nuclear potentials for molecular vibrations in the ground (S_0) and excited (S_1) electronic states are shifted harmonic wells of identical curvature. In the vector subspace containing a single electronic excitation within an aggregate consisting of N PDI chromophores the Hamiltonian is

$$H = \hbar\omega_0 \sum_n b_n^\dagger b_n + \hbar\omega_0 \lambda \sum_n (b_n^\dagger + b_n)|n\rangle\langle n| + \sum_{m,n} J_{mn}|m\rangle\langle n| + \hbar\omega_0 \lambda^2 \tag{3-1}$$

The first term represents the vibrational energy, with the operators $b_n^\dagger$ and b_n, respectively creating and annihilating vibrational excitations in the nth PDI chromophore. The vibrational mode is taken to be the symmetric vinyl stretching mode with $\hbar\omega_0$ = 1400 cm^{-1}. The Huang−Rhys (HR) factor λ^2 is derived from the monomer absorption spectrum

and was determined to be 0.60 (see below). The second term in eq 1 represents the linear vibronic coupling, while the third term represents excitonic coupling, with |n> indicating that chromophore n is in its electronic excited state (S_1) with all other PDI chromophores in their electronic ground states (S_0). J_{mn} is the excitonic coupling between chromophores n and m, and e_{0-0} represents the frequency of the 0−0 transition of the single molecule in solution.

Figure 3-1

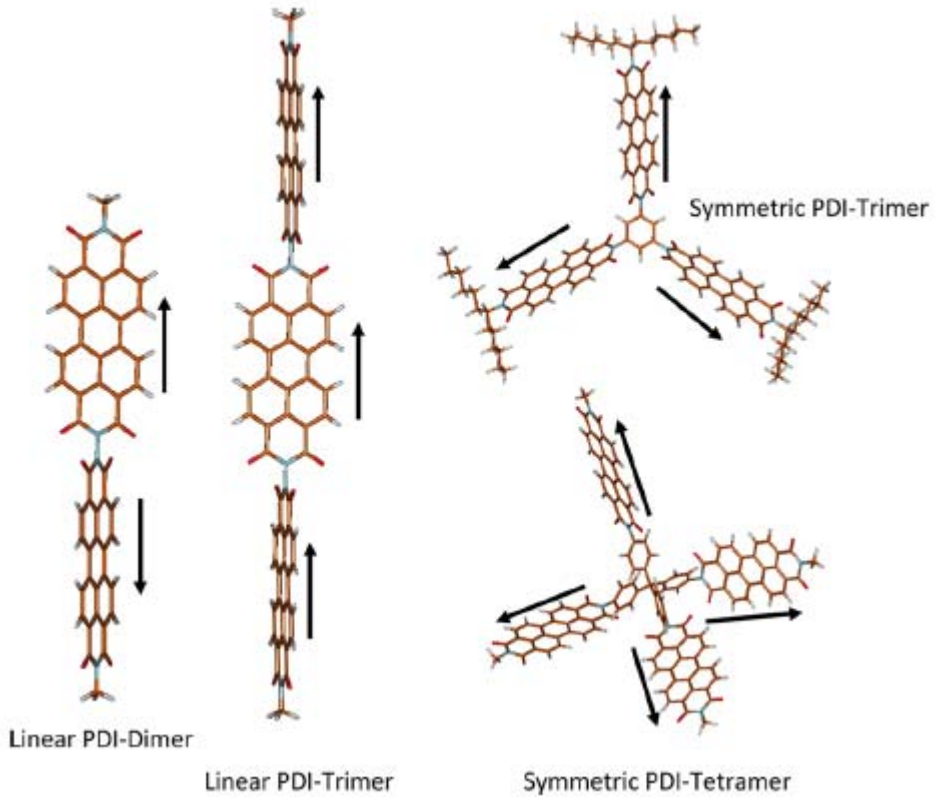

Figure 3-1. Geometry-optimized PDI complexes considered in this work. Also shown is our adapted phase convention, as indicated by the directions of the PDI transition dipole moments.

The basis set used to represent H in eq 3-1 consists of the so-called single- and two-particle states. In a single-particle state, denoted as |n, ṽ>, the nth chromophore is electronically excited with ṽ vibrational quanta in its shifted potential well. The remaining N − 1 chromophores are in their vibrationless ground states. In a two-particle state, denoted |n, ṽ; n′, v′ >, chromophore n is electronically excited with ṽ excited-state vibrational quanta, while molecule n′ is vibrationally excited with v' > 0 vibrational quanta in the shifted potential. The remaining N − 2 chromophores are in their vibrationless ground states. Three-and higher particle states for complexes with three or more chromophores can also be included, but their impact is negligible. The αth eigenstates of H in eq 3-1 can then be expanded as

$$|\Psi^{\alpha}\rangle = \sum_{n,\tilde{v}} c_{n,\tilde{v}}^{(\alpha)} |n,\tilde{v}\rangle + \sum_{n,\tilde{v}} \sum_{n',v'} c_{n,\tilde{v};n',v'}^{(\alpha)} |n,\tilde{v};n',v'\rangle \tag{3-2}$$

The expansion coefficients are readily determined numerically.

The method used here to calculate the excitonic coupling J_{mn} between PDI chromophores m and n has been described previously.[26] We briefly present the important points here. The structure for each of the PDI complexes in this report was optimized at the PM3 level (see Figure 3-1). Then, for each of the symmetric complexes, the N−C bond connecting the PDI to the central core is replaced with a methyl group. (For linear systems, the N−N bond is broken and terminated with a methyl group on each PDI.) If an alkyl chain is also attached to a PDI in the supersystem, it is also replaced by a methyl group. This creates independent N,N-dimethyl PDIs with their original PM3 geometries and orientations present in the super system. Ideally, coupling between these monomers would be calculated as the Coulombic interaction between their respective

monomeric excited-state transition densities, but this would be a rather costly procedure. In order to mimic the spatial qualities of monomeric transition densities on each PDI chromophore, Mullikan population analysis (MPA) is applied to the monomeric transition density of the bright ππ* excited state (S_1) for each PDI. This decomposes the monomeric transition density to point charges localized on each atom of the monomer, mimicking the extent of transition polarization each atom feels in the excitation and capturing much of the spatial character of the transition density. For this study, this was done by expanding the excited-state wave function in terms of its single-excitation Slater determinants and their corresponding CI coefficients from a TDDFT excited-state calculation using the hybrid functional B3LYP and the cc-pVDZ basis set.[36] This method has been used by others for calculating the coupling between carbon nanotubes within the TDDFT regime,[37] and it has been used with other single-reference excited-state methods.[37-40] The PDI transition dipole calculated using this method is on average about 8.4 D, close to the experimental value of 8.5 D. Further details can be found in.[26]

Table 3-1 shows the calculated pairwise electronic couplings within each of the PDI complexes. In the case of the symmetric tetramer discussed in this report, two different sets of monomeric units were generated from the supersystem. One set generated was the N,N-dimethyl PDIs, described above, and the other included the phenyl attached to each PDI and the central carbon of the supersystem, generating four N-methyl-N-phenyl PDI monomers. For this set, the coordinates of the phenyl-PDIs were those from the PM3 structure of the supersystem, with the central C replaced by a reasonable phenyl C−H bond. This was done in order to study the influence of including

the phenyl along with the PDI as a single monomeric chromophore and the effect this has on the coupling and resulting spectral predictions.

Table 3-1

Table 1. J_{mm} for Pairs of Monomer PDIs for Each of the Systems in This Study: Dimer, Symmetric Trimer, and Symmetric Tetramer, Given in eV and cm^{-1} [a]

dimer	J/eV	J/cm^{-1}
J_{12}	0.05842	471.2
symmetric (cyclic) trimer	**J/eV**	**J/cm^{-1}**
J_{12}	0.02689	216.8
J_{13}	0.02654	214.1
J_{23}	0.02672	215.5
linear trimer	**J/eV**	**J/cm^{-1}**
J_{12}	−0.05842	−471.2
J_{13}	−0.00534	−43.0
J_{23}	−0.05846	−471.5

symmetric (tetrahedral) tetramer	J/eV	J/cm^{-1}	J/eV[b]	J/cm^{-1} [b]	PDI-PDI angles	angle/deg
J_{12}	0.01271	102.5	0.01479	119.3	∠12	103.771
J_{13}	0.01084	87.40	0.01315	106.0	∠13	112.301
J_{14}	0.01083	87.36	0.01317	106.2	∠14	113.298
J_{23}	0.01076	86.76	0.01304	105.2	∠23	112.700
J_{24}	0.01084	87.39	0.01312	105.8	∠24	111.987
J_{34}	0.01280	103.3	0.01486	119.9	∠34	103.157

[a]Unless otherwise stated, monomers are *N*,*N*-dimethyl PDIs. Also given for the symmetric tetramer are the angles between the long axes for each pair, in degrees. [b]Monomers are *N*-methyl-*N*-phenyl PDIs.

Table 3-1 shows that the PM3-minimized cyclic trimer and tetrahedral complexes are not fully symmetric, with slight differences in the intermolecular couplings within each complex. However, such differences are certainly smaller than kT at reasonable temperatures, allowing one to safely employ a mean coupling, J_0, to fully describe all interchromophore interactions within a symmetric trimer or tetramer. We verified in our spectral simulations that using the couplings in Table 1 produces spectra indistinguishable from those computed using the mean coupling, J_0, which preserves the symmetry of the complex.

In the symmetric series the wave function phase was chosen so that it is preserved under a rotation, i.e., $\hat{C}_{2,3}|n> = |m>$, where $\hat{C}_2$ and $\hat{C}_3$ are two- and three-fold rotational operations appropriate for the dimer ($\hat{C}_2$) and trimer and tetramer ($\hat{C}_3$). This leads to a

similar relationship among the transition dipole moments $\hat{C}_{2,3}\,\vec{\mu}_m = \vec{\mu}_n$ such that all $\vec{\mu}_n$ point radially away from the molecular center, as indicated in Figure 1. Hence, in a dimer the positive coupling from Table 3-1 ($< 1\,|H|\,2 > \geq J_{12} > 0$) is consistent with the lowest energy exciton of the form, $2^{-1/2}(|1> - |2>)$, which is strongly allowed since the transition dipole moment is, $(\vec{\mu}_1 - \vec{\mu}_2)/(\sqrt{2} \approx \sqrt{2}\vec{\mu}_1)$. By contrast, the higher energy exciton, $2^{-1/2}(|1> + |2>)$ is optically forbidden. The PDI dimer is therefore an ideal J-aggregate. Note from Table 1 that a different but more conventional phase convention is employed for a linear trimer. Here, the phase of the three electronic wave functions |n > (n = 1−3) is chosen such that the transition dipole moments are all parallel and unidirectional $\vec{\mu}_n = |\vec{\mu}_n|\,\hat{x}$, where $\hat{x}$ is a unit vector pointing along the long molecular axis (see Figure 3-1). With this convention the intermolecular couplings are now negative. However, the linear trimer, like the dimer, remains a J-aggregate since the (x-polarized) transition to the lowest energy exciton remains the most strongly allowed.

To begin, we consider the eigenstates and energies of just the excitonic part of the Hamiltonian, the third summation term in eq 3-1. Hence, all energies are relative to the monomer energy, e_{0-0}. For the symmetric series the eigenstates are arranged as shown in Figure 3-2. The lower level is (N − 1)-fold degenerate with energy $-J_0$, while the highest energy nondegenerate exciton has energy $(N - 1)J_0$. Hence, if J_0 were constant throughout the series, the lowest energy would be independent of N, in stark contrast to the linear complexes (see below). In reality, J_0 itself diminishes with N, as shown by our transition-charge density calculations as described above (see Table 1), so that the level structure appears as shown in Figure 3-2. The exciton bandwidth, NJ_0, decreases with N because J_0 decreases faster than 1/N.

Figure 3-2

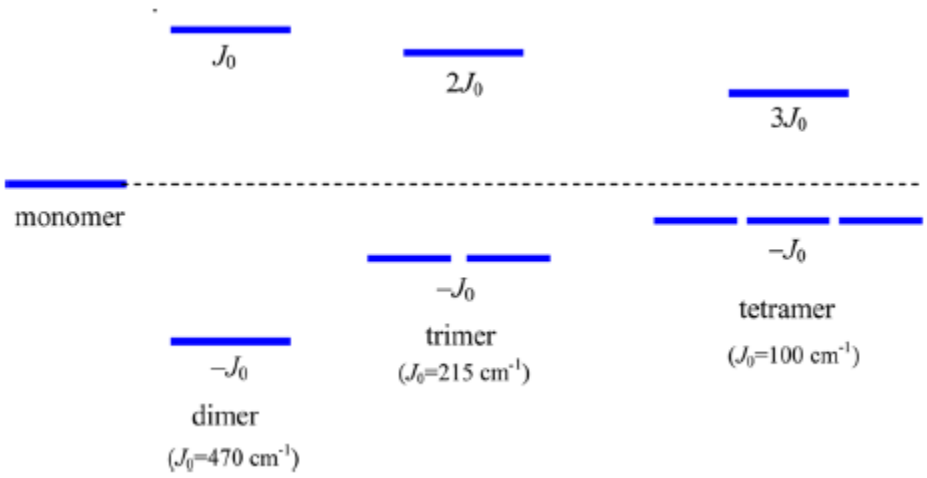

Figure 3-2. Exciton energy levels in the symmetric series of chromophores in the absence of vibronic coupling. For the dimer, trimer, and tetramer, the lower states are optically allowed from the ground state, while the upper state is optically forbidden. Generally, a symmetric N-mer has N−1 degenerate bright states at the band bottom. The unique coupling J_0 is evaluated numerically (see text) and is positive with our chosen phase convention. Note that the exciton bandwidth, N J_0, decreases with increasing N.

The exciton wave functions corresponding to the states in Figure 3-2 are straightforward. The upper level exciton for all complexes in the symmetric series is nondegenerate, consisting of the totally symmetric combination of on site excitations, i.e.,$\Psi_{upper}^{N} = N^{-1/2}\sum_n |n\rangle$. The transition dipole moment is exactly zero, as can be verified by taking a symmetric sum of the radially directed PDI transition dipole moments (see Figure 3-1). For the dimer, the lowest energy exciton is the antisymmetric combination:

$$\psi_{\text{lower}}^{N=2} = \frac{1}{\sqrt{2}}\{|1> - |2>\}; \quad M_{2,x} = \sqrt{2}\,\mu \tag{3-3}$$

where we have indicated the nonzero component of the transition dipole moment, $M_{N,x}$. The lowest energy excitons for the trimer and tetramer are basis functions for the E and T irreducible representations of the D_{3h} and T point groups. Hence, for the cyclic trimer we have wave functions, together with their transition dipole moments are

$$\psi_{\text{lower},x}^{N=3} = \frac{1}{\sqrt{2}}\{|2> - |3>\}; \qquad M_{3,x} = \sqrt{3/2}\,\mu$$
$$\psi_{\text{lower},y}^{N=3} = \frac{1}{\sqrt{6}}\{2|1> - |2> - |3>\}; \quad M_{3,y} = \sqrt{3/2}\,\mu \tag{3-4}$$

The transition dipole moments are evaluated by summing the individual PDI transition dipole moment vectors using the coefficients that appear in the wave function expansion. Finally, for the tetrahedral complex, the triply degenerate states with their transition dipole moments are

$$\psi_{\text{lower},x}^{N=4} = \frac{1}{2}\{|1> - |2> - |3> + |4>\}; \quad M_{4,x} = \sqrt{4/3}\,\mu$$
$$\psi_{\text{lower},y}^{N=4} = \frac{1}{2}\{|1> - |2> + |3> - |4>\}; \quad M_{4,y} = \sqrt{4/3}\,\mu$$
$$\psi_{\text{lower},z}^{N=4} = \frac{1}{2}\{|1> + |2> - |3> - |4>\}; \quad M_{4,z} = \sqrt{4/3}\,\mu \tag{3-5}$$

For the linear series the eigenspectra are quite different. Here, we consider nearest-neighbor coupling only, also designated as J_0, which is now negative ($J_0 < 0$), consistent with the usual phase convention for linear aggregates. The dimer's eigenspectrum was already discussed as a member of the symmetric series. For the linear (J-) aggregates with $N > 2$, the exciton energies (relative to the monomer e_{0-0}) are given by

$$\varepsilon_k^N = -2|J_0|\cos(k\pi/N+1), \quad N > 2$$

(3-6)

where k indexes the eigenstates, k = 1, ..., N. The band structure is depicted in Figure 3-3. All eigenstates are nondegenerate.

Figure 3-3

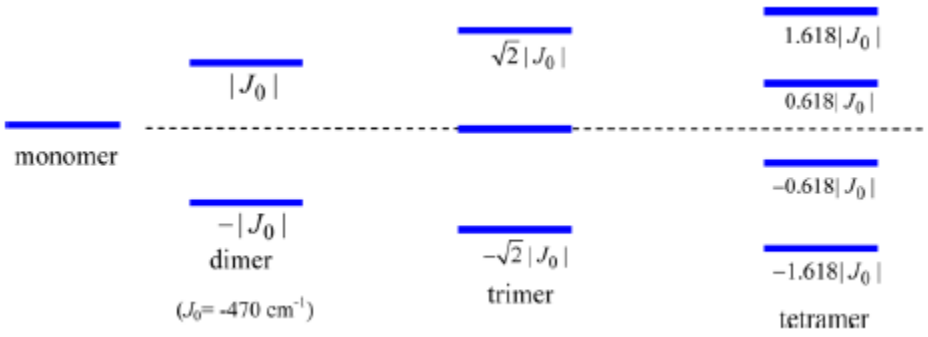

Figure 3-3. Exciton energy levels in the linear series of chromophores assuming nearest-neighbor-only coupling equal to J_0 and no vibronic coupling. Unlike the symmetric series, the value of J_0 remains constant throughout the series and the red shift of the lowest energy exciton increase with N. Consistent with our chosen phase convention for linear complexes, J_0 is negative (see text). In all cases the lowest energy exciton is the most strongly allowed from the ground state. Such complexes therefore behave as ideal J-aggregates.

The wave functions, together with their transition dipole moments are

$$\psi_{\text{linear},k}^N = \sqrt{\frac{2}{N+1}} \sum_n \sin\frac{n\pi k}{N+1} \Big| n>$$

(3-7)

$$M_{N,k,x} = \sqrt{\frac{2}{N+1}} \cot\left(\frac{\pi k}{2(N+1)}\right)\mu; \quad k = 1, 3$$
$$M_{N,k,x} = 0 \qquad\qquad k = 2, 4$$

(3-8)

eq 3-8 shows that the line strength is mainly concentrated in the lowest energy exciton (k = 1), consistent with J-aggregation. This is readily seen in the limit N ≫ 1, where

$$|M_{N,1,x}|^2 \approx 8\mu^2(N+1)/\pi^2$$

(3-9)

The scaling of the squared transition dipole moment with N is a signature of superradiance.

3-3 Comparison to Experiment

Figure 3-4 shows the experimental absorption spectra of the symmetric series of PDI complexes dissolved in chloroform as measured by Langhals et al.[12-15] In monomeric PDI, the vibronic peaks labeled as n−0 (n = 0, 1, 2, ...) correspond to transitions from the vibrationless electronic ground state (S_0) to the electronic excited state (S1) with n vibrational quanta (i.e., $S_1(n) \leftarrow S_0(0)$). In higher complexes the origin of the peaks is more complex, but we retain the same notation.

The spectral intensity in Figure 3-4a is in units of molar absorptivity. Hence, if the interactions between PDI chromophores were absent, the spectrum for the N-mer would be approximately N times the monomer spectrum shown in black. As pointed out by (citation Langhals 12) the spectra in Figure 4 are peculiar in that the peak 0−0 absorptivity for an N-mer, significantly exceeds N times that of the monomer. The

enhancement is ~1.39 in the dimer but diminishes with increasing N; for the symmetric trimer and tetramer the enhancement is respectively, 1.1 and 1.07. To check whether the enhanced peak height is due to increased oscillator strength in the 0−0 transition, one should determine how the 0−0 spectral area of the N-mer compares to the monomer. This is particularly important because the 0−0 line width (or, more generally, the line shape) is not uniform throughout the symmetric series. The line asymmetry is mainly due to the presence of additional low-frequency vibrations (<600 cm^{-1}) which have been identified in PDI monomers[41] and derivatives thereof. [42] To estimate the spectral areas, we fit the measured absorption spectrum for each of the chromophores using displaced Gaussians. The fitted spectra are drawn alongside the measured spectra in Figure 3-4a. (Further details of the fitting procedure are contained in the SI.)Using the fittedGaussians, we computed the spectral area of the 0−0 line normalized to N times the corresponding monomer value

$$\mathrm{SA}_N \equiv \frac{\int A_N^{0-0}(\omega)\mathrm{d}\omega}{N\int A_{mon}^{0-0}(\omega)\mathrm{d}\omega} \tag{3-10}$$

The results are collected in Table 3-2, alongside the mean excitonic couplings from Table 3-1. The Table shows that the normalized 0−0 oscillator strength does indeed exceed N times the monomer in a manner which decreases with increasing N in the symmetric series.

Table 3-2 Experimental 0−0 Spectral Areas Normalized to *N* Times the Monomer 0−0 Spectral Area for the Symmetric Series[a]

	mean excitonic coupling, J_0 (cm^{-1})	normalized 0−0 spectral area, SA_N (exp)	normalized 0−0 oscillator strength (eq 15)
dimer	471	1.23	1.19
trimer	215	1.07	1.09
tetramer	92 (110)	1.05	1.04 (1.05)

[a] Also shown are the calculated 0−0 oscillator strengths (similarly normalized) using the mean couplings from column one. Values in parentheses correspond to the tetramer composed of PDI-phenylchromophores (see Table 3-1).

The observed decrease in the 0−0 oscillator strengths with N correlates with the diminishing value of J_0 with increasing N as shown in Table 3-2. To better understand the nature of the effect, we calculated the absorption spectrum for an isotropic distribution of N-mers using

$$A_N(\omega) = \sum_{j=x,y,z} \sum_{\alpha} f_{G,\alpha}^{(j)} W_{\mathrm{LS}}(\omega - \omega_\alpha) \tag{3-11}$$

eq 3-11 contains the (normalized) j-polarized oscillator strength from the vibrationless electronic ground state |G> to the αth excited state |ψ(α)>,

$$f_{G,\alpha}^{(j)} \equiv E_\alpha |\langle G|\hat{\mathrm{M}}_j|\psi^{(\alpha)}\rangle|^2 \tag{3-12}$$

Figure 3-4

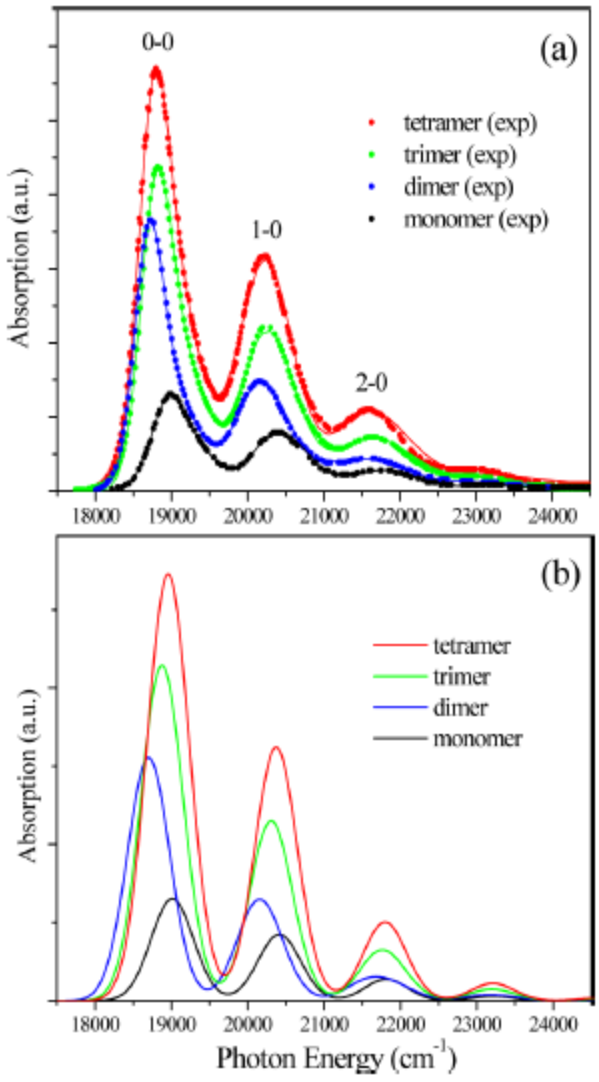

Figure 3-4. (a) Measured (dots) and fitted (lines) absorption spectra ofthe symmetric series of PDI complexes. (b) Calculated spectra using aGaussian line shape in eq 11 with a full width (at the 1/e point) of 800cm^{-1} (see text for details).

where Eα = ħωα is the transition energy to state α and $\hat{M}_j$ is the jth component of the transition dipole moment (tdm) operator, defined as

$$\hat{\mathrm{M}}_j \equiv \sum_{n=1,N} \{|g><n| + |n><g|\}\mu_{n,j}$$

(3-13)

In eq 3-11, $\mu_{n,j}$ is the jth component of the transition dipole moment of the nth chromophore of the complex (see Figure 3-1), referred to the molecular frame. In eq 3-13, $|g\rangle \equiv |g_1, g_2, ..., g_N\rangle$, is the pure electronic ground state of the complex. Hence, $|G\rangle$ is the product of $|g\rangle$ and the vacuum vibrational state in which all N oscillators are in the lowest level of the S_0 nuclear potential. Finally, WLS in eq 3-11 is a symmetric line shape function, taken here to be Gaussian.

The absorption spectrum as written in eq 3-11 correctly identifies the absorption line strength to a particular state α with the oscillator strength in eq 3-12. In our previous works we based our analysis on an absorption line strength depending solely on the square of the transition dipole moment, i.e., lacking the transition energy dependence in eq 3-12. Such an approximation is consistent with a Poissonian distribution of 0−n line strengths in the monomer spectrum, as is normally assumed.(citation 43) However, as shown in detail in the SI, the error incurred in neglecting the energy dependence is entirely negligible - at most a few percent - basically because the vibrational energy ($\hbar\omega 0$) is far smaller than the 0−0 optical transition energy, e_{0-0}.

For an isotropic distribution of PDI monomers eq 3-11 reduces to

$$A_{\mathrm{mon}}(\omega) = \mu^2 \sum_{n=0,1,2,..} \{(\omega_{0-0}^{\mathrm{mon}} + n\omega_0)\lambda^{2n} e^{-\lambda^2}/n!\} W_{\mathrm{LS}}(\omega - \omega_{0-0} - n\omega_0)$$

(3-14)

a Poissonian distribution slightly weighted by the aforementioned peak energy dependence. From the measured monomer absorption spectrum we have, $e_{0-0}^{mon} \equiv \hbar\omega_{0-0}^{mon}$

= 19 000 cm^{-1}, $\hbar\omega_0$ = 1400 cm^{-1}, and 1.54 for the ratio of the 0−0 to 1−0 peak areas. Inserting these values in eq 3-14 gives the best fit HR factor to be $\lambda^2 = 0.60$.

Based on eqs 35−38 the 0−0 oscillator strength of the symmetric N-mer, $I_{A,N}^{0-0}$, normalized to N times the 0−0 line strength of the monomer is given by

$$\frac{I_{A,N}^{0-0}}{NI_{A,\mathrm{mon}}^{0-0}} \equiv \frac{\sum_{\alpha=1,\ldots,N-1}\sum_j f_{G,\alpha}^{(j)}}{Ne_{0-0}^{\mathrm{mon}}e^{-\lambda^2}\mu^2} \approx \frac{(N-1)|<G|\hat{\mathrm{M}}_x|\psi^{(\alpha=1)}>|^2}{Ne^{-\lambda^2}\mu^2} \tag{3-15}$$

The first sum runs over the N − 1 degenerate excitons comprising the lowest energy level with polarizations assumed in the order x,y,z. Hence, the N − 1 prefactor accounts for the equivalent contributions from the additional polarization components (y and z) encountered when N ≥ 2. Note that the theoretical enhancement reduces to unity in the limit of vanishing coupling between PDI chromophores. In this case,

$$|<G|\hat{\mathrm{M}}_x|\psi^{(\alpha=1)}>|^2 = e^{-\lambda^2}|M_{N,x}|^2 = e^{-\lambda^2}\mu^2 N/(N-1) \tag{3-16}$$

where the MN,x are given in eqs 27−29. Substitution of eq 40 into eq 39 yields $I_{A,N}^{0-0}/NI_{A,mon}^{0-0}$= 1.

Table 3-2 also reports the ratios $I_{A,N}^{0-0}/NI_{A,mon}^{0-0}$ calculated using eq 3-15 with the αth wave function computed by diagonalizing the Holstein Hamiltonian in eq 3-1 using the mean of the excitonic couplings from Table 3-2. The calculated values agree quite well with the measured values. As expected, the enhancement correlates with the strength of the exciton coupling, J_0.

Such an aggregation-induced enhancement of the 0−0 oscillator strength is also a property of linear J-aggregates, containing one molecule per unit cell. (citation 30) Although the dimer is certainly a J-aggregate, the symmetric trimer and tetramer are not, since the lowest energy exciton is degenerate. Moreover, the 0−0 oscillator strength, although enhanced relative to the monomer, decreases in going from N = 2 to 4 since J_0 (see Table 3-2) itself decreases. This trend opposes what is found in linear J-aggregates, as we show below.

Because the oscillator sum rule requires that the enhanced 0−0 oscillator strength must come at the expense of the oscillator strength residing in the side-bands (1−0, 2−0, ...), a better indicator of J-like behavior is an increase in the ratio of the 0−0 to 1−0 oscillator strengths, R ≡ $I_{A,N}^{0-0}/I_{A,N}^{1-0}$, with increased exciton coupling. (citation 30) Using the fitted spectra in Figure 3-4a we evaluated R_{abs} from the 0−0 and 1−0 spectral areas. The results appear in Table 3-3 and Figure 3-5a. Rabs is largest in the dimer, subsequently diminishing in going to the (symmetric) trimer and then to the tetramer, as J_0 also diminishes.

Table 3 - 3 Experimental and Theoretical 0−0/1−0 Oscillator Strength Ratios, R_{abs}, for the Symmetric Series[a]

	monomer	dimer	trimer (S)	tetramer (S)
experimental R_{abs}	1.54	2.30	1.85	1.72
calculated R_{abs} (SP and TP)	1.54	2.26	1.85	1.68 (1.70)
calculated R_{abs} (SP only)	1.54	2.63	1.98	1.71 (1.75)
R_{abs} (perturbation theory)		2.70	1.98	1.71 (1.75)

[a]Calculated values of R_{abs} employ the mean couplings in Table 3-2. The most accurate calculation uses all single particle (SP) and two-particle (TP) basis functions. The perturbative calculations are discussed in Section 3-4 and are based on eq 47 using the couplings in Table 3-2.

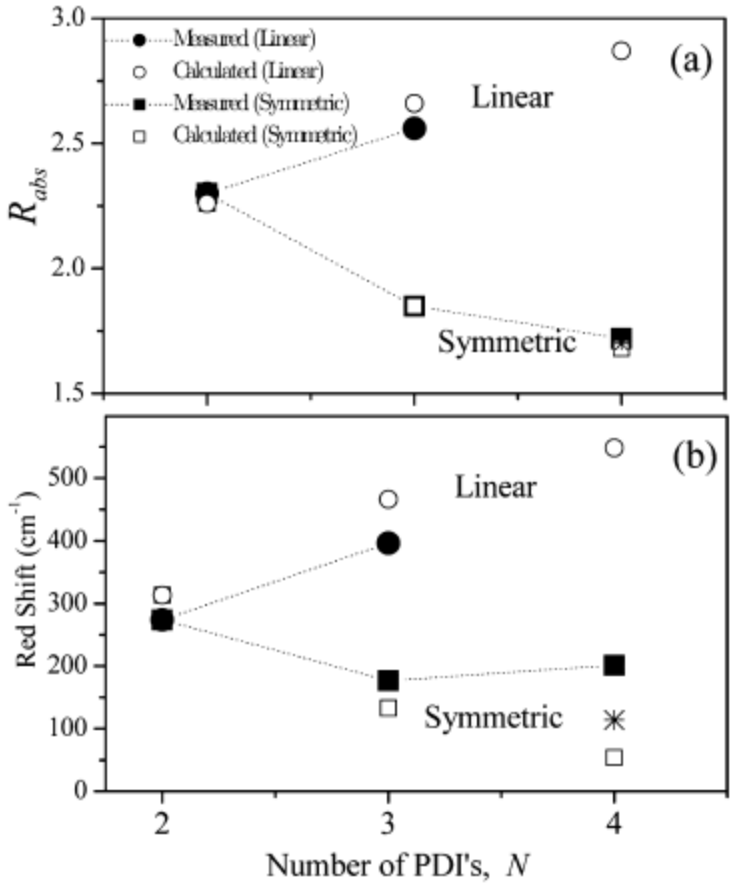

Figure 3-5. Measured and computed values of (a) R_{abs} and (b) the 0−0 spectral red-shift (relative to the monomer) in both the linear and symmetric series. Dotted lines connect the measured values. Computed shifts utilize the mean couplings in Table 3-2 for the symmetric series and the nearest-neighbor couplings in Table 3-4 for the linear series. All computations assume PDI complexes except the phenyl-PDI tetrahedral complex indicated by the asterisk (at N = 4).

The calculated values of R_{abs}, based on eigenstates and energies evaluated from the Hamiltonian in eq 25 with mean couplings taken from Table 3-2, are also shown in Table 3-3. Here, $I_{A,N}^{0-0}(I_{A,N}^{1-0})$ is obtained by summing $f_{G,\alpha}^{(j)}$ over all j and α, such that E_α lies within the 0−0 (1−0) bands. Table 2-3 and Figure 3-5a show that the agreement the calculated and measured R_{abs} values is excellent.

We conclude our analysis of Langhal's symmetric series with Figure 3-5b, which shows the measured red-shift of the main 0−0 spectral peak relative to the monomer peak as a function of N. Traditionally, such spectral shifts have been used to extract the excitonic couplings. Comparison of the Langhals' data in Figure 3-5a,b shows that the spectral shifts are strongly correlated to R_{abs}. Thus, within the symmetric series, the dimer undergoes the largest red-shift, followed by the cyclic trimer. The reduction in the red-shift (and Rabs) in going from N = 2 and 3, coincides with the decrease in the TDDFT-calculated excitonic coupling J_0 (see Tables 3-1 and 3-2). The tetramer red-shift breaks the downward trend, being slightly greater than the trimer red-shift. This is likely due to the fact that the tetrahedral complexes of Langhals are composed of phenyl-PDI units (and not just PDI units as in the trimer) in which e_{0-0} is reduced due to dispersion effects, as enhanced conjugation is effectively eliminated due to the large dihedral angles between the phenyl and PDI groups (see Figure 3-1) .We note that the phenyl core within the trimer is expected to have a much smaller impact since there is only a single phenyl group per complex, and it is similarly disconnected from the PDI groups due to large dihedral angles.

Figure 3-5b also shows that our computed red shifts agree well with the measurements of Langhals. The calculated 60 cm^{-1} increase in the red-shift in the phenyl-PDI tetramer vs the PDI tetramer (the asterisk vs open square) is almost enough to account for the enhancement of the red-shift of the symmetric tetramer observed by Langhals. Figure 3-5a also shows that the ratio Rabs is practically independent of the extra phenyl group.

We now consider the linear series of PDI complexes which should behave as ideal J-aggregates. Figure 3-6a depicts the experimental spectra of Langhals et al. (citation 12,13) along with our fitted spectra. Once again, as pointed out by Langhals, the 0−0 peak of the N-mer is enhanced relative to N times the 0−0 peak in the monomer. Figure 3-6b shows the calculated spectra based on the Hamiltonian in eq 3-1 and the spectrum in eq 3-11. The experimental enhancements of the 0−0 oscillator strength based on the fitted areas are tabulated in Table 3-4 alongside our calculated quantities.

Figure 3-6

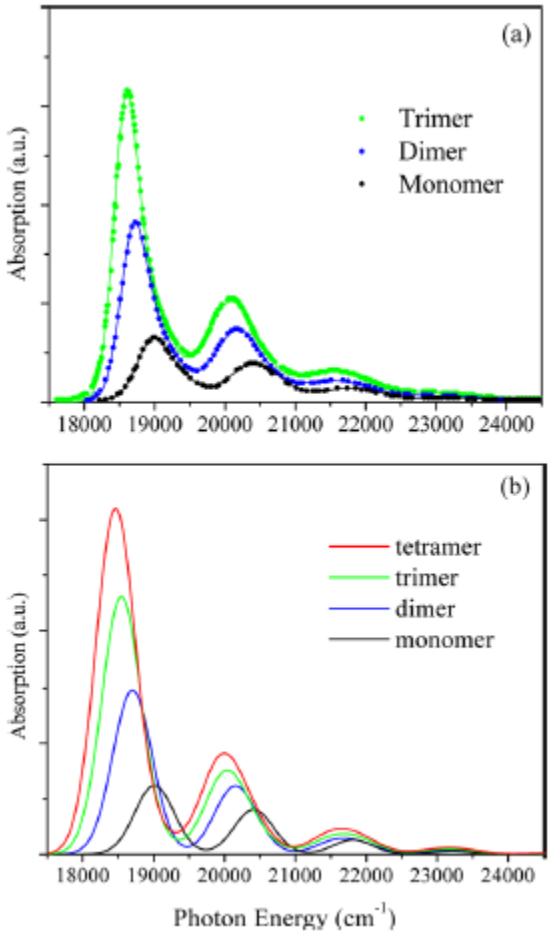

Figure 3-6. (a) Measured (dots) and fitted (lines) absorption spectra of the linear series of PDI complexes. (b) Calculated spectra using a Gaussian line shape in eq 3-11 with a full width (at 1/e) of 800 cm^{-1} (see text for details).

Table 3-4 Experimental 0–0 Spectral Areas Normalized to *N* Times the Monomer 0–0 Spectral Area for the Linear Series[a]

	nearest-neighbor excitonic coupling (cm^{-1})	normalized 0–0 SA_N (exp)	normalized 0–0 oscillator strength (calculated)
dimer	−471	1.23	1.19
trimer	−471	1.34	1.26
tetramer	−471	—	1.30

[a]Also shown are the calculated 0–0 oscillator strengths (similarly normalized).

In direct contrast to the symmetric series, the enhancement of the 0−0 peak in the linear trimer exceeds that in the dimer, as expected for J-aggregates. The trend is supported by our calculations up through the tetramer and correlates with a similar increase in the observed and calculated values of R_{abs}, as can be appreciated from Table 3-5 and Figure 3-5a. The behavior also correlates to an increase in the observed and calculated excitonic red-shift with N as shown in Figure 3-5b. The origin of the N-dependent shift can be traced back to the free-exciton regime of eq 3-6, where the k = 1 exciton's energy is given by, $-2|J_0|\cos(\pi/N + 1)$, see also Figure 3-3. The initial increase in the red shift with N directly contrasts what is found in the symmetric series (see Figure 3-5b) where the free-exciton energy is simply $-J_0$, with J_0 decreasing as N increases.

Table 3 - 5. Experimental and Theoretical 0−0/1−0 Integrated Line Strength Ratios for the Linear Series[a]

	monomer	dimer	trimer (L)	tetramer (L)
experimental R_{abs}	1.54	2.30	2.56	—
calculated R_{abs} (SP and TP)	1.54	2.26	2.66	2.87
calculated R_{abs} (SP only)	1.54	2.63	3.20	3.48
R_{abs} (perturbation theory)	—	2.65	3.26	3.60

[a]The most accurate calculation uses all SP and TP basis functions. The perturbative calculations are discussed in Section 4 and are based on eq 23.

In order to make a fairer comparison of the photophysical properties displayed by linear vs symmetric complexes we plot in Figure 3-7 the calculated values of R_{abs} vs $|J_0|$ for all of the complexes considered so far. The figure shows that in both series the ratio increases with $|J_0|$, as expected, with the linear complexes significantly exceeding their symmetric counterparts for a given $|J_0|$. Interestingly, the symmetric series is far less sensitive to J_0 and appears to converge with increasing J_0. The ratio also converges in the linear series to the value of $N/(r_\omega \lambda^2)$ (but for larger values of $|J_0|$ than shown in Figure 3-7) as can be determined using Born−Oppenheimer approximation. (Here, r_ω is the ratio of the 1−0 and 0−0 peak absorption frequencies and is close to unity). For the symmetric series the converged value is approximately $N/[(N-1)\, r_\omega\, \lambda^2]$, obtained by replacing N in the linear series with $N/(N-1)$ in the symmetric series.

Figure 3-7

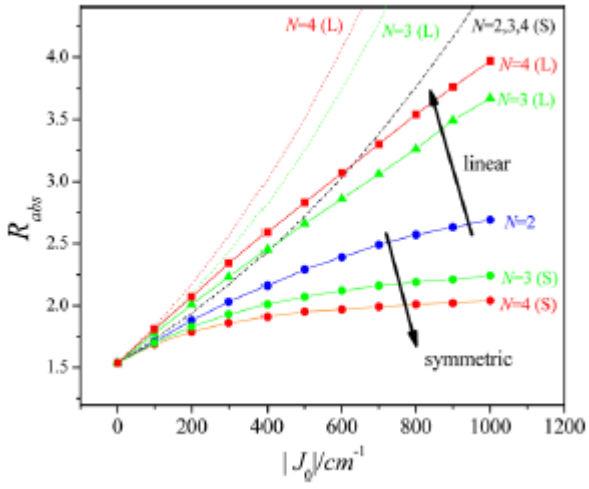

Figure 3-7. Calculated ratio of 0−0 and 1−0 oscillator strengths for the linear and symmetric series as a function of $|J_0|$ using $\lambda^2 = 0.60$. In the linear series the nearest-neighbor approximation was invoked with nearest-neighbor coupling equal to J_0 in Table 2. Dotted curves represent the single-particle approximation.

For a given value of $|J_0|$, opposite trends are observed with increasing N for the two series. Whereas R_{abs} increases with N in the linear series as expected for J-aggregates, it decreases with N in the symmetric series. Although the former dependence can be traced back to an increasing exciton bandwidth with N, the latter effect is quite unusual and arises entirely from two-particle states. This is readily appreciated from the curves in Figure 3-7 which are based on the single-particle approximation. In the symmetric series there is no N dependence at the single-particle level, ultimately due to the lack of any N dependence in the excitonic contribution to the energy of the optically allowed level. Hence, two-particle states have a more profound impact for complexes within the symmetric series.

3-4. Weak Coupling Limit: The Ratio Formula

In this section we account for the observations in Section 3-3 by treating the excitonic Hamiltonian, H_{ex}, (third summation term in eq 3-1) as a perturbation, valid in the limit of weak excitonic coupling, $|J_0| \ll \lambda^2 \hbar\omega_0$ The inequality is roughly satisfied by all of the PDI complexes considered so far. To zero-order in $|J_0|/\hbar\omega_0$, the eigenstates are divided into vibronic bands identified by the number of vibrational quanta, $\tilde{v} = 0, 1, 2, \ldots$, defining the majority single-particle state. We begin our analysis with the symmetric series of chromophores, where the first-order corrected energies for the optically allowed levels are

$$E_{\tilde{v}} = e_{0-0} + \hbar\omega_0\tilde{v} - J_0\lambda^{2\tilde{v}}e^{-\lambda^2}/\tilde{v}!, \qquad \tilde{v} = 0, 1, 2, \ldots \tag{3-17}$$

Note that the levels in eq 3-17 are (N − 1)-fold degenerate but otherwise do not depend on N. The associated zero-order wave functions are symmetry-adapted single-particle states resembling the excitonic wave functions in eqs 3-3 to 3-5. To first-order, like symmetry states in different bands couple together so that $\tilde{v}$is no longer a good quantum number. Such interband coupling was discussed in detail in refs (citation 29 and 44) for the case of linear aggregates. First-order coupling also connects the zero-order states with two-particle states, but the latter are dark and do not directly contribute to the absorption spectrum; Their impact is felt at higher orders. The first-order corrected wave functions for the j-polarized optically allowed excitons are

$$|\psi_{\tilde{\nu},j}> \approx |\varphi_j, \tilde{\nu}> + \sum_{\tilde{\nu}' \neq \tilde{\nu}} \frac{<\varphi_j, \tilde{\nu}'|H_{ex}|\varphi_j, \tilde{\nu}>}{\hbar\omega_0(\tilde{\nu} - \tilde{\nu}')} |\varphi_j, \tilde{\nu}'>$$

$$\tilde{\nu} = 0, 1, 2, \ldots$$

(3-18)

where j = x for the dimer, j = x and y for the cyclic trimer, and j = x, y, and z for the tetrahedral complex, reflecting the increasing degeneracy of each vibronic level. The zero-order states $|\varphi_j,\tilde{\nu}>$ in eq 3-18 are delocalized single-particle states with expansion coefficients, which come from the diagonalization of H_{ex} and, hence, are identical to those appearing in eqs 3−5. So, for example, in the tetrahedral complex the three degenerate zero-order excitons in the $\tilde{\nu}$ band are

$$\left|\varphi_x, \tilde{\nu}> = \frac{1}{2}\{\right|1, \tilde{\nu}> - |2, \tilde{\nu}> - |3, \tilde{\nu}> + |4, \tilde{\nu}> \}$$

(3-19a)

$$\left|\varphi_y, \tilde{\nu}> = \frac{1}{2}\{\right|1, \tilde{\nu}> - |2, \tilde{\nu}> + |3, \tilde{\nu}> - |4, \tilde{\nu}> \}$$

(3-19b)

$$\left|\varphi_z, \tilde{\nu}> = \frac{1}{2}\{\right|1, \tilde{\nu}> + |2, \tilde{\nu}> - |3, \tilde{\nu}> - |4, \tilde{\nu}> \}$$

(3-19c)

which are reminiscent of the sp^3-hybridized orbitals in tetrahedral carbon. (The fourth orbital corresponds to the higher energy optically forbidden exciton, see Figure 3-2.) Transitions to the excitons $|\psi, \tilde{\nu}_{=0,j}>$ contribute to the 0−0 absorption band, while transitions to the excitons $|\psi, \tilde{\nu}_{=1,j}>$ contribute to the 1−0 absorption band.

To first order in ($J_0/(\hbar\omega_0)$) the 0−0/1−0 oscillator strength ratio, R_{abs}, is therefore

$$R_{\text{abs}} = \frac{E_{\tilde{v}=0} \sum_j | < G|\hat{M}_j|\psi_{\tilde{v}=0,j} > |^2}{E_{v=1} \sum_j | < G|\hat{M}_j|\psi_{v=1,j} > |^2} \tag{3-20}$$

After inserting the wave function in eq 3-18 into eq 3-20 one obtains, after some additional simplification, the final expression

$$R_{\text{abs}} = \frac{1}{\lambda^2 r_\omega}\left[\frac{(1 + G(0; \lambda^2)e^{-\lambda^2}J_0/\hbar\omega_0)}{(1 + G(1; \lambda^2)e^{-\lambda^2}J_0/\hbar\omega_0)}\right]^2, \quad N = 2-4 \tag{3-21}$$

where $J_0 > 0$. The vibronic factors appearing in eq 3-21 are given by (citation 29)

$$G(\tilde{v}; \lambda^2) \equiv \sum_{\substack{\tilde{v}'=0,1,2\ldots \\ \tilde{v}'(\neq\tilde{v})}} \frac{\lambda^{2\tilde{v}'}}{\tilde{v}'!(\tilde{v}' - \tilde{v})} \tag{3-22}$$

The factor rω appearing in eq 3-21 arises from the transition frequency dependence of the oscillator strength. It is essentially the ratio of the 1−0 and 0−0 peak absorption frequencies in the monomer, which, for the present case is close to unity, $r_\omega \approx 1.07$. Our previous ratio expression[29] lacks r_ω, and it might be expected the deviation from the more accurate ratio in eq 3-21 is about 7% in the present case. The error is in fact much smaller, because neglecting the frequency dependence of the oscillator strength forces a slightly larger HR factor, equal to $\lambda^2 r_\omega$, to reproduce R_{abs} in the monomer spectrum.

Eq 3-21 (without r_ω) reduces to our previous expression for linear aggregates with periodic boundary conditions if the excitonic energy of the optically allowed (free-) exciton, $-J_0$ in eq 3-21, is replaced by the excitonic energy of the k = 0 exciton in the linear complex, $\tilde{J}_{k=0} \equiv \Sigma_n J_{mn}$, where the sum includes all neighbors (the two nearest and beyond) in the linear chain.[30] Hence, in all cases the ratio strictly depends on the excitonic shift of the optically allowed exciton, the magnitude of which is equal to half the exciton bandwidth only under the nearest-neighbor-only approximation.

When the HR factor for monomeric PDI, $\lambda^2 = 0.60$, is inserted into eq 3-22 we obtain, G(0;0.60) = 0.703 and G(1;0.60) = −0.800. inserting these quantities into eq 3-21 gives the final first-order expression for the PDI symmetric series:

$$R_{abs} = 1.54\left[\frac{(1 + 0.386J_0/\hbar\omega_0)}{(1 - 0.439J_0/\hbar\omega_0)}\right]^2, \quad N = 2-4 \tag{3-23}$$

Since $J_0 > 0$, R_{abs} increases with J_0, as is also the case of J-aggregates. Unlike J-aggregates, however, there is no N dependence. The accuracy of eq 3-23 can be gauged from Tables 3-3 and 3-5. Figure 3-8 shows R_{abs} plotted for small values of $|J_0|$ for the symmetric and linear series. The figure shows the ratios calculated fully numerically (including single- and two-particle basis functions) and by using the first-order expression in eq 3-23. The latter works quite well when $J_0 < 100$ cm^{-1}. In the symmetric series there is practically no N dependence over the first 50 cm^{-1}, as predicted by eq 3-23. This can be ultimately traced back to the independence of the lowest exciton energy on N; see eq 3-17. For higher coupling strengths the ratio acquires an N dependence, being

larger for the dimer and smallest for the tetramer. The N dependence arises entirely from the increased contribution of two-particle states, as discussed in the previous section.

Figure 3-8

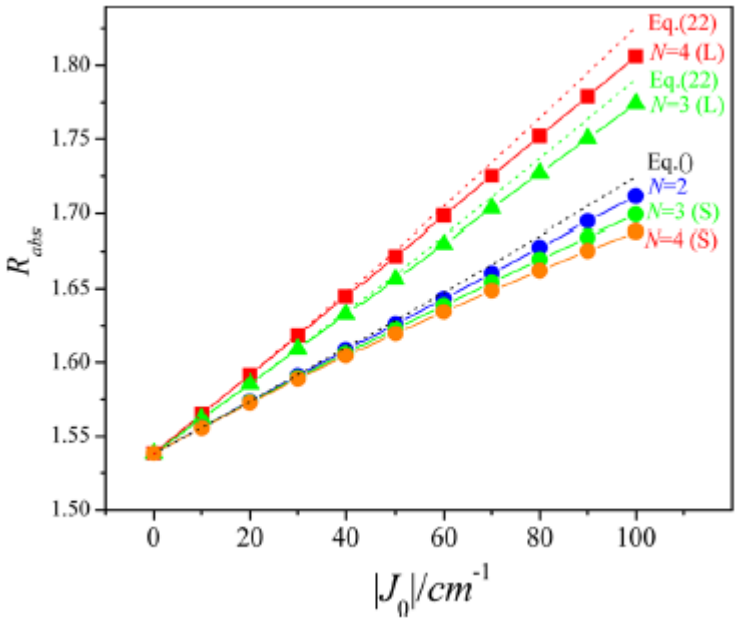

Figure 3-8. Calculated ratio of 0−0 and 1−0 oscillator strengths for the linear and symmetric series as a function of J_0. In the linear series the nearest-neighbor approximation was invoked with nearest-neighbor coupling equal to J_0. Dotted curves represent the perturbative expressions (see text).

The perturbation theory result for the linear series is more complex than its symmetric series counterpart, since oscillator strength is divided among the k = 1 and 3 excitons for both the N = 3 and 4 complexes (see eq 3-8). The division is purely a result of open boundary conditions. Assuming only nearest-neighbor coupling equal to $-|J_0|$ we obtain

$$R_{abs}(N) = \frac{1}{\lambda^2 r_\omega} \left[\frac{\sum_{k=1,3} M^2_{N,k,x}(1 - G(0; \lambda^2)e^{-\lambda^2}\varepsilon_k^N/\hbar\omega_0)^2}{\sum_{k=1,3} M^2_{N,k,x}(1 - G(1; \lambda^2)e^{-\lambda^2}\varepsilon_k^N/\hbar\omega_0)^2} \right]$$

(3-24)

which now depends on N through the transition dipole moments and energies from eq 3-6. Since the energies are negative, eq 3-24 predicts J-aggregate behavior, with Rabs increasing with $|J_0|$. The ratios calculated using eq 3-24 are also plotted in Figure 3-8.

The initial linear rise of R_{abs} with $|J_0|$ is identical for all of the molecules in the symmetric series and is significantly smaller than the initial rise displayed by the linear trimer and tetramer. Using eqs 3-21 and 3-24 the initial slopes of all curves in Figure 3-8 are given by

$$\frac{dR_{abs}}{d|J_0|} = 2b\{G(0, \lambda^2) - G(1, \lambda^2)\}e^{-\lambda^2}/\hbar\omega_0\lambda^2 r_\omega$$

(3-25)

where the prefactor b is unity for all molecules in the symmetric series. For the linear trimer and tetramer b is, respectively, 1.33 and 1.55 and reflects the increase in the magnitude of the excitonic shift of the band bottom exciton with N. In the limit of large N, b approaches the value of two in the linear series since in this limit the lowest energy exciton approaches $-2|J_0|$ (see eq 3-6), twice as large (in magnitude) as what is found in the symmetric complexes.

3-5. Dicussion and Conclusion

The photophysical properties of symmetric star-shaped chromophores are markedly different from their linear counter-parts. The latter behave as J-aggregates, with oscillator strength concentrated in the transition to the lowest energy, non-degenerate exciton. The oscillator strength is linear with the number of chromophores N, which leads to superradiance at sufficiently low temperatures. By contrast, in the symmetric series of chromophores (N = 2−4) the lowest energy exciton level is (N − 1)-fold degenerate, supporting absorption and emission polarized in N − 1 orthogonal directions. The oscillator strength scales as N/(N − 1) in each of the allowed directions. Hence, the overall emission decay rate also scales as N/(N − 1), significantly weaker than the N-enhancement found in the linear complexes. The two sets of behaviors converge when N = 2, as expected since the dimer is a member of both series. In all linear and symmetric complexes the 0−0 peak in the absorption spectrum red shifts with increasing $|J_0|$ and the 0−0/1−0 oscillator strength ratio, R_{abs}, initially increases linearly with $|J_0|$. However, in the symmetric complexes these increases are independent of the number of PDI chromophores, N, and the spectral shifts and ratios are markedly smaller than in their linear counterparts (see Figure 3-8). In the linear complexes the excitonic red-shift and R_{abs} depend on both J_0 and N.

The opposing N-dependent trends observed in the absorption spectra of the symmetric vs linear series of PDI chromophores measured by Langhals et al.[12-15] and summarized in Figure 3-5 can be understood as follows: (1) In the symmetric series the coupling, J_0 (with $J_0 > 0$) diminishes with N, as confirmed through TDDFT calculations, but the excitonic (red) shift contains no topological N dependence. This is easily

appreciated in the free-exciton regime where the excitonic shift for all optically allowed excitons is given simply by $-J_0$ for N = 2−4 (see Figure 3-2); (2) by contrast, in the linear series, the nearest- neighbor coupling J_0 remains constant, but the excitonic shift contains a topological N dependence of the form contained in eq 3-6, see also Figure 3-3.Hence, the observed increase in the 0−0 peak frequency along with and the diminished value of R_{abs} in going from the dimer to the cyclic trimer are due to a decrease in J_0 (see Figure 3-4a), whereas the opposite behavior observed in going from dimer to linear trimer is due to the influence of the topological factor, for example, in the free-exciton limit the energy of the k = 1 exciton changes from $e_{0-0} - |J_0|$ for N = 2 to $(e_{0-0} - \sqrt{2}|J_0|)$ for N = 3. (The red-shift of the 0−0 peak in Langhals' tetrahedral complex breaks the trend and is actually slightly red-shifted compared with the cyclic trimer. This arises because the complex is composed of PDI-phenyl chromophores, with the extra phenyl unit per chromophore leading to an additional red-shift, see Figure 3-5.)

A very recent single-molecule study of linear and cyclic PDI trimmers[25] showed that in roughly 20% of the cyclic trimers studied, the emission spectra of the trimer and dimer, where the latter is formed by photobleaching a single PDI unit within the trimer, are spectrally aligned (no relative shift), while a substantial blue shift occurs between the dimer and the monomer formed by photobleaching two PDI units. Such behavior is consistent with the energy level structure of Figure 3-2a but with a constant value of J_0, since the dimer formed upon photo- bleaching the trimer is necessarily bent with the same inter-PDI coupling as exists in the trimer. In Ref. 25 there are also molecules in which a blue-shift is observed in the emission spectrum upon photobleaching the trimer to create the dimer. Such cases may involve distorted trimers, where an angle between

two of the three PDI units is contracted below 120° due to disorder-induced environmental factors. Almost half of the linear trimers in Ref. showed a blue shift after both photobleaching events, as is consistent with the energy scheme in Figure 3-2b.

We have shown previously that in linear J-aggregates with periodic boundary conditions the ratio of 0−0 and 0−1 line strengths in the PL spectrum, $I_{PL}^{0-0}/I_{PL}^{0-1}$, is equal to N/λ^2 whenever the exciton coherence covers all N chromophores, which is favored by low temperature and minimal disorder.[45] The N scaling was confirmed in the emission spectra of the photobleached linear trimers in Ref. 25. We have shown numerically that the PL ratio in symmetric complexes is, to an excellent approximation, given by $N/[(N-1)\lambda^2]$, thereby leading to a factor of 2 reduction in the PL ratio of the cyclic trimer compared to the linear trimer. (In fact, the reduction is slightly less than two due to end effects present in the linear trimer.) In Ref. 25 the maximum observed PL ratio in the linear trimers is ∼4, compared to 2.7 in the cyclic trimers, in rough agreement with our predictions. A better agreement should be achieved by averaging over a Boltzmann distribution of emitting excitons as is necessary for T > 0 K.

Our analysis of spectra of Langhals et al.[12−15] also confirms an important correlation between the exciton red-shift of the 0−0 peak and the 0−0/1−0 ratio of oscillator strengths, R_{abs}, best demonstrated in Figure 3-5. Both quantities can be used to deduce the excitonic coupling, but R_{abs} is more reliable since there are additional sources to spectral shifts (i.e., the gas-to-crystal shift) which complicate the spectral-shift analysis. The spectral shift/R_{abs} correlation is evident in the perturbative expressions for R_{abs} in eqs 3-21 and 3-24, where R_{abs} is an increasing function of the magnitude of the (free-) exciton shift, for example R_{abs} increases with J_0 in eq 3-21. For the symmetric

complexes, where the red-shift, $-J_0$, is independent of N, this suggests that in the perturbative regime, the absorption spectral line shapes for all symmetric complexes are identical, given a constant value of J_0 (see Figure 3-8). This is in fact the case, as we have confirmed numerically. This behavior is in stark contrast to the case of linear complexes where a strong N dependence arises from$\varepsilon_{k=1}^{N}$. Increasing J_0 in either series leads to a breakdown of the ratio formula as the two-particle contributions become important. In the symmetric complexes (with J_0 held constant), two-particle states cause a differentiation of the absorption line shapes for different N; the 0−0/1−0 ratios diminish with increasing N, exactly opposite to what is found in linear complexes. This behavior is shown in Figure 3-7, further demonstrating that symmetric complexes are unusual photophysical entities which are quite different from the conventional J- (or H-) aggregates.

It is interesting to compare linear vs star-shaped chromophores as light harvesters in solar cell applications. For an isotropic distribution of a given concentration of either chromophore type which is superior? By the oscillator sum rule, the integrated molar absorptivity is the same for a given N, but the distribution of oscillator strength is very different in the two chromophore types. In the linear series only the x-component (long-molecular axis) is optically allowed, whereas in symmetric molecules, oscillator strength is distributed over N − 1 orthogonal polarizations. Hence, in an isotropic distribution of either chromophore, the absorptivity along any particular direction is the same. The situation is entirely different in the crystal phase. Due to their geometry, linear chromophores are more prone to crystallization making absorption a strong function of the angle between the electric field vector and the crystal axes. Star-shaped molecules often resist crystallization, forming largely amorphous films. Thus, such films would not

require solar tracking, in contrast to crystalline films, a point originally emphasized by Langhals.[12] Moreover, the significantly reduced radiative decay rates in the nonlinear complexes inhibit radiative loss. Hence, as solar harvesters, star-shaped molecules have significant advantages over their linear counterparts.

The accurate reproduction of the measured absorption spectral line shapes for the linear and symmetric complexes studied herein is strong validation for our computational method for evaluating interchromophore interactions as well as the application of the Holstein Hamiltonian for including the effects of the vibronic coupling. We have achieved a level of accuracy (with no adjustable parameters) of several percent in systems in which interchromophore interactions are dominated by through-space Coulombic interactions. For the PDI complexes studied here, the minimal cofacial overlap inhibits the involvement of charge transfer states (citation 46) which are not accounted for in our analysis. Although in sandwich PDI complexes,[17, 21, 41, 47] our analysis remains qualitatively correct, for example, it predicts a 0−0/1−0 ratio smaller than what is found in the monomer absorption spectrum, as expected for H-aggregates; it generally cannot account for the excimer-like PL line shapes[21, 48] which contrast the well-structured vibronic PL line shapes found in the complexes studied here.[15, 25] In future studies we will consider how vibronic coupling impacts energy and charge migration in PDI complexes.[11, 19, 22-24] It may also prove rewarding to investigate vibronic coupling in more elaborate architectures, such as dendrimers.

We have shown that our model, which utilizes the Holstein Hamiltonian and one- and two-particle vibronic states, once coupling have been calculated, can accurately reproduce the eigenstates and spectra of a diverse set of aggregate geometries. With the

accuracy and versatility of assured by these studies, we now move on to more practical applications of the model at hand. In the next chapter we model positively charged hole type polarons in a 2 dimensional poly(3-hexylthiophene) (P3HT) π-stack. P3HT is a conjugated polymeric material used most notable in organic solar cells as the primary absorber of light as well as the electron donating substance. The coherence length conduction of holes the P3HT phases after charge separation is of particular concern for designers or organic photovoltaic devices. As is shown in the next two chapters, charge modulation spectroscopy (CMS) is an effective probe for the coherence lengths of holes in P3HT π-stacks, and CMS spectra as well as coherence functions are reproduced to an unprecedented accuracy in chapter 4.

REFERENCES

1. Kanibolotsky, A. L.; Perepichka, I. F.; Skabara, P. J. Chem. Soc. Rev. 2010, **39**, p. 2695.

2. Oldham, W. J.; Lachicotte, R. J.; Bazan, G. C. J. Am. Chem. Soc. 1998, **120**, p. 2987.

3. Robinson,M. R.;Wang, S.; Bazan, G. C.; Cao, Y. Adv.Mater. 2000, **12**, p. 1701.

4. Roncali, J.; Leriche, P.; Cravino, A. Adv. Mater. 2007, **19**, p. 2045.

5. Mangold, H. S.; Richter, T. V.; Link, S.; Wurfel, U.; Ludwigs, S. J. Phys. Chem. B 2011, **116**, p. 154.

6. Tretiak, S.; Chernyak, V.; Mukamel, S. J. Phys. Chem. B 1998, **102**, 3310.

7. Minami, T.; Tretiak, S.; Chernyak, V.;Mukamel, S. J. Lumin. 2000, **87**−9, p. 115.

8. Badaeva, E.; Harpham, M. R.; Guda, R.; Suzer, O.; Ma, C. Q.; Bauerle, P.; Goodson, T.; Tretiak, S. J. Phys. Chem. B 2010, **114**, p. 15808.

9. Lee, C. C.; MacKay, J. A.; Frechet, J. M. J.; Szoka, F. C. Nat. Biotechnol. 2005, **23**, p. 1517.

10. Crooks, R.M.; Zhao,M.Q.; Sun, L.; Chechik, V.; Yeung, L. K. Acc. Chem. Res. 2001, **34**, .p 181.

11. Wilson, T.M.; Tauber,M. J.;Wasielewski,M. R. J. Am. Chem. Soc. 2009, **131**, p. 8952.

12. Langhals, H. Helv. Chim. Acta 2005, **88**, p. 1309.

13. Langhals, H.; Jona, W. Angew. Chem., Int. Ed. 1998, **37**, p. 952.

14. Langhals, H.; Gold, J. J. Prakt. Chem./Chem.-Ztg. 1996, **338**, p. 654.

15. Langhals, H.;Wagner, C.; Ismael, R. New J. Chem. 2001, **25**, p. 1047.

16. Kaiser, T. E.; Stepanenko, V.; Wurthner, F. J. Am. Chem. Soc. 2009, **131**, p. 6719−6732.

17. Ghosh, S.; Li, X.-Q.; Stepanenko, V.;Wurthner, F. Chem. Eur. J. 2008, **14**, 11343−11357.

18. Shaller, A. D.; Wang, W.; Gan, H. Y.; Li, A. D. Q. Ang. Chem. Int. Ed. 2008, **47**, p. 7705.

19. Rybtchinski, B.; Sinks, L. E.; Wasielewski, M. R. J. Phys. Chem A 2004, **108**, p. 7497.
20. Veldman, D.; Chopin, S. M. A.; Meskers, S. C. J.; Groeneveld, M. M.; Williams, R. M.; Janssen, R. A. J. J. Phys. Chem A 2008, **112**, p. 5846.
21. Giaimo, J.M.; Lockard, J. V.; Sinks, L. E.; Scott, A. M.;Wilson, T. M.; Wasielewski, M. R. J. Phys. Chem. A 2008, **112**, p. 2322.
22. Schlosser, F.; Sung, J.; Kim, P.; Kim, D.; Wurthner, F. Chem. Sci. 2012, **3**, p. 2778.
23. Montgomery, N. A.; Hedley, G. J.; Ruseckas, A.; Denis, J.-C.; Schumacher, S.; Kanibolotsky, A. L.; Skabara, P. J.; Galbraith, I.; Turnbull, G. A.; Samuel, I. D. W. Phys. Chem. Chem. Phys. 2012, **14**, p. 9176.
24. Metivier, R.; Nolde, F.; Mullen, K.; Basche, T. Phys. Rev. Lett. 2007, **98**, p. 047802.
25. Yoo, H.; Furumaki, S.; Yang, J.; Lee, J.-E.; Chung, H.; Oba, T.; Kobayashi, H.; Rybtchinski, B.; Wilson, T. M.; Wasielewski, M. R.; Vacha, M.; Kim, D. J. Phys. Chem. B 2012, **116**, p. 12878.
26. Kistler, K. A.; Pochas, C. M.; Yamagata, H.; Matsika, S.; Spano, F. C. J. Phys. Chem. B 2011, **116**, p. 77.
27. Langhals,H.; Hofer, A.; Bernhard, S.; Siegel, J. S.;Mayer, P. J. Org. Chem. 2011, **76**, p. 990.
28. Kasha, M. Radiat. Res. 1963, **20**, p. 55.
29. Spano, F. C. Chem. Phys. 2006, **325**, p. 22.
30. Spano, F. C. Acc. Chem. Res. 2010, **43**, p. 429.
31. Clark, J.; Silva, C.; Friend, R.H.; Spano, F. C. Phys. Rev. Lett. 2007, **98**, p. 206406.
32. Spano, F. C. J. Am. Chem. Soc. 2009, **131**, p. 4267.
33. Spano, F. C. J. Chem. Phys. 2002, **116**, p. 5877.
34. Philpott, M. R. J. Chem. Phys. 1971, **55**, p. 2039.
35. Stradomska, A.; Petelenz, P. J. Chem. Phys. 2009, **131**, p. 044507.
36. Dunning, T. H. J. Chem. Phys. 1989, **90**, p. 1007.

37. Wong, C. Y.; Curutchet, C.; Tretiak, S.; Scholes, G. D. J. Chem. Phys. 2009, **130**, p. 081104.

38. Chang, J. C. J. Chem. Phys. 1977, **67**, p. 3901.

39. Patwardhan, S.; Sengupta, S.; Wurthner, F.; Siebbeles, L. D. A.; Grozema, F. J. Phys. Chem. C 2010, **114**, p. 20834.

40. Li, H.; Malinin, S. V.; Tretiak, S.; Chernyak, V. Y. J. Chem. Phys. 2010, **132**, p. 124103.

41. Guthmuller, J.; Zutterman, F.; Champagne, B. J. Chem. Phys. 2009, **131**, p. 154302.

42. Diehl, F. P.; Roos, C.; Jankowiak, H. C.; Berger, R.; Kohn, A.; Diezemann, G.; Basche, T. J. Phys. Chem B 2010, **114**, p. 1638.

43. Pope, M.; Swenberg, C. E. Electronic processes in organic crystals and polymers, 2nd ed.; Oxford University Press: New York, 1999; Vol. **56**.

44. Spano, F. C. J. Chem. Phys. 2005, **122**, p. 234701.

45. Spano, F. C.; Yamagata, H. J. Phys. Chem. B 2011, **115**, p. 5133−5143.

46. Gao, F.; Zhao, Y.; Liang, W. J. Phys. Chem. B 2011, **115**, p. 2699.

47. Zheng, Y.; Long, H.; Schatz, G. C.; Lewis, F. D. Chem. Commun. 2005, p. 4795−4797.

48. Fink, R. F.; Seibt, J.; Engel, V.; Renz, M.; Kaupp, M.; Lochbrunner, S.; Zhao, H. M.; Pfister, J.; Wurthner, F.; Engels, B. J. Am. Chem. Soc. 2008, 130, p. 12858.

CHAPTER 4

NEW INSIGHTS ON THE NATURE OF TWO-DIMENSIONAL POLARONS IN SEMICONDUCTING POLYMERS: INFRARED ABSORPTION IN POLY(3-HEXYLTHIOPHENE)

4-1 Introduction

Charge conduction in semiconducting polymers is of primary concern in the fabrication and optimization of plastic electronic devices such as light-emitting diodes[1, 2] and solar cells.[3-6] In π-conjugated polymers charges are strongly coupled to intramolecular vibrational degrees of freedom resulting in the formation of charged polarons with relaxation energies of approximately 0.1 eV, as revealed though the onset of mid-gap absorption features.[7] Generally, the polaron mobility and photophysical response depend in a complicated way on the electronic coupling within and between polymer chains, the coupling between the electronic and nuclear degrees of freedom, and the presence of disorder.[7-17] In this paper we analyze theoretically the nature of positively charged polarons (holes) in poly(3-hexylthiophene) or P3HT, the polymer of choice in photovoltaic applications, through a careful analysis of the mid- to near-infrared absorption spectrum. Our nonadiabatic approach treats the electronic coupling, electronic-vibrational (EV) coupling, and disorder on equal footing.

In the conventional adiabatic description, the formation of a polaron in a conjugated polymer chain is accompanied by the creation of two mid-gap states, one slightly above the valence band and one slightly below the conduction band, leading to additional mid- and near-infrared peaks (labelled P_1 and P_2) in the absorption spectrum.[7] In P3HT such peaks have been detected using transient absorption spectroscopy[18, 19] and charge modulation spectroscopy.[12, 20, 21] In the semicrystalline phase, P3HT exhibits

lamellar packing, in which the thiophene backbones form π-stacks separated by alkyl-rich layers containing the hexyl side-chains.[22, 23] As the π-stacking distance is only 3.8 Å, interchain interactions become important in exciton and polaron transport – indeed there is convincing evidence of two-dimensional polaron delocalization (along the polymer backbone and along the π-stacking axis) from transient pump-probe spectroscopy[18, 19] and charge modulation spectroscopy.[12, 20, 21] Interchain interactions result in additional peaks in the polaron absorption spectrum; a low-energy, infrared peak (referred to as DP_1) due to a direct charge transfer transition between chains, and a higher energy, near-infrared partner (DP_2). Both peaks arise from splitting of the main intrachain polaronic bands, P_1 andP_2, due to interchain interactions.[18, 21]

Several theories have been advanced to account for the effect of interchain coupling on polarons in conjugated polymers.[8-10, 12-15] Initial concern focused mainly on the stability of polarons in the presence of interchain coupling. The general conclusion was that disorder is needed to localize the wave function to the point that self-trapping along the chain is possible.[9, 10] The infrared spectral signatures of interchain charge-transfer were investigated by Beljonne *et al.*[8] and Chang *et al.*[12] Using quantum chemical techniques and employing the adiabatic approximation in treating the vibronic coupling involving the main aromatic-quinoidal stretching mode, Beljonne *et al.* calculated the polaron absorption spectrum of a cationic dimer, revealing the presence of a low energy (infrared) peak polarized along the internuclear axis with an absorption cross-section proportional to the peak absorption energy. A nonadiabatic analysis based on charge transfer between a single donor chain and a single acceptor chain was later employed by Chang *et al.*[12] Their approach mirrors that of Piepho *et al.*[24-26]. used to

investigate mixedvalence Creutz-Taube complexes.[27] Chang *et al.* correlated the higher mobilities found in the higher MW P3HT films with stronger interchain interactions and smaller polaron relaxation energies. Although the theories of Refs. 8 and 12 shed important light on the more general features of polaron absorption, they were unable to capture the vibronic features present in the measured spectra. Moreover, neither approach considered disorder, which, as we show below, has a major impact on the polaron photophysics.

In the present work we revisit the theory of polaron absorption in P3HT π-stacks using the Holstein molecular crystal Hamiltonian,[28] modified to include spatially correlated diagonal and off-diagaonal disorder, in an overall effort to better appreciate the impact of interchain interactions on polaron photophysics.We treat a "square" lattice consisting of N polymer chains with N thiophene rings per polymer. Our approach is nonadiabatic at the outset, as the Holstein Hamiltonian treats both the nuclear kinetic and potential energy terms fully quantum mechanically. We employ a multi-particle basis set[29-31] truncated at the two-particle level which includes local and nonlocal nuclear distortions surrounding the hole. Such distortions occur mainly along the aromatic-quinoidal symmetric stretching coordinate, with an associated energy of approximately 0.17 eV. The basis set is analogous to that used to successfully account for the photophysics of excitons in P3HT π-stacks.[32-36] The lattice model is similar to that used in Refs. 35 and 36, except that here we focus on a single oxidized chain (hole) and include only the coupling between adjacent unit-cell (thiophene ring) HOMO's along and across chains. By omitting the LUMO's within each unit cell we are limited to infrared absorption – i.e., to the spectral region surrounding the P_1 and DP_1 peaks. One of the big

advantages of the current approach is that it is not restricted, as is Hush theory[37] and the theories of Piepho *et al.*[24-26] to just two coupled chromophores. In what follows we treat up to 25 coupled chromophores in a 5 × 5 lattice. Spatially correlated diagonal disorder due to Gaussian distributed site polarization energies is readily accounted for as well as off-diagonal disorder due to a Gaussian distribution of nearest-neighbor interchain distances. The latter, referred to as paracrystallinity,[11, 13, 14] plays a major role in limiting hole mobility and has been shown to depend strongly on the polymer molecular weight.[11] Our theory quantitatively reproduces the infrared line shapes reported in Refs. 18 and 12, including the peak positions and relative intensities of the vibronic features, and shows how interchain (intrachain) disorder *selectively* attenuates the component of the absorption spectrum polarized along the stacking axis (polymer backbone axis), allowing one to gain greater insight into the two-dimensional nature of charges in polymer films.

4-2 Model

In this section, we introduce the Hamiltonian for a positively charged polaron ("hole") in P3HT, which is modeled as a two-dimensional square aggregate consisting of N chains, each with N thiophene units as depicted in Fig. 4-1 An individual P3HT chain is treated as a linear array of coupled thiophene chromophores, where only the local HOMO of each thiophene unit is retained. A hole on a given thiophene ring therefore corresponds to a missing electron in its HOMO. The local HOMO's of adjacent rings are coupled to each other through the hole transfer integral, t_{intra}. In a π-stack of such chains there is also wave function overlap between the neighboring thiophene HOMOs on

adjacent chains. The resulting interchain electronic coupling is represented by the transfer integral, *tinter*. Such a course-grained approach on a P3HT lattice has previously been used to study neutral excitons,[35, 36] where the thiophene LUMO was also retained.

Figure 4-1

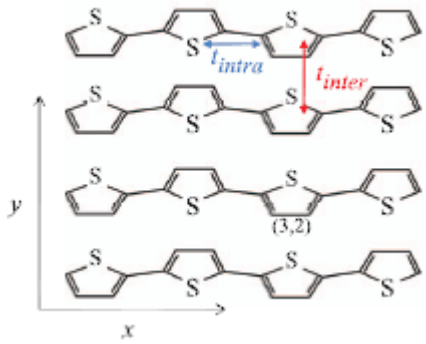

Figure. 4-1. 4 × 4 π-stack showing the intra- and interchain interactions. We assume a square lattice of thiophene rings with a nearest neighbor distance (d) of 0.4 nm in each direction.

In order to account for the nuclear relaxation accompanying the formation of a hole on a particular thiophene unit, we consider local vibronic coupling involving the aromatic/quinoidal stretching mode at approximately 0.17 eV. We employ a site based Holstein Hamiltonian, where the nuclear potentials for molecular vibrations in the ground state, S_0 (doubly filled HOMO) and cationic state, S_+ of a given thiophene chromophore are shifted harmonic wells of identical curvature. In the vector subspace containing a single hole within a $N \times N$ square π-stack, the Hamiltonian reads:

$$
\begin{aligned}
H_0 = & \sum_{m=1}^{N-1}\sum_{n=1}^{N} t_{intra}\{|m+1,n\rangle\langle m,n| + h.c.\} \\
& + \sum_{m=1}^{N}\sum_{n=1}^{N-1} t_{inter}\{|m,n+1\rangle\langle m,n| + h.c.\} \\
& + \hbar\omega_{vib}\sum_{m=1}^{N}\sum_{n=1}^{N} b_{m,n}^{\dagger} b_{m,n} + \hbar\omega_{vib}\lambda\sum_{m=1}^{N}\sum_{n=1}^{N}(b_{m,n}^{\dagger} \\
& + b_{m,n})|m,n\rangle\langle m,n| + \hbar\omega_{vib}\lambda^2,
\end{aligned}
\tag{4-1}
$$

where *h.c.* means hermittian conjugate. The first two terms represent the electronic coupling along and across chains with $|m,n\rangle$ designating the pure electronic state in which the hole resides on the mth thiophene unit of the nth chain while all other units have doubly filled HOMO levels. The last several terms account for local vibronic coupling involving the symmetric aromatic/quinoidal stretching vibration with energy, $\omega_{vib} \approx 0.17$ eV. The operators $b_{m,n}^{\dagger}$ and $b_{m,n}$, respectively, create and annihilate vibrational quanta on the thiophene unit at position (m,n) within the ground (S_0) potential well. The Huang-Rhys (HR) factor λ^2 represents the geometric relaxation energy experienced by a single monomer subsequent to ionization (in units of ω_{vib}), which is nonzero whenever the ground and cationic potential wells are shifted relative to each other. In P3HT λ^2 is approximately unity.[36] Finally, the Hamiltonian omits a constant term representing the zero-point vibrational energy as well as the on-site polaron energy. As we are interested only in transitions between eigenstates such terms are unimportant. Terms representing diagonal and off diagonal disorder will be introduced in Sec. 4-4.

Under the two-particle approximation, the basis set used to represent H in Eq. 4-1 is truncated to include just the one- and two-particle states, analogous to the one and two

particle states used in treating neutral excitons.[32, 33] Hence, in a single-particle state, denoted as $|m, n, \tilde{v}\rangle$ a hole resides on the mth thiophene monomer of the nth chain with $\tilde{v}$ vibrational quanta in its *shifted* (S_+) potential well. The remaining $N^2 - 1$ monomers are in their vibrationless ground states (filled HOMO with no vibrations in the S_0 well). In a two particle state, denoted $|m, n, \tilde{v}\ ; m', n', v'\rangle$, monomer (m,n) is ionized with $\tilde{v}$ vibrational quanta in S_+, while monomer (m', n') is electronically neutral, with $v' > 0$ vibrational quanta in the unshifted S_0 potential. The remaining $N^2 - 2$ monomers are in their vibrationless ground states. Three- and higher particle states with three or more thiophene ring excitations (electronic plus vibrational) can also be included, but their impact is negligible on the calculated infrared spectra for the vibronic coupling parameters used here.

When interchain and intrachain electronic coupling are neglected the multi-particle states are eigenstates of H in Eq. 4-1. Electronic coupling induces mixing amongst the one and two-particle states. In the general case, the αth eigenstate of H in Eq. 4-1 can be written as

$$|\Psi_\alpha\rangle = \sum_{m,n=1} \sum_{\tilde{v}=0,1,\ldots} c^{\alpha}_{m,n,\tilde{v}} |m, n, \tilde{v}\rangle + \sum_{m,n,\tilde{v}} \sum_{m',n',v'} c^{\alpha}_{m,n,\tilde{v};m',n',v'} |m, n, \tilde{v}; m', n', v'\rangle. \tag{4-2}$$

The one- and two-particle expansion coefficients can be readily obtained numerically; however, more insight can be gained from analytical results obtained in certain limits. When the electronic coupling is weak compared to the nuclear relaxation, $\lambda^2 \hbar\omega_{vib}$ (≈ 0.2 eV),

$$2|t_{intra}| + 2|t_{inter}| < \lambda^2 \hbar\omega_{vib},$$

(4-3)

the polaron eigentates are divided into vibronic bands, as depicted in Fig. 4-2(a). The bands are labeled with the quantum number $\tilde{v}$ (= 0, 1, . . .) which represents the number of vibrational quanta in the single particle component of the zeroth order eigenstate. In the *lowest* energy band the zeroth order eigenstates are entirely one-particle state constructs with $\tilde{v} = 0$, given by

$$\begin{aligned} &|k_x, k_y; \tilde{v} = 0\rangle \\ &= \frac{2}{N+1} \sum_{m,n} \sin\left(\frac{m\pi k_x}{N+1}\right) \sin\left(\frac{n\pi k_y}{N+1}\right) \\ &\times |m, n; \tilde{v} = 0\rangle \\ &k_x, k_y = 1, 2, 3, \ldots, N. \end{aligned}$$

(4-4)

The corresponding first-order energies are

$$\begin{aligned} E_{k_x,k_y;\tilde{v}=0} = \Bigg\{ & 2t_{intra} \cos\left(\frac{\pi k_x}{N+1}\right) \\ & + 2t_{inter} \cos\left(\frac{\pi k_y}{N+1}\right) \Bigg\} e^{-\lambda^2}. \end{aligned}$$

(4-5)

Taking t_{intra} and t_{inter} to be negative gives the polaron ground state as

$$|G\rangle \equiv |k_x = 1, k_y = 1, \tilde{v} = 0\rangle,$$

(4-6)

with energy, $E_G = E_{1,1,0}$. In higher vibrational bands with $\tilde{v} \geq 1$ one- and two-particle states are degenerate when the excitonic coupling tends to zero – for example, in the $\tilde{v}$ = 1 band, the one-particle states |*m, n,* $\tilde{v}$ = 1> are degenerate with the two-particle states |*m,*

n, $\tilde{\nu}$ = 0; *m*', *n*', *v*' = 1>. Hence, the zero order states in the bands with ˜ $v \geq 1$ are generally mixtures of one- and two-particle states.[32, 33]

Increasing the electronic coupling by a factor of ten in both dimensions compared with the values used in Fig. 2-4(a) results in the energy level diagram in Fig. 2-4(b). The intrachain and interchain hole transfer integrals are now comparable to the nuclear relaxation energy (≈0.2 eV) along the aromatic-quinoidal coordinate, defining the intermediate coupling regime. The coupling, *tinter* = −0.15 eV, is a typical value used in treating interchain interactions in pheneylene and thiophene based polymers.[13, 38] The intrachain coupling, t_{intra} = −0.3 eV,[39] is slightly below the range, 0.4−1 eV, typically employed in treating conjugated polymers[13, 38, 40] but agrees well with the value deduced from a recent line shape analysis of steady-state exciton absorption and PL in P3HT stacks.[36] Fig. 2-4(b) shows that in the intermediate coupling regime, the vibronic band structure is lost, and the ground state undergoes a large red shift relative to the weak coupling regime. The significant difference between the weak and intermediate coupling limits is immediately apparent in the calculated absorption spectra, as shown in Sec. 3-4

Figure 4-2.

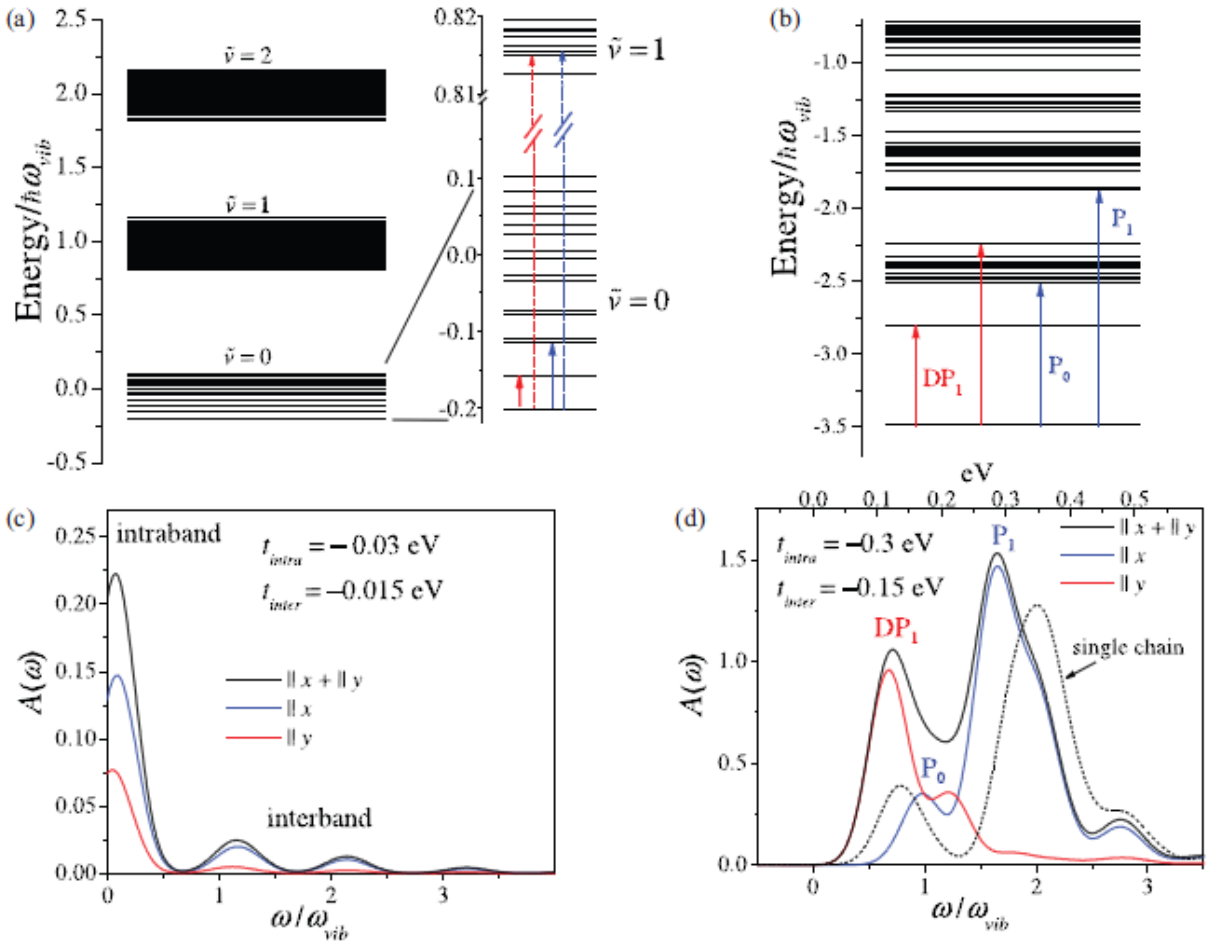

Fig. 4-2. (a) Hole energy levels corresponding to a 4 × 4 π-stack in the weak exciton coupling limit, with $t_{intra} = -0.03$ eV, $t_{inter} = -0.015$ eV, $\omega_{vib} = 0.174$ eV/$\hbar$, and $\lambda^2 = 1$. Solid (dotted) arrows show intraband (interband) transitions. (b) Hole energy levels in the intermediate coupling regime with the electronic couplings increased tenfold. (c) and (d) show the absorption spectra corresponding to cases (a) and (b), respectively, using a homogeneous line width, $\Gamma = 0.03$ eV.

4-3. Polaron Absorption In Disorder-Free π-Stacks

In what follows we evaluate the infrared absorption spectrum for $N \times N$ π-stacks using the Holstein Hamiltonian in Eq. 4-1. Like the PKS theory[26] used to treat just two

coupled (donor and acceptor) chromophores the approach is fully nonadiabatic. In fact, for a dimer (1 × 2 aggregate) our calculated spectrum agrees exactly with that evaluated using PKS theory.

The *j*-polarized (*j* = *x,y*) absorption spectrum for a positively charged polaron in a square lattice is evaluated using the expression

$$A_j(\omega) = (e^2 d^2 \hbar\omega_{vib})^{-1} \sum_{\alpha} f_{\alpha}^{(j)} W_{LS}(\omega - \omega_{\alpha G}).$$

(4-7)

Equation 4-6 contains the *j*-polarized oscillator strength corresponding to the $|G\rangle \rightarrow |\Psi_\alpha\rangle$ transition,

$$f_{\alpha}^{(j)} = \hbar\omega_{\alpha G} |\langle G|\hat{\mu}_j|\Psi_\alpha\rangle|^2,$$

(4-8)

where $\hbar\omega_{\alpha G} \equiv E_\alpha - E_G$ is the transition energy and $\hat{\mu}$ is the vector transition dipole moment operator, defined as

$$\hat{\boldsymbol{\mu}} = e \sum_{m,n=1}^{N} \boldsymbol{r}_{m,n} |m,n\rangle\langle m,n|.$$

(4-9)

Here, $\boldsymbol{r}_{m,n} = md\hat{x} + nd\hat{y}$ is the position vector locating the (*m,n*) thiophene unit. $\hat{x}$ and $\hat{y}$ are unit vectors along the *x* and *y*-axes, respectively, and *d* is the nearest neighbor distance between chains, which is also (approximately) equal to the distance between neighboring thiophene rings within a chain ($d \approx 0.4$ nm). Finally, $W_{LS}(\omega)$ is the homogeneous line shape function, taken to be a normalized Gaussian, $W_{LS}(\omega) \equiv (2\pi$

$\Gamma^2)^{-1/2} exp(-\omega^2/2\Gamma^2)$ with line width, Γ. $A(\omega)$ is normalized so that its spectral area is dimensionless.

Fig. 4-2(a) depicts the two main transitions in the weak coupling limit, one polarized along the polymer backbone (x) and one polarized along the stacking axis (y), as indicated by the solid blue and solid red arrows, respectively. Both are intraband transitions as they occur within the lowest vibronic band with $\tilde{\nu} = 0$.[54] The strongest transitions occur between the ground state, $|G\rangle = |k_x = 1,\ k_y = 1, \tilde{\nu} = 0\rangle$, and the polarons with $k_x = 2$, $k_y = 1$ (x-polarized) and $k_x = 1$, $k_y = 2$ (y-polarized) *within* the lowest energy band ($\tilde{\nu} = 0$). Using Eq. 4-4 the corresponding transition energies relevant to the weak coupling regime are

$$E_{k_x=2,k_y=1;\tilde{\nu}=0} - E_G = 4|t_{intra}| \sin\left(\frac{\pi}{2(N+1)}\right) \times \sin\left(\frac{3\pi}{2(N+1)}\right) e^{-\lambda^2} \quad x\text{-}polarized \tag{4-10(a)}$$

and

$$E_{k_x=1,k_y=2;\tilde{\nu}=0} - E_G = 4|t_{inter}| \sin\left(\frac{\pi}{2(N+1)}\right) \times \sin\left(\frac{3\pi}{2(N+1)}\right) e^{-\lambda^2} \quad y\text{-}polarized. \tag{4-10(b)}$$

Equations 4-9(a) and 4-9(b) show that the x-polarized (y-polarized) transition energies scale directly with the magnitude of the intrachain (interchain) coupling. In addition, the transition energies redshift as the π-stack increases in size,[41] scaling as $(N+1)^{-2}$ for sufficiently large N ($N \gtrsim 4$). The corresponding oscillator strengths are given by

$$f^{(x)}_{k_x=2,k_y=1;\tilde{v}=0} \approx |t_{intra}|e^2d^2e^{-\lambda^2},$$

4-11(a)

$$f^{(y)}_{k_x=1,k_y=2;\tilde{v}=0} \approx |t_{inter}|e^2d^2e^{-\lambda^2}.$$

4-11(b)

Like the transition energies, the oscillator strengths are also directly proportional to $|t_{intra}|$ and $|t_{inter}|$. The linear dependence of the oscillator strength on the inter (or intra-) chain splitting has also been shown by Beljonne *et al.* in treating a PPV dimer.[8] The scaling of the intraband transition energies *and* oscillator strengths with the excitonic couplings is apparent in the absorption spectrum shown in Fig. 4-2(c), where the dominant low-energy peak in the *x*- and *y*-polarized spectra is due to the intraband transitions. The *x*-polarized peak is twice as intense and has twice the transition energy as the *y*-polarized peak, consistent with our taking $t_{intra} = 2t_{inter}$.

As shown in Fig. 4-2(a) there is also a series of *interband* transitions for both polarizations occurring at approximately $\tilde{v}\hbar\omega_{vib}$ ($\tilde{v}$ = 1, 2, . . .) above the intraband transition – only transitions to the $\tilde{v}$ = 1 band are shown in the level diagram (dotted arrows). The interband transitions are far weaker than the intraband transitions in the weak electronic coupling limit and become activated only when the polaron wave functions are corrected to first order in $|t_{intra}|/\hbar\omega_{vib}$ and $|t_{inter}|/\hbar\omega_{vib}$. First order corrections are due to interband coupling between the zeroth order states with $\tilde{v}$ = 0 in Eq. 4-3 with zero-order states having the same k_x and k_y values but in higher-energy bands with $\tilde{v} > 0$. This is analogous to the case of interband coupling in neutral excitons discussed in Ref.

(citation 33) and involves both one- *and* two-particle contributions. Using the first order wave functions to evaluate the oscillator strengths gives

$$f^{(x)}_{k_x=2,k_y=1;\tilde{\nu}=1} \approx 2\frac{t^2_{intra}\lambda^2 e^{-2\lambda^2}}{\hbar\omega_{vib}} e^2 d^2, \qquad \text{4-12(a)}$$

$$f^{(y)}_{k_x=1,k_y=2;\tilde{\nu}=1} \approx 2\frac{t^2_{inter}\lambda^2 e^{-2\lambda^2}}{\hbar\omega_{vib}} e^2 d^2. \qquad \text{4-12(b)}$$

Unlike the intraband transitions, the *x* and *y*-polarized interband transitions scale quadratically with the coupling strength. This property is also evident in the absorption spectrum in Fig. 4-2(c), where the second peak in the vibronic progression, arising from the ($\tilde{\nu}$ = 1) interband transitions, is four times more intense in the *x*-direction compared to the *y*-direction, as expected since $t_{intra} = 2t_{inter}$.[54] There it is shown that the adiabatic approximation is wholly inappropriate in treating exciton-vibrational coupling involving the high-frequency aromatic-quinoidal mode. This is quite important, as most theories which treat self-trapping of polarons in conjugated polymers employ the adiabatic approximation.[9, 10, 42, 43]

Fig. 4-2(d) shows the polaron absorption spectrum in the intermediate coupling regime relevant for conjugated polymers, obtained by increasing both *tintra* and *tinter* by a factor of ten over the values used in Fig. 2-4(c). The change to the spectral line shape is quite dramatic. As observed in Fig. 4-2(b), the vibronic bands are no longer well-defined so that the transitions cannot be unambiguously classified as intraband or interband. For the interchain (*y*-polarized) transitions the first peak remains dominant and is about a factor of ten larger than the corresponding peak in the weak coupling regime. In marked

contrast, the intrachain (*x*-polarized) transition undergoes a dramatic reversal of peak intensities – the dominant peak is now the second peak, opening up a large energy gap between the main interchain and intrachain transitions. The dominant *y*-polarized peak is due to interchain charge transfer and is referred to as DP1 in Ref. 18. The dominant *x*-polarized peak is intrachain in nature and is identified with P_1 in[18] (also referred to as C_1[21]). The P1 assignment is further justified by the dotted spectrum in Fig. 4-2(d), which represents the single polymer chain spectrum obtained by setting the interchain coupling to zero. The P1 peak remains dominant but is shifted to higher energy. The decrease in the energy of P1 caused by interchain coupling has also been reported by Beljonne *et al*[8]. who interpreted the spectral shift as a decrease in the polaron relaxation energy due to enhanced interchain delocalization.

The weak first peak in the intrachain absorption spectrum, labeled P_0 in Fig. 4-2(d), has not, to our knowledge, been reported before. P_0 is intrinsic to single polymer chains, as it remains a prominent feature in the single-chain spectrum in Fig. 4-2(d), but it cannot be accounted for in the simplified molecular orbital picture commonly used to describe polarons under the adiabatic approximation.[7, 8] Further investigation shows that P_0 arises from an excited state which is predominantly two-particle in character, with a two-particle admixture of approximately 60%. As shown in the figure, P_0 shifts to the blue when interchain coupling is activated, in contrast to the redshift experienced by P_1. Interestingly, in a single chain P_0 exists in the vicinity of the spectrum where the narrow infrared-active vibrational (IRAV) modes appear in unaggregated P3HT derivatives,[19] peaking at an energy slightly less than a vibrational quantum.

We have also directly tested the impact of increasing nuclear relaxation energy on the π–stack absorption spectrum. Fig. 4-3 shows the interchain and intrachain spectra for several HR factors. Increasing the relaxation energy, $\lambda^2\hbar\omega_{vib}$, leads to a blue shift of the main P_1 band in the intrachain spectrum, consistent with the MO picture of polymer polarons, where the half-filled, highest energy valence MO is pushed higher into the band gap with increasing relaxation energy.[7, 8] In contrast, the low-energy feature, P_0, redshifts with increasing relaxation energy. A similar trend holds for DP_1 which also redshifts with increasing relaxation energy, consistent with its intraband heritage (see Eq. 4-9(b)), while the higher-energy but lower-intensity *y*-polarized peak blueshifts.

Figure 4-3

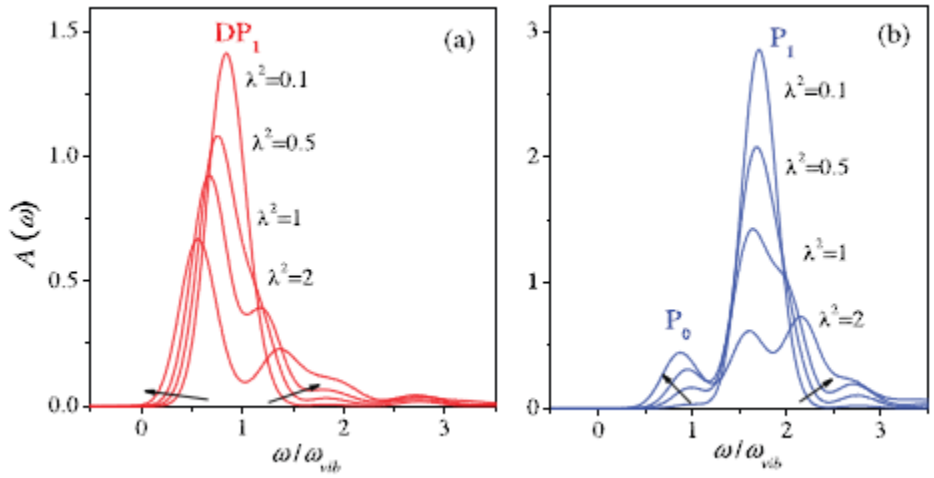

Fig. 4-3. Calculated y-polarized (a) and x-polarized (b) absorption spectra for a 4 × 4 π-stack in the intermediate coupling regime with t_{intra} = −0.3 eV, t_{inter} =−0.15 eV, ω_{vib} = 0.174 eV/$\hbar$, and for several HR parameters, λ^2. The homogeneous line width is Γ = 0.03 eV.

We next investigated how the spectral components change when the aggregate size is increased to 5 × 5, the largest size we can handle numerically. Figs. 4-4(a) and 4-4(b) show infrared spectra for 4 × 4 and 5 × 5 π-stacks, respectively. Two sets of spectra

are shown corresponding to $t_{intra} = -0.3$ eV and $t_{intra} = -0.45$ eV (t_{inter} is unchanged). The larger value for $|t_{intra}|$ was derived using DFT in Ref. 40 and employed in Ref. 13 to model the density of states in P3HT. As expected, increasing $|t_{intra}|$ affects primarily the P_1 band, leading to a significant blue shift and large intensity increase.

Figure 4-4

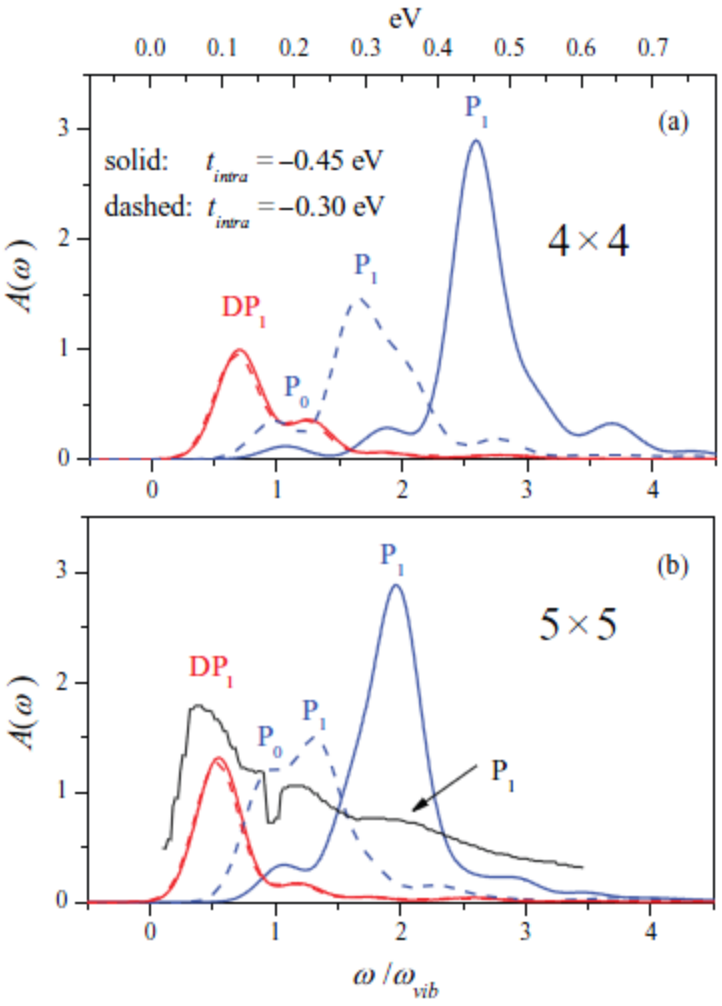

Fig. 4-4. Calculated polarized polaron absorption spectra using $t_{intra} = -0.45$ eV (solid) and $t_{intra} = -0.30$ eV (dashed) for a 4 × 4 π-stack in (a) and a 5 × 5 π-stack in (b). In all cases $t_{inter} = -0.15$ eV, $\omega_{vib} = 0.175$ eV/$\hbar$, $\lambda^2 = 1$ and the *homogeneous* line width is $\Gamma = 0.03$ eV. The black dotted curve in (b) is the (unpolarized) experimental transient induced absorption spectrum for (>99%) regioregular P3HT films cast from xylene from Ref. 18.

For both sets of spectra, increasing size leads to expected spectral redshifts in both the *x*- and *y*-polarized components. There is also a large enhancement of the first intrachain vibronic peak, P_0.[54] As long as disorder is neglected, as in Fig. 4-4, we anticipate the x- and y-polarized spectra to continue to redshift with increasing *N*. Based on a detailed analysis of disorder given in Secs. 4-4 and 4-5, we estimate the coherence length to be about 5 thiophene units in P3HT π-stacks. Hence, the spectrum for a 5×5 π-stack is already near convergence.

Fig. 4-4(b) also shows the measured induced-absorption spectrum of P3HT films spin cast from xylene reported in Ref. 18, but without the sharp IRAVs, as the latter are omitted in the present theory. Although the peak positions of DP_1 and P_1 are roughly reproduced by the $t_{intra} = -0.45$ eV spectra, the relative intensity ratios are approximately inverted; the measured (calculated) value of I_{DP1}/I_{P1} is roughly $2^{(1/2)}$. In order to make more quantitative comparisons with experiment one needs to consider the localizing influence of disorder.

4-4 Polaron Absorption In Disordered π-Stacks

In this section we consider the effects of diagonal and off-diagonal disorder on the hole absorption spectrum. The former includes random changes in the site energy of the hole while the latter includes changes in the hole transfer integrals. Both forms of disorder are due to an inhomogeneous polarizing environment surrounding the hole due to disturbances in intrachain and interchain order.[44, 45] Inhomogeneity can be manifest as variations in the nearest-neighbor π-stacking distance, as occurs in paracrystalline films, accompanied by variations in the intramolecular torsional angles within the

polymer.[11, 13, 14] Inhomogeneity may also arise from spatially varying local electric fields arising from a distribution of holes. In what follows, disorder is represented as random changes in the hole energy, $\varepsilon_{m,n}$, when the hole resides on monomer (m,n), as well as variations of the *interchain* transfer integrals, t_n, between chain n and chain $n+1$. The associated Hamiltonian for a disordered $N \times N$ π-stack is given by

$$H = H_0 + H_{diag} + H_{off\ diag},$$

4-13

where H_0 was introduced in Eq. 4-1. The diagonal and off-diagonal terms are given by

$$H_{diag} = \sum_{m=1}^{N} \sum_{n=1}^{N} \Delta\varepsilon_{m,n} |m,n\rangle\langle m,n|,$$

(4-14)

and

$$H_{off\ diag} = \sum_{m=1}^{N} \sum_{n=1}^{N-1} \Delta t_n \{|m,n+1\rangle\langle m,n| + |m,n\rangle\langle m,n+1|\}.$$

(4-15)

Off-diagonal disorder within a polymer chain can also be included, as induced by torsional defects, for example. t_{intra} is expected to scale as the cosine of the torsional angle; the impact of torsional defects is therefore weak but for very large angular deviations from planarity[46] which occur only infrequently in a π-stack of planarized polymer segments. We expect the relative changes in t_{inter} – by as much as 30% when the interchain separation changes by only 5%[47] – to be much larger than changes in t_{intra}

due to torsional defects. The hypersensitivity of t_{inter} to interchain separation arises from the strong dependence of t_{inter} on the wave function overlap.

A. Diagonal disorder

We begin by focusing on the impact of just diagonal disorder on the infrared spectrum. Each of the N^2 energy variations, $\varepsilon_{m,n}$, within a $N \times N$ π–stack was selected from a Gaussian distribution with standard deviation σ: $P(\Delta\varepsilon_{m,n}) = (2\pi\sigma^2)^{-1/2}$ $\exp(-\Delta\varepsilon_{m,n}^2/2\sigma^2)$. Each set of offsets, $\{\varepsilon_{m,n}\}$, defines a configuration (or "realization") of disorder within the ensemble. The Hamiltonian $H_0 + H_{diag}$ from Eqs. 4-1 and 4-13was numerically diagonalized for each configuration, from which an infrared spectrum was assembled using Eq. 4-6. The ensemble spectrum was constructed from averaging together 10^3 such configuration-specific spectra.

For a given disorder width, σ, the impact of diagonal disorder can vary greatly depending on the degree of spatial correlation.[48, 49] Short- and long-range broadening represent the extremes in spatial correlation: in short-range broadening each $\varepsilon_{m,n}$ is selected independently from all others along a chosen direction (i.e., along the polymer backbone or along the stacking axis), whereas in long-range broadening all $\varepsilon_{m,n}$ along a chosen direction and within a given configuration are identical and equal to $\Delta\varepsilon_C$ (although $\Delta\varepsilon_C$ is selected randomly from a Gaussian distribution of width σ). For a π-stack, short- and long-range broadening along each of the two directions defines four general cases, denoted as LL (isotropic long-range), LS (long-range along the polymer axis, short-range along the stacking axis), SL (short-range along the polymer axis, long-range along the stacking axis), and SS (short-range along both axes). The four cases are depicted schematically in Fig. 4-5.

Fig. 4-6 shows the ensemble-averaged infrared spectra for 4 × 4 π-stacks for each of the four broadening cases of Fig. 4-5, using the physically realistic electronic couplings and HR factors for P3HT from Fig. 4-2(d).

Figure 4-5

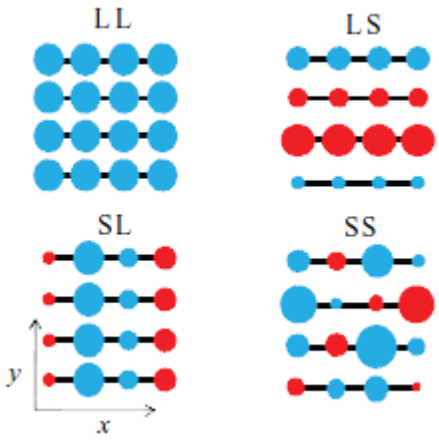

Fig. 4-5. Schematic representations of the four spatial correlation limits of site disorder in a 4 × 4 π-stack for the: LL: isotropic long-range broadening; LS: long-range (short-range) broadening along the polymer x-axis (π-stacking yaxis); SL: short-range (long-range) broadening along the x-axis (y-axis); and SS: isotropic short-range broadening. The radius of the monomer-unit circle at (m,n) is proportional to the magnitude of the site energy, $|\varepsilon_{mn}|$. The color indicates the sign of the deviation, ε_{mn}.

For isotropic long-range broadening (LL), disorder has no effect at all on the spectrum since the hole energy within a given π-stack configuration is entirely independent of monomer position, i.e., $\varepsilon_{m,n} = \varepsilon_C$ in each configuration. The value ε_C adds to all state energies equally – including the ground state – and thus does not contribute to the *transition* frequency. In this limit, disorder has no impact on the line shape and line broadening is entirely homogeneous as in Fig. 4-2(d)

In Fig. 4-6(b) long-range broadening occurs within the polymer while short-range broadening occurs between polymers ("LS"). Hence, the hole energy is the same for all

monomer units in a given polymer chain, but this energy varies randomly between chains; the hole energy therefore depends only on the chain index n; $\varepsilon_{m,n} = \varepsilon_n$. Fig. 4-6(c) (SL) shows the reverse case from Fig. 4-6(b). Here, the hole-energy varies randomly along a given polymer chain, but not between chains; the hole energy depends only on m, i.e., $\varepsilon_{m,n} = \varepsilon_m$. Finally, in Fig. 4-6(d) short-range broadening occurs isotropically (SS); within a given π-stack configuration all hole energies are spatially uncorrelated. In this limit disorder is expected to have the greatest impact on the absorption spectrum.

Figure 4-6

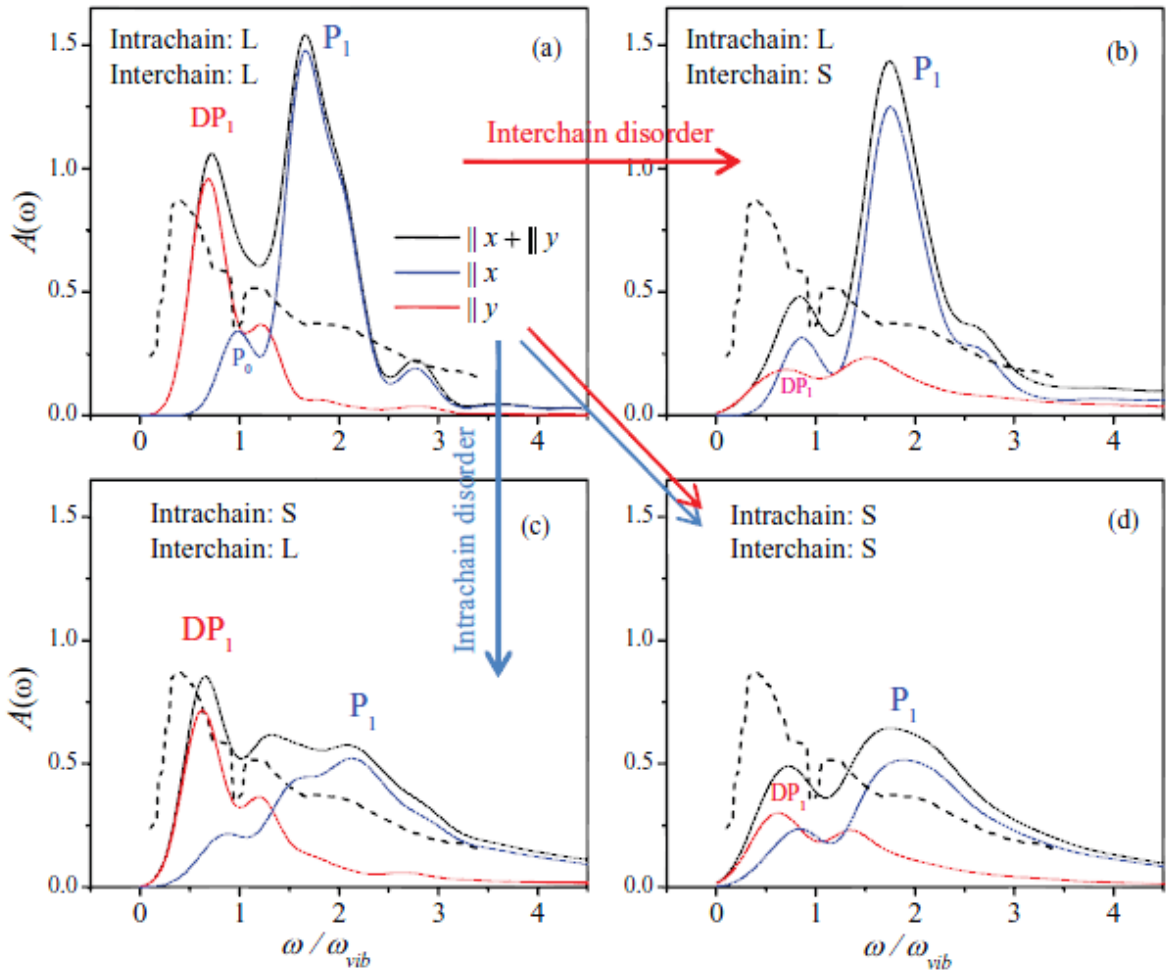

Fig. 4-6. Polaron absorption spectra for 4 × 4 π-stacks according to the four correlated disorder models (a)–(d) of Fig. 5. The parameters used are: $t_{intra} = -0.3$ eV, $t_{inter} = -0.15$ eV, $\omega_{vib} = 0.175$ eV/$\hbar$, and $\lambda^2 = 1$. In all

cases the standard deviation of the Gaussian distribution of polaron energies is $\sigma = 0.20$ eV and the homogeneous line width is = 0.03 eV. One thousand randomly generations disorder configurations were averaged together to create the spectra. The black dotted curve is the experimental transient induced absorption spectrum for (>99%) regioregular P3HT films cast from xylene from Ref. (citation) (sans the sharp IRAVs). Arrows show direction of increasing interchain (red) and intrachain (blue) short range disorder.

Fig. 4-6 clearly shows that the spatial correlation plays a very large role in the shape of the infrared absorption spectrum. It is apparent in all cases that increasing short-range disorder leads to an attenuation of the spectrum: the spectra with at least one component of short-range broadening are less intense than the LL spectrum in Fig. 4-6(a). The short range disorder-induced attenuation arises because the oscillator strength is dependent on the electronic coupling (see, for example, Eqs. 4-10(a) and 4-11(a)) so that as disorder increases and the monomer units become energetically isolated the associated trapped hole states can no longer absorb infrared photons. Note that the oscillator strength is not simply redistributed as is the case in a UV-Vis spectrum; hole absorption in the present model lacks an oscillator strength sum rule, in contrast to the case of optical absorption of neutral excitons. Interestingly, Fig. 4-6 also shows that the interchain (*y*-polarized) and intrachain (*x*-polarized) components of the spectrum respond *selectively* to the interchain and intrachain short-range components of disorder, respectively. Hence, comparing the SL case (Fig. 4-6(c)) to the LL case in Fig. 4-6(a), one sees a dramatic drop in just the *x*-polarized spectrum: the P_1 intensity decreases by a factor of three, while DP_1 is attenuated by only 30%. The effect is even more pronounced in the LS case (Fig. 4-6(b)), where DP_1 drops by about a factor of four due to short-range disorder along the stacking axis, while P_1 is hardly affected at all. When short-range disorder occurs

isotropically as in Fig. 4-6(d), both polarization components are strongly attenuated – by about a factor of two for the value of σ used in the figure.

B. Off-diagonal disorder

X-ray diffraction studies by Salleo and co-workers[11, 13] have revealed the presence of paracrystallinity in poly(2,5-bis(3-tetradecylthiophen-2-yl)thieno[3,2,-b]thiophene) (PBTTT),[13] and P3HT[11] films, in which significant deviations exist in the π-stacking distance about its equilibrium value, d. The paracrystallinity parameter g is defined as $\sigma d/d$, where σd is the standard deviation of π-stacking distances which are assumed to be normally distributed about d. Hence, an increasing value of g represents increasing disorder; a film with a g value of greater than 0.1–0.15 is considered amorphous.[11, 13]

In paracrystalline π-stacks the interchain coupling between chain n and chain $n+1$ is given by,[11, 13] $t_{inter}(n) = t_{0inter} \exp(-\beta d_n)$ where $d + d_n$ is the distance between the two chains and t_{0inter} is the coupling corresponding to $d_n = 0$. The factor β represents how rapidly the interchain orbital overlap diminishes with increasing separation and was taken here to be $\beta = 2.35$ Å^{-1}, the value calculated using DFT in Ref. 13. The deviation in the interchain coupling appearing in Eq. 4-14 is thus, $t_n \equiv t_{inter}(n) - t_{0inter}$.

As with diagonal disorder, off-diagonal disorder can be short- or long-range. The two limits are depicted in Fig. 4-7. For short-range broadening, all of the d_n are chosen independently of each other within each configuration, while in long-range broadening all d_n are the same within any given configuration ($d_n = d_C$), although d_C remains randomly distributed. The impact of increasing g on the hole absorption spectrum for off-diagonal disorder was investigated by numerically diagonalizing the Hamiltonian $H_0 + H_{off\ diag}$ in

Eqs. 4-1 and 4-14 for each randomly generated configuration and spectral averaging over 10^3 configurations. (Diagonal disorder is suppressed in order to focus on the effect of paracrystallinity alone.) The results for long- and short-range broadening are shown in Figs. 4-8(a) and 4-8(b), respectively. The figure shows that, as with diagonal disorder, increasing off-diagonal disorder in the stacking direction (*y*) leads to a selective attenuation of just the *y* polarized spectrum – hence, DP_1 is increasingly attenuated with increasing *g* in a manner which is significantly greater for short-range broadening, while the *x*-polarized spectrum hosting P_0 and P_1 is largely unaffected. Interestingly, the first peak in the unpolarized spectrum (with contributions from *both* DP_1 and P_0) shifts to the blue with increasing *g* by ≈300 cm^{-1} as *g* ranges from 0 to 0.1 in both broadening limits. This could account for the increasing blue shift with side-chain length in P3AT films observed by Vardeny and co-workers,[18, 19] although the overall line shape for paracrystalline disorder alone (sans diagonal disorder) in Fig. 4-8 does not agree well with the measured spectrum of Vardeny's (see Figs. 4-4 and 4-6). A far more realistic description should involve the *simultaneous* presence of diagonal and off diagonal disorder,[11] as variations in the π-stacking distances in paracrystalline films also induce fluctuations in the hole energies arising from charge – induced dipole interactions which scale as the inverse fourth power of distance.[45] In Sec. 4-5 we include both forms of disorder in an attempt to quantitatively account for the measured infrared spectral line shape.

Figure 4-7

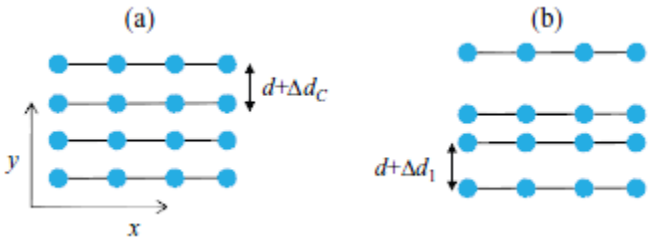

Fig. 4-7. Schematic representations of paracrystalline disorder in a 4 × 4 π-stack. In long-range broadening (a) all nearest neighbor distances are equal to $d + d_C$ within a given configuration, but d_C differs between configurations. (b) In short-range broadening d is spatially uncorrelated and there are generally three independent deviations, d_n (n = 1, 2, 3) within each configuration. In both cases (a) and (b), the d's are selected from a Gaussian distribution with standard deviation, σ_d.

Figure 4-8

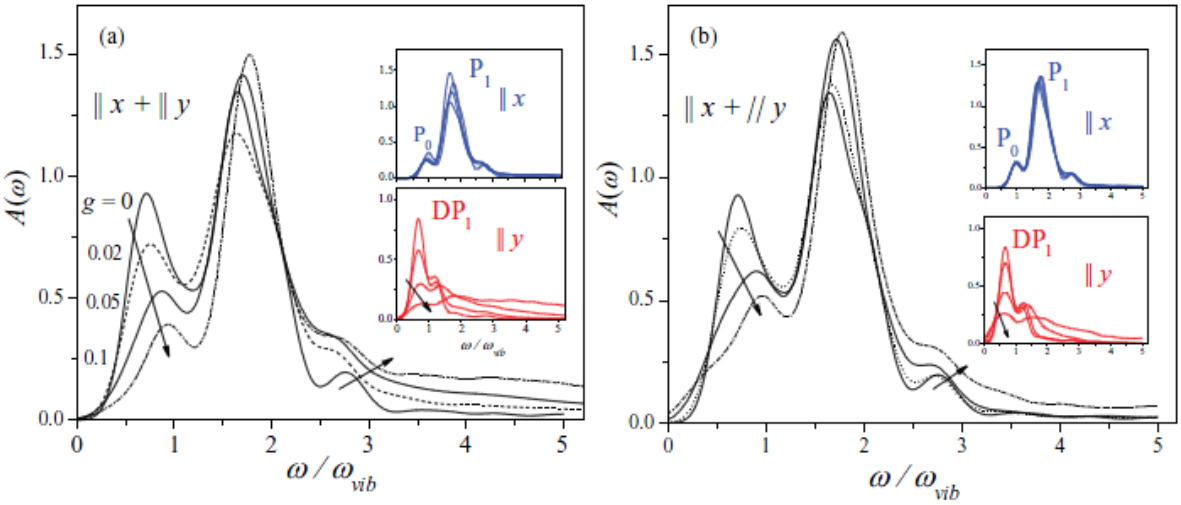

Fig. 4-8. Polaron absorption spectra for 4 × 4 π-stacks with (a) short-range and (b) long-range paracrystalline disorder. Spectra are shown for several values of g. The electronic and vibrational parameters are identical to those in Fig. 4-5. In all cases the homogeneous line width is _ = 0.035 eV. One thousand randomly generations disorder configurations were averaged together to create the spectra. Arrows indicate the direction of increasing g.

4-5. Comparison to Experiment

The mid- to near-infrared absorption spectra of a variety of P3AT films have been measured using transient pump-probe spectroscopy by Vardeny and co-workers.[18, 19] and charge modulation spectroscopy by Sirringhaus and coworkers.[12, 20, 21, 50] The spectral line shape and intensity were shown to depend on the solvent used in spin casting, the length of the alkyl side chains, and the polymer molecular weight. According to Fig. 4-6 the (unpolarized) induced absorption spectrum of Vardeny and co-workers[14, 15] for a (>99%) regioregular P3HT spin cast from xylene is best described by the SL diagonal disorder model, where short-range disorder occurs primarily along the polymer backbone. The calculated unpolarized spectrum in Fig. 4-6(c) (x+y) reproduces the general line shape including the relative peak heights and the dip at almost exactly one vibrational quantum. However, the first main peak due mainly to interchain charge transfer is calculated to be at approximately 900 cm^{-1}, at least 250 cm^{-1} higher than the measured value. In order to address this discrepancy we increased the size of the π-stack from 4 × 4 (used in Fig. 4-6) to 5 × 5 in order to take advantage of the redshift of the first (intraband) peak predicted by Eq. 4-(a). We also slightly fine-tuned the inter- and intrachain couplings. The resulting spectrum is shown in Fig. 4-9, where very good agreement with experiment is now achieved. The first peak is only slightly higher (<100 cm^{-1}) than the measured value, while the dip remains at $\omega \approx \omega^{vib}$. Moreover, the blue tail, which is most sensitive to our choice of σ (= 0.20 eV) , is in excellent agreement with experiment. Further changes in the IR spectrum for larger π-stacks are minimal if the (intrachain) polaron coherence length, defined largely by the ratio $|t_{intra}/\sigma|$, is smaller than five thiophene units. Our preliminary investigations show the coherence length to be around

four-five units, similar to what was found for neutral excitations in Ref. 36. Hence, we cannot discount some additional spectral evolution in larger π-stacks which may require slight readjustments in the disorder parameters to re-establish good agreement with experiment. In a later chapter, we will report further on the polaron coherence function and its relation to the infrared spectral line shape.

Figure 4-9

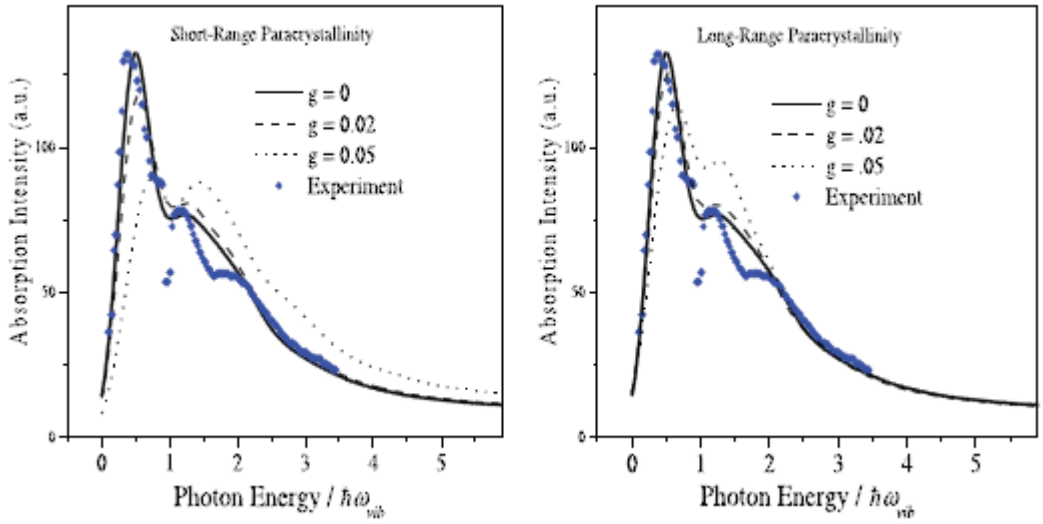

Fig. 4-9. Calculated absorption spectra ($x + y$) for 5 × 5 π-stacks with SL diagonal disorder (σ = 0.20 eV) as well as (a) short-range and (b) long-range paracrystalline disorder. Spectra are shown for several values of the paracrystalline parameter g. In all cases t_{inter} = −0.135 eV and t_{intra} = 0.26 eV. The vibrational parameters are ω_{vib} = 0.174 eV/$\hbar$ and λ^2 = 1 and the homogeneous line width is Γ = 0.035 eV. One thousand randomly generated disorder configurations were averaged together to create the spectra. The blue dotted spectra are the measured spectra reproduced from Ref. (citation 18) but without the sharp anti-resonances.

Fig. 4-9 also shows the effect of increasing paracrystallinity. Based on x-ray diffraction analysis[11] g values have been shown to increase significantly with polymer molecular weight for P3HT. Beyond approximately 100 thiophene units, the polymer morphology becomes entangled, and g levels off to ≈0.06–0.07. The entanglement

regime is defined by locally ordered aggregates in which the π-stacks contain folded polymers/polymer segments, separated by amorphous regions connect by tie chains.[51] Our results in Fig. 4-9 show that the first main peak, which is largely interchain in nature, decreases significantly with increasing g with the best agreement with experiment occurring for $g<\sim 0.02$. Generally, long-range paracrystallinity has a slightly smaller impact than short-range paracrystallinity as anticipated from Fig. 4-8. Unfortunately, the molecular weight (MW) of P3HT was not reported in Ref. (citation 18) so we cannot access if the polymer film used in those measurements was in the entanglement limit. Our results would better support the lower MW (paraffinic limit) where g is measured to be significantly lower, in the range 0.02–0.04.[11] We point out, however, that the calculated spectra are also sensitive to our choice of β, through the product βg (see Sec. 4-4). This means that the spectrum with $g = 0.02$ and $\beta = 2.35$ Å^{-1} is also consistent with $g = 0.05$ if β is reduced to unity. A value of $\beta = 1.18$ Å^{-1} was employed by Wu and Conwell in their analysis of MEH PPV aggregates.[38]

The effect of molecular weight on the infrared absorption spectrum was studied by Chang *et al*[12]. using CMS spectroscopy. Ignoring the sharp antiresonances (as is also done here), the authors of Ref. 12 observed that the lower MW spectra are blueshifted and strongly attenuated relative to the higher MW spectra, as shown in Fig. 4-10. Of particular relevance here, the first vibronic peak (mainly due to DP_1) is significantly attenuated relative to the second in going from the high to low MW films, consistent with an increase in interchain disorder. Compared to the Vardeny spectra in Fig. 4-9, the Sirringhaus spectra are somewhat broader, especially in the high energy region. This may reflect an inherent difference in the experimental techniques used to obtain the spectra;

for example, charge modulation spectroscopy used in Ref. 12 may result in a greater hole population and a broader distribution of electric fields, which, through the Stark effect, provides a source of additional inhomogeneous broadening.

Figure 4-10

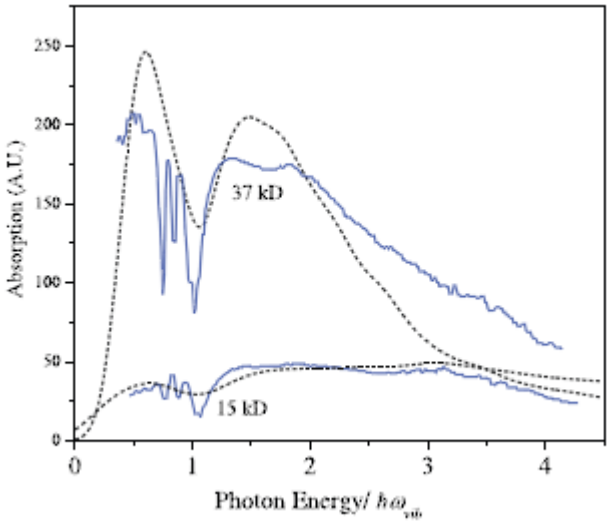

Fig. 4-10. Blue curves correspond to the experimental CMS spectra of Ref. (citation 12) for high (37 kD) and low (15 kD) MW P3HT films spin cast from trichlorobenzene. Dashed curves are calculated absorption spectra ($x + y$) for 5 × 5 π-stacks. For the high MW spectrum: $t_{inter} = -0.15$ eV and $t_{intra} = -0.36$ eV with SL diagonal disorder, $\sigma = 0.20$ eV, and paracrystalline disorder, $g = 0.025$. The homogeneous line width is $\Gamma = 0.018$ eV. For the low MW spectrum: $t_{inter} = -0.15$ eV and $t_{intra} = -0.26$ eV with isotropic (SS) disorder, $\sigma = 0.4$ eV, no paracrystalline disorder, $g = 0$, and $\Gamma = 0.03$ eV. In both low and high MW spectra $\omega_{vib} = 0.174$ eV/$\hbar$ and $\lambda^2 = 1$. Two thousand randomly generated disorder configurations were averaged together to create the spectra.

In Ref. 12 the PKS[25] and Piepho[26] models were used to treat interchain charge transfer between a single donor and a single acceptor chromophore (polymer chain) and it was concluded that the higher MW samples have *inter*chain couplings about 50% larger and reorganization energies about four times *smaller* than the lower MW samples. Within

the present formalism the general trends observed in Ref. 12 can be explained with essentially no change in either the interchain coupling or the reorganization energy with MW. Instead, very good agreement with experiment is obtained by increasing the *intrachain* coupling ($|t_{intra}|$) by approximately 50% and by significantly reducing the diagonal energy disorder (σ) in going from the low to high MW polymers, as demonstrated in Fig. 4-10.

The increase in intrachain coupling and decrease in disorder in the high MW films is fully consistent with our analysis of neutral exciton photoluminescence in low and high MW P3HT films. In Ref. 36 it was concluded that the higher MW polymers maintained greater intrachain order within the crystalline domains of the entangled phase compared to the lower MW polymers in the paraffinic phase. By carefully analyzing peak ratios in the PL spectra the hole transfer integral, $|t_{intra}|$, was estimated to increase from ≈0.21 eV in low MW films to ≈0.26 eV in the higher MW films. In Fig. 4-10 the calculated spectra for 5 × 5 π-stacks employ slightly higher values of $|t_{intra}|$ (0.26 eV for 15kD and 0.36 eV for 37 kD) but maintain the trend with increasing MW. By contrast, the interchain coupling was held constant, with $t_{inter} = -0.15$ eV for both MWs. This was done because the interchain coupling is most sensitive to the *mean* π-stacking distance, which should not be seriously affected by MW. This is not true, however, for the standard deviation (g) which actually *increases* in the higher MW samples, as shown by Salleo and co-workers.[11] In order to show that the current approach can accommodate Salleo's observations, we increased g from zero in the 15 kD film to 0.025 in the 37 kD film. By itself, this would result in a damping of the first peak (composed of DP_1+P_0 in the unpolarized spectrum) relative to P_1 as demonstrated in Fig. 4-8. However, the opposite

trend is observed in the calculated spectra in Fig. 4-10. This is due to the more dominant impact of increasing energetic site disorder.

Increasing diagonal disorder is very likely responsible for the fourfold decrease of the infrared spectral intensity as well as the attenuation of the first vibronic peak (relative to the second) observed in going from the higher to lower MW P3HT films. Increased disorder in the lower MW films is also consistent with the lower measured mobilities.[12] In our calculated spectra we treated the 37 kD films in the SL limit with $\sigma = 0.2$ eV. For the 15 kD films σ was doubled and the disorder was made isotropic (SS). The net effect is a strong overall spectral attenuation and a drop in DP_1 relative to P_1, in very good agreement with the observations of Ref. 4-12. The essence of the effect can also be seen by comparing the spectra in Figs. 4-6(c) and 4-6(d). A significant but smaller increase in site disorder in the lower MW samples (by a factor of ≈1.2) was also the conclusion reached in Ref. 36, but with reference to the transition energies of the *neutral exciton*. Disorder in the latter derives from deviations in the nonresonant environmental shift (D),[44] a fundamentally different quantity than the deviation in hole energies of relevance here. The former scales as R^{-6} while the latter scales as R^{-4} leading to *larger* standard deviations in the hole energies – by as much as a factor of three, as originally pointed out by Bassler, for diagonally disordered organic materials.[45] Interestingly, the value of σ (= 0.2 eV) used to reproduce the measured spectral line shapes in Figs. 4-9 and 4-10 (37 kD film) is about three times larger than that used to reproduce the absorption spectra of neutral excitons in Ref. 36, in line with Bassler's predictions.

4-6 Conclusion

The Holstein Hamiltonian represented in a basis set truncated to include one and two-particle states provides an excellent description of positively charged polarons in conjugated polymers chains and π-stacked aggregates. The measured hole infrared absorption spectra in P3HT films obtained via induced absorption[18, 19] and charge modulation[12, 20, 21] spectroscopies are quantitatively reproduced, correctly capturing the peak positions and relative peak intensity ratios in spectral line shapes rich in vibronic structure. A detailed analysis of diagonal and off diagonal disorder resolved along the polymer backbone and along the π-stacking axis adds new insight into the dominant role played by disorder in governing photophysical properties: disorder – either diagonal or off diagonal – directed along the polymer backbone (*x*-axis) selectively attenuates the x-polarized region of the absorption spectrum, while disorder directed along the interchain (*y*) axis selectively attenuates the *y*-polarized region of the spectrum. Hence, in order to unravel the nature of disorder in these technologically important materials further experiments are needed on oriented "crystalline" samples.

One of the more intriguing results of our nonadiabatic approach is the prediction of a new low energy peak, P_0, polarized along the polymer axis and hence observable in isolated, single chains with sufficient disorder to trap polarons. P_0 is slightly higher in energy than DP_1, peaking at an energy slightly smaller than a vibrational quantum, around 1000 cm^{-1}. Indeed, Vardeny and co-workers have recorded IRAV activity in this spectral region for *unaggregated* P3ATs.[19] The presence of the broader P_0 resonance may enhance the IRAVs, a hypothesis we are currently exploring.

Future work will be directed at applying our disorder model to better understand charge transport in conjugated polymer films. Hole mobilities have been shown by several groups to increase with molecular weight.[11, 12, 20, 52, 53] Fundamental questions remain as to the nature of the increase, be it primarily due to increased electronic coupling, reduced nuclear relaxation energy, reduced disorder (as is championed here) or a complex combination thereof.

REFERENCES

1. Braun, D. and Heeger, A. J. Appl. Phys. 1991, Lett. **58**(18), p. 1982–1984.

2. Sirringhaus, H.; Tessler, N.; Friend, R. H. Science 1998, **280**(5370), p. 1741–1744

3. Bredas, J.-L.; Norton, J. E; Cornil, J.; Coropceanu, V. Acc. Chem. Res. 2009, **42**(11), p. 1691–1699.

4. Ma, W. L.; Yang, C. Y.; Gong, X.; Lee, K.; Heeger, A. J. Adv. Funct. Mater. 2005, **15**(10), p. 1617–1622.

5. Brabec, C. J.; Gowrisanker, S.; Halls, J. J. M.; Laird, D.; Jia, S. J.; Williams, S. P. Adv. Mater. **22**(34), P. 3839–3856 (2010).

6. Brabec, C. J.; Sariciftci, N. S.; Hummelen, J. C. Adv. Funct. Mater. 2001, **11**(1), p. 15–26.

7. Bredas, J. L. and Street, G.B. Acc. Chem. Res. 1985, **18**(10), p. 309–315

8. Beljonne, D.; Cornil, J.; Sirringhaus, H.; Brown, P.J.; Shkunov, J. L.; Friend, R. H.; Bredas, J.L. Adv. Funct. Mater 2001, **11**(3), p. 229–234.

9. Gomes da Costa, P.; Dandrea, R. G.; Conwell, E. M. Phys. Rev. B 1993, **47**(4), p. 1800–1810.

10. Vogl, P. and Campbell, D. K. Phys. Rev. Lett. 1989, **62**(17), p. 2012–2015.

11. Noriega, R.; Rivnay, J.; Vandewal, K.; Koch, F. P. V.; Stingelin, N.; Smith, P.; Toney; M. F.; Salleo, A. Nat. Mater. 2013, **12**(11), p. 1038–1044.

12. Chang, J.-F.; Sirringhaus, H.; Giles, M.; Heeney, M.; McCulloch, I. Phys. Rev. B 2007, **76**, P. 205204.

13. Rivnay, J.; Noriega, R.; Northrup, J. E.; Kline, R. J.; Toney, M. F.; Salleo, A. Phys. Rev. B 2011, **83**(12), p. 121306.

14. McMahon, D. P.; Cheung, D. L.; Goris, L.; Dacuña, J.; Salleo, A.; Troisi, A. J. Phys. Chem. C 2011, **115**(39), p. 19386–19393.

15. Poelking, C. and Andrienko, D. Macromolecules 2013, **46**(22), p. 8941–8956.

16. Meisel, K. D.; Vocks, H.; Bobbert, P.A. Phys. Rev. B 2005, **71**(20), p. 6.

17. Fishchuk, I. I.; Kadashchuk, A.; Hoffmann, S. T.; Athanasopoulos, S.; Genoe, J.; Bassler, H.; Kohler, A. Phys. Rev. 2013, B **88**, 125202.

18. Osterbacka, R.; An, C. P.; Jiang, X. M.; Vardeny, Z. V. Science 2000, **287**, p. 839–842.

19. Jiang, X. M.; Osterbacka, R.; Korovyanko, O.; An, C. P.; Horovitz, B. ; Janssen, R. A. J.; Vardeny, Z.V. Adv. Funct. Mater. 2002, **12**(9), p. 587–597.

20. Chang, J. F.; Clark, J.; Zhao, N.; Sirringhaus, H.; Breiby, D. W.; Andreasen, J. W.; Nielsen, M. M.; Giles, M.; Heeney, M.; McCulloch, I. Phys. Rev. B 2006, **74**(11), p. 115318.

21. Sirringhaus, H.; Brown, P. J.; Friend, R. H.; Nielsen, M. M.; Bechgaard, K.; Langeveld-Voss, B. M. W.; Spiering, A. J. H.; Janssen, R. A. J.; Meijer, E. W.; Herwig, P.; de Leeuw, D. M. Nature 1999, **401**, p. 685.

22. Prosa, T. J.; Winokur, M. J.; McCullough, R. D. Macromolecules 1996, **29**, p. 3654–3656.

23. Prosa, T. J.; Winokur, M. J.; Moulton, J.; Smith, P.; Heeger, A. J. Macromolecules 1992, **25**, p. 4364–4372.

24. Piepho, S. B. J. Am. Chem. Soc. 1990, **112**(11), p. 4197–4206.

25. Piepho, S. B. J. Am. Chem. Soc. 1988, **110**(19), p. 6319–6326.

26. Piepho, S. B.; Krausz, E. R.; Schatz, P. N. J. Am. Chem. Soc. 1978, **100**(10), p. 2996–3005.

27. Creutz, C. and Taube, H. J. Am. Chem. Soc. 1969, **91**(14), p. 3988–3989.

28. Holstein, T. Ann. Phys. 1959, **8**, p. 325–342.
29. Philpott, M. R. J. Chem. Phys. 1971, **55**, p. 2039–2054.

30. Spano, F. C. J. Chem. Phys. 2002, **116**, p. 5877–5891.

31. Stradomska, A. and Petelenz, P. J. Chem. Phys. 2009, **131**(4), p. 044507.

32. Spano, F. C. J. Chem. Phys. 2005, **122**, p. 234701.

33. Spano, F. C. Chem. Phys. 2006, **325**, p. 22–35.

34. Clark, J.; Silva, C.; Friend, R. H.; Spano, F. C. Phys. Rev. Lett. 2007, **98**(20), p. 206406.

35. Yamagata, H and Spano, F. C. J. Chem. Phys. 2012, **136**(18), p. 184901
.

36. Paquin, F.; Yamagata, H.; Hestand, N. J.; Sakowicz, M.; Bérubé, N.; Côté, M.; Reynolds, L. X.; Haque, S. A.; Stingelin, N.; Spano, F. C.; Silva, C. Phys. Rev. B 2013, **88**(15), p. 155202.

37. Hush, N. S. Coord. Chem. Rev. 1985, **64**, p. 135–157.

38. Wu, M. W. and Conwell, E. M. Phys. Rev. B 1997, **56**(16), p. 10060–10062.

39. We note that tintra corresponds to the hole transfer between the local HOMO's of adjacent thiophene rings and is therefore substantially smaller than the value of approximately −2.5 eV between p-orbitals involved in a double bond. Since a single-ring HOMO is delocalized over four carbon p-orbitals, tintra should be less than about 1/4 of the p-orbital value, or about −0.6 eV.

40. Northrup, J. E. Phys. Rev. B 2007, **76**(24), p. 245202.

41. Wohlgenannt, M.; Jiang, X. M.; Vardeny, Z. V. Phys. Rev. B 2004, **69**(24), p. 4.

42. Mizes, H. A.; Conwell, E. Phys. Rev. Lett. 1993, **70**, p. 1505–1508.

43. Emin, D. Phys. Rev. B 1986, **33**, p. 3973–3975.

44 Hoffmann, S. T.; Bassler, H.; Kohler, A. J. Phys. Chem. B 2010, **114**(51), p. 17037–17048.

45. Bassler, H. Phys. Status Solidi B 1981, **107**, p. 9.

46. Beenken, W. J. D. Phys. Status Solidi A 2009, **206**(12), p. 2750–2756.

47. Coropceanu, V.; Cornil, J.; da Silva, D. A.; Olivier, Y.; Silbey, R.; Bredas, J. L.; Chem. Rev. 2007, **107**(4), p. 926–952.

48. Knapp, E. W. Chem. Phys. 1984, **85**, p. 73–82.

49. Spano, F. C.; Clark, J.; Silva, C.; Friend, R. H. J. Chem. Phys. 2009, **130**(7), p. 074904.

50. Brown, P. J.; Thomas, S. D.; Kohler, A.; Wilson, J. S.; Kim, J.S.; Ramsdale, C. M.; Sirringhaus, H.; Friend, R. H. Phys. Rev. B 2003, **67**, p. 064203.

51. Reid, O. G.; Pensack, R. D.; Song, Y.; Scholes, G. D.; Rumbles, G. Chem.

Mater. 2014, **26**, p. 561.

52. Goh, C.; Kline, R. J.; McGehee, M. D.; Kadnikova, E. N.; Frechet, J. M. J. Appl. Phys. Lett. 2005, **86**(12), p. 122110.

53. Koch, F. P. V.; Rivnay, J.; Foster, S.; Müller, C.; Downing, J. M.; Buchaca-Domingo, E.; Westacott, P.; Yu, L; Yuan, M. J.; Baklar, M.; Fei, Z. P.; \ Luscombe, C.; McLachlan, M. A.; Heeney, M.; Rumbles, G.; Silva, C.; Salleo, A.; Nelson, J.; Smith, P.; Stingelin, N. Prog. Polym. Sci. 2013, **38**, p. 1978–1989.

CHAPTER 5

POLARON COHERENCE FUNCTIONS

5-1 Introduction

The spatial coherence length of charges in organic electronic systems has been receiving an increasing amount of attention, as it becomes clearer that long range room temperature coherence may be achieved in conjugated organic materials even in the presence of coupling to quantum mechanical vibrations in these systems.[1,2] Recent reports of 40-60 angstrom delocalization of a positive charge (hole) in poly(3-hexylthiophene) (P3HT) by Poluektov and coworkers[10] were taken as evidence of significant spatial coherence range of polarons. In this chapter we investigate the coherence of positively charged polarons in 2 dimensional conjugated polymer π-stacks.

In a recent work we calculated the coherence functions of polarons in poly (3-hexylthiophene) P3HT π-stacks as a function of diagonal site energy disorder using a Holstein-based Hamiltonian.[3] That kind of disorder arises from the different environment each repeat unit experiences in a real sample, due to the quasi-amorphous nature of the material. The coherence functions were shown to be highly sensitive to energetic site disorder which is represented as a random distribution of hole energies.[7] In what follows we evaluate the polaron coherence function corresponding to a two-dimensional P3HT π-stack including paracrystalline disorder, which is off-diagonal disorder in the intermolecular couplings, as well as diagonal site disorder. Then we combine both diagonal and off-diagonal disorder to calculate the coherence functions of polarons in real P3HT π-stack thin films.

5-2 Hamiltonian and Basis Set

Here we introduce the Hamiltonian and eigenstates for a hole-type polaron in a 2-dimensional P3HT π-stack. In this 2D model we treat each of the individual thiophene units as its own chromophore where only the local HOMO of each thiophene unit is retained. A hole represents a missing electron in the HOMO of a single thiophene unit. The hole transfer integral, t_{intra} couples local HOMO's of neighboring rings to each other, while wave function overlap between neighboring thiophene HOMOs on adjacent chains leads to interchain electronic coupling, represented by the transfer integral, t_{inter}. This course-grained approach on a P3HT lattice has previously been used to study holes[3] as well as neutral excitons[4,5] where the thiophene LUMO was also retained in the case of neutral excitons

Our model utilizes the two particle approximation, where the basis set is limited to one- and two-particle states. A one-particle state, denoted $|m,n,\tilde{\nu}\rangle$ indicates the location of the hole in two dimensions (m and n) and includes a vibrational excitation $\tilde{\nu}$, which in our model can consist of 0 to 4 vibrational quanta each with an energy of 1400 cm^{-1}. A two-particle state is denoted by $|m,n,\tilde{\nu};m',n',\nu'\rangle$, and consists of a one-particle state, plus a pure vibrational excitation ν', on a different site, m',n', which is charge neutral (filled HOMO), and may also have 0 to 4 vibrational quanta.

We employ a site based Holstein Hamiltonian, where nuclear potentials for the molecular vibrations in the ground state and cationic state of a given thiophene chromophores are shifted harmonic wells of identical curvature. In the vector subspace containing one hole in a N x N square π-stack, the Hamiltonian is:

$$H_0 = \sum_{m=1}^{N-1}\sum_{n=1}^{N} t_{intra}\{|m+1,n\rangle\langle m,n| + h.c.\}$$
$$+ \sum_{m=1}^{N}\sum_{n=1}^{N-1} t_{inter}\{|m,n+1\rangle\langle m,n| + h.c.\} + \hbar\omega_{vib}\sum_{m=1}^{N}\sum_{n=1}^{N} b_{m,n}^{\dagger}b_{m,n}$$
$$+ \hbar\omega_{vib}\lambda\sum_{m=1}^{N}\sum_{n=1}^{N}(b_{m,n}^{\dagger} + b_{m,n})|m,n\rangle\langle m,n| + \hbar\omega_{vib}\lambda^2 \quad (5\text{-}1)$$

where h.c. means Hermitian conjugate. The first two terms represent the electronic coupling along and across chains, and the remaining terms describe local vibronic coupling involving the symmetric aromatic/quinoidal stretching vibration. The operators $b_{m,n}^{\dagger}$ and $b_{m,n}$, respectively, create and annihilate vibrational quanta on the thipohene unit at position (m,n) within the ground (S_0) potential well. The Huang-Rhys (HR) factor λ^2 represents the relaxation of a single thiophene unit after ionization, and it is unity in all the cases presented here, representing a shifted potential well in the ionized state compared to the ground state.

Electronic coupling acts to mix the one- and two-particle states such that the αth eigenstate of H in equation 5-1 can be written as

$$|\Psi^{(\alpha)}\rangle = \sum_{n,m,\tilde{\nu}} c_{n,m,\tilde{\nu}}^{(\alpha)}|n,m,\tilde{\nu}\rangle + \sum_{n,m,\tilde{\nu}}\sum_{n',m',\nu'} c_{n,m,\tilde{\nu};n'm'\nu'}^{(\alpha)}|n,m,\tilde{\nu};n',m',\nu'\rangle \quad (5\text{-}2)$$

The one- and two-particle expansion coefficients can be readily obtained numerically.

5-3 Disorder

In this section we describe how we accounted for the disorder that exists in real polymer film systems. We distinguish two different types of disorder, diagonal, which effects the site energies of hole states, and off-diagonal, which effects the coupling between sites. Both forms of disorder are cause by inhomogeneous polarizing environments surrounding the hole due to disturbances in intrachain and interchain order. There are several sources of this inhomogeneity, including variations in the nearest-neighbor π-stacking distance, called paracrystallinity, as well as intramolecular torsional angles within the polymer. It may also come about because of spatially varying local electric fields from a distribution of holes in the sample. Disorder is represented as random changes in the hole energy, $\Delta\varepsilon_{m,n}$, when the hole resides on the monomer (m,n) as well as random changes in the interchain transfer integrals, Δt_n, between chain n and chain n+1. The Hamiltonian for a disordered N x N π-stack is given by

$$H = H_0 + H_{diag} + H_{offdiag} \tag{5-3}$$

where $H_0$is the disorder-free Hamiltonian of equation 1 and

$$H_{diag} = \sum_{m=1}^{N}\sum_{n=1}^{N} \Delta\varepsilon_{m,n}|m,n\rangle\langle m,n| \tag{5-4}$$

and

$$H_{off\ diag} = \sum_{m=1}^{N}\sum_{n=1}^{N} \Delta t_n\{|m,n+1\rangle\langle m,n| + |m,n\rangle\langle m,n+1|\} \tag{5-5}$$

5-4 Paracrystalline Disorder

In this section we introduce the coherence function as a means of determining the coherence length of a hole in P3HT, and we perform a systematic analysis of the effect of paracrystalline (off-diagonal) disorder, without the presence of site energy (diagonal) disorder. The spatial coherence function corresponding to the ground state polaron in a 2D π-stack is given by,

$$C(r) \equiv \langle \langle \Psi_\alpha | \sum_R P_R^\dagger P_{R+r} | \Psi_\alpha \rangle \rangle_C \tag{5-6}$$

where $P_{\boldsymbol{R}}^\dagger \equiv |\boldsymbol{R};vac\rangle\langle g;vac|$ creates a hole at the monomer site $\boldsymbol{R}$ with no vibrational quanta relative to the unshifted potential well of the neutral monomer. Here, the vector $\boldsymbol{R}$ = (*n*,*s*) locates the *n*th monomer repeat unit on the *s*th chain. Ψ_α refers to the polaron eigenstate of interest. $\langle \ldots \rangle_C$ represents a Monte Carlo average taking place over the various configurations of site-energy disorder. The dimensionless vector $\boldsymbol{r}$ runs over all monomer-monomer separation vectors within the stack.

In paracrystalline π-stacks, the π-stacking distance between polymer chains varies around some equilibrium value d. The paracrystallinity parameter *g* is defined as σ_d/d where σ_d is the standard deviation of π-stacking distances. In these stacks the interchain coupling between chain n and chain n+1 is given by $t_{inter}(n) = t_{inter}^0 \exp(-\beta \Delta d_n)$ where Δd_n is the deviation from the equilibrium distance d and is selected from a Gaussian distribution. t_{inter}^0 is the coupling when $\Delta d_n = 0$. The paracrystalline

disorder model and the diagonal disorder model are discussed in greater detail in previous work.[4,6]

Figure 5-1 shows *C*I for a π-stack consisting of 8 chains with 8 thiophene rings per chain with several levels of paracrystalline disorder (i.e. off-diagonal disorder as discussed above).

Figure 5-1

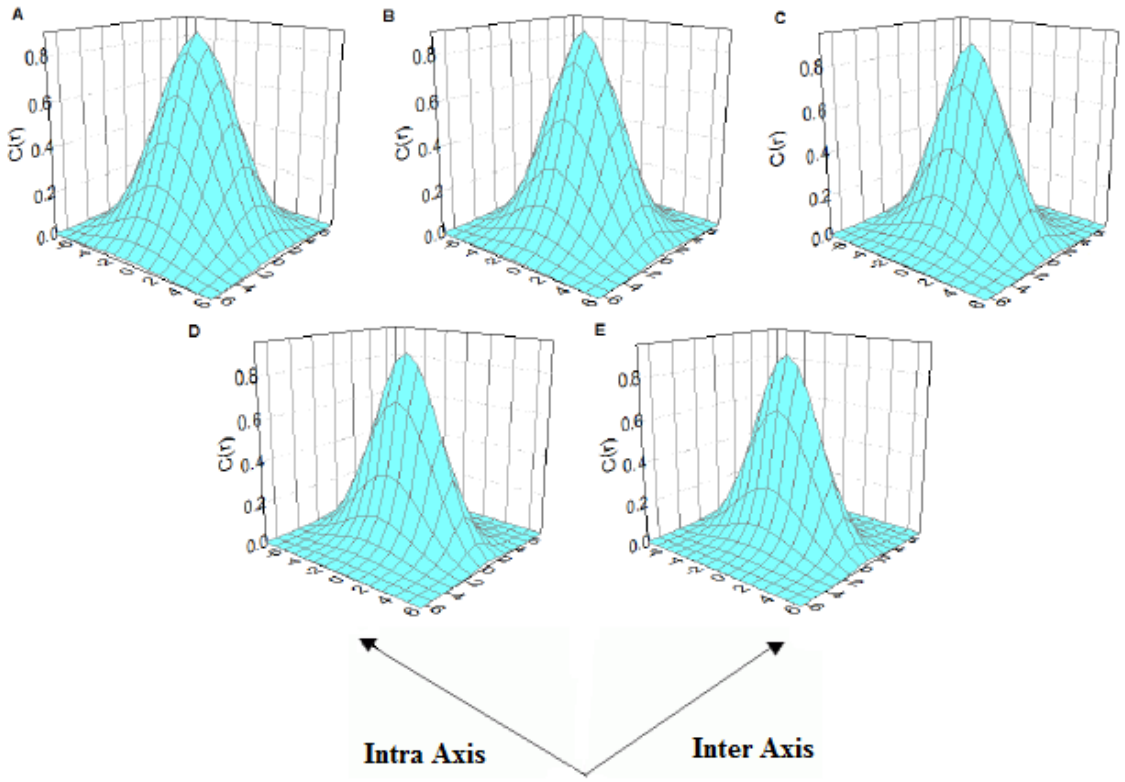

Figure 5-1 A-E shows the coherence functions of an 8x8 π-stack, with the paracrystallinity parameter g increasing from 0.02 in A to .1 in E, in increments of 0.02. t_{intra} = 0.3 eV and t_{inter} =0.1 eV. In addition, the vibronic energy was set to, $\hbar\omega_{vib} = 0.17\,\text{eV}$, corresponding to the aromatic-quinoidal stretching mode in P3HT, and the Huang-Rhys factor, λ^2, was set to unity. (see Ref.[8] for further discussion of the parameters). Hence, the nuclear relaxation energy upon hole formation on a given thiophene unit, $\lambda^2\hbar\omega_{vib}$, is also 0.17 eV. 2.4 was used for the value of β.[9]

Within the 8x8 "square" π-stack both *x* (intra) and *y* (inter) range from -7 to 7, in units of $d = 0.38$ nm. One can evaluate the total number of monomeric units, N_{coh} , within the coherence "area". This is referred to as the coherence number, and it is a way to measure the extent of delocalization of the hole. The formal definition of the coherence number is as follows:

$$N_{coh} = C(0)^{-1} \sum_{\boldsymbol{r}} \left| C(\boldsymbol{r}) \right| \tag{5-7}$$

In the data shown in Figure 5-1, the total coherence number N_{coh} drops from 45 to 27 when the paracrystallinity increases from g= 0.02 to 0.1 reflecting an associated increase in localization. The localization is almost entirely restricted to the interchain coordinate; the interchain coherence length decreases from 21 angstroms to 11 angstroms as the paracrystallinity increases through the same range of g values. Conversely, the intrachain coherence length remains roughly constant 23 Angstroms, which is the maximum value allowed for open boundary conditions and no intrachain disorder. The diminishing coherence number with increasing paracrystallinity is to be expected, since disorder leads to localization; in the limit of infinite disorder, the coherence function becomes a delta function. In Fig. 5-1 the disorder exists entirely along the interchain axis of the 2-dimensional system, and so the intrachain coherence length hardly changes at all as the paracrystallinity varies.

5-5 Ground State Polarons of Real Systems

In chapter 4 we used the Hamiltonian and basis states used in this chapter to reproduce the charge modulation spectra (CMS) of three P3HT films of different molecular weights, and preparation methods. By using the same disorder models and parameters that reproduced the experimental CMS spectra, we produce in Fig. 5-2 the coherence functions for the polaron ground states in the three systems. The coherence functions presented in Fig. 5-2 are quite different from each other, which is a result of the experimental samples having quite different morphologies. The experimental films ranged from high molecular weight (MW) and low disorder (Fig. 5-2A), to low MW and high disorder (Fig. 5-2B)[7]. Figure 5-2C is the coherence function of a hole in a low-disorder film for which the molecular weight was not reported.[8] See chapter 4 for more details concerning the disorder models and parameters used for the different thin film samples.

Interestingly, the interchain coherence lengths are larger than the intrachain coherence lengths in low disorder, high MW systems. In our model, the direct reason for this is the inhomogeneous diagonal site energy disorder, which varies along a chain but not between chains. In other words, our model indicates that in low disorder P3HT films, the structure can be described by a collection of disordered chains in which the disorder is correlated over at least 5 chains. Note that for the low molecular weight, high disorder film, the disorder did

Figure 5-2

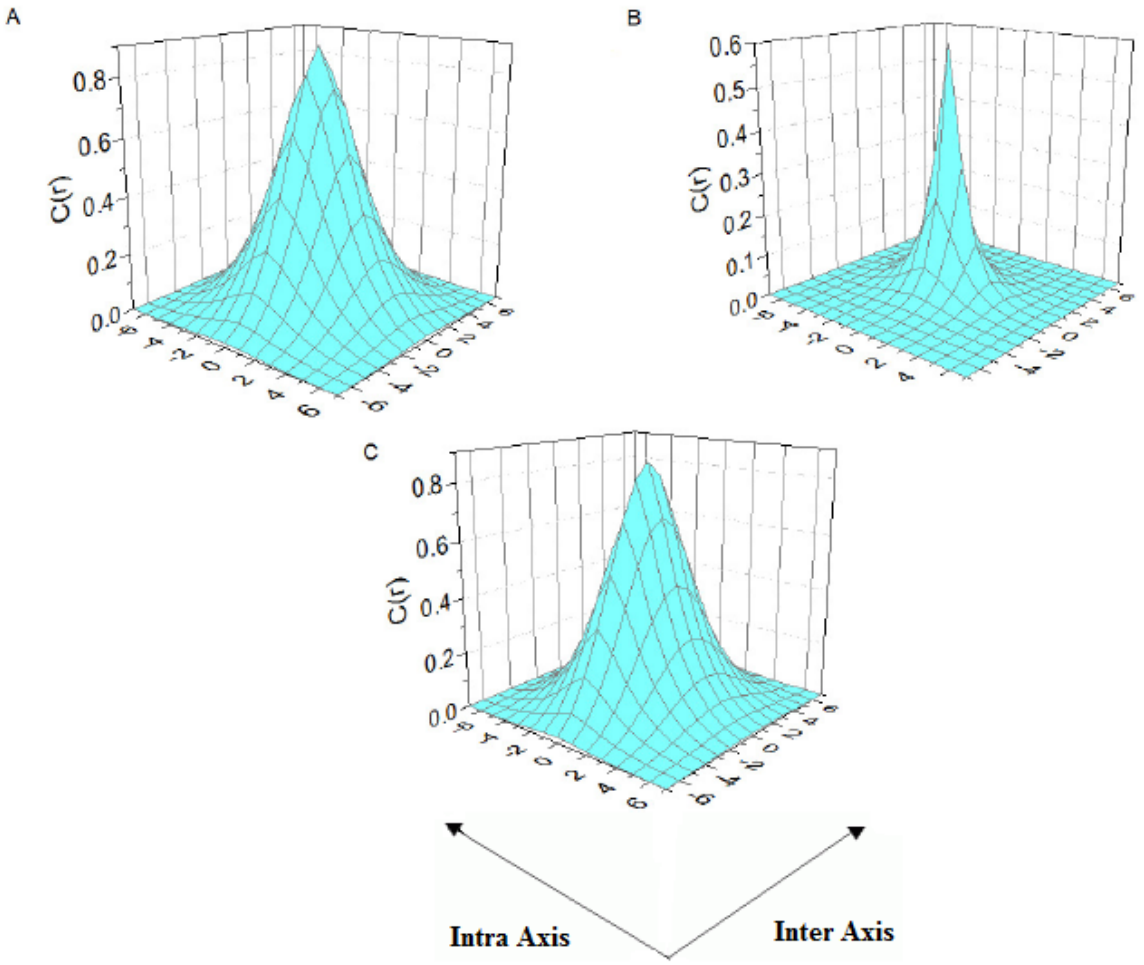

Figure 5-2A depicts the coherence function of a hole in a high MW, 37 kiloDaltons (kD), and low disorder system. Its interchain and intrachian coherence lengths are 20 and 18 angstroms, respectively. Figure 5-2B depicts the coherence function of a hole in a low MW, 15 KD, and high disorder system. Its interchain and intrachain coherence lengths are 4.5 and 7 angstroms, respectively. Figure 5-2C depicts the coherence function of a hole in P3HT thin film that had an unreported MW, and a low amount of disorder compared to the film in 5-2B. Its interchain and intrachian coherence lengths are 23 and 15 angstroms, respectively.

not have a directional component and was isotropic and the coherence lengths were much smaller.

Intrachain disorder can be caused by torsional disorder along the polymer backbone, polarization of the molecule due to the surrounding environment, and other nearby charges not explicitly included in our simulations. The CMS spectra of these films confirm that the coherence length is longer in the inter-direction (compared to the intra-direction) in high MW films. This is evident in the larger DP_1 peak compared with the P_1 peak found in the CMS spectrum.

5-6 Excited State Polarons

In a previous work[6], we reproduced the so called first delocalized polaron (DP_1) transition in the CMS spectra of P3HT thin films. It is called the delocalized polaron transition because it is a transition that pushes the hole from one polymer chain to another chain (delocalization) rather than moving it along only one chain, which is called simply the polaron or P_1 transition. The DP_1 transition and its interchain origin was identified by Vardeny et al.[8] from their induced transient absorption experiments. In our previous work, we identified the specific eigenstate that was responsible for the appearance of this DP_1 peak, and showed, using polarized spectra, that it did indeed have an interchain origin. The DP_1 peak and the eigenstate responsible for it lie at a relatively low energy above the ground state, because the interchain coupling. Figure 5-3 depicts the coherence functions of the hole eigenstate responsible for the DP_1 transition, for the three systems that were presented in figure 5-2, in the same order.

As with the ground state polarons in Figure 5-2, the interchain coherence lengths are larger than the intrachain coherence lengths in low disorder, high MW systems. Interestingly, we now see nodes and negative values along the interchain axes in the

simulations where the low-disorder model was used. The direct reason for this is the non-isotropic disorder used for the low disorder system (i.e. diagonal site energy disorder within a chain, with the same disordered chain repeating itself). The negative dips do not appear in Figure 5-3B because that figure was generated using an isotropic disorder model. Interestingly, in all three cases, the coherence numbers along each axis were very similar to the coherence numbers for the ground state polarons in Figure 5-2, despite these new features.

5-7 Discussion and Conclusion

We have studied the coherence functions of holes in real P3HT thin films as well as purely theoretical systems. Coherence functions are of particular importance for solar cell materials because they are directly related to charge mobility. The paracrystallinity that exists in real systems has been incorporated into our model, and we have shown, predictably, that it acts to localize charges along the interchain π-stacking axis. In the same series we showed that interchain paracrystallinity has practically no effect on the intrachain coherence number. Intrachain paracrystallinity also exists, though it was not used in our models nor thought to be significant for P3HT.

Next we examined the ground state polarons of some real systems for which we had already found the appropriate parameters in a previous work[6]. Interestingly, we found that the coherence lengths along the interchain direction were greater for ordered systems than the intrachain coherence lengths.

Figure 5-3

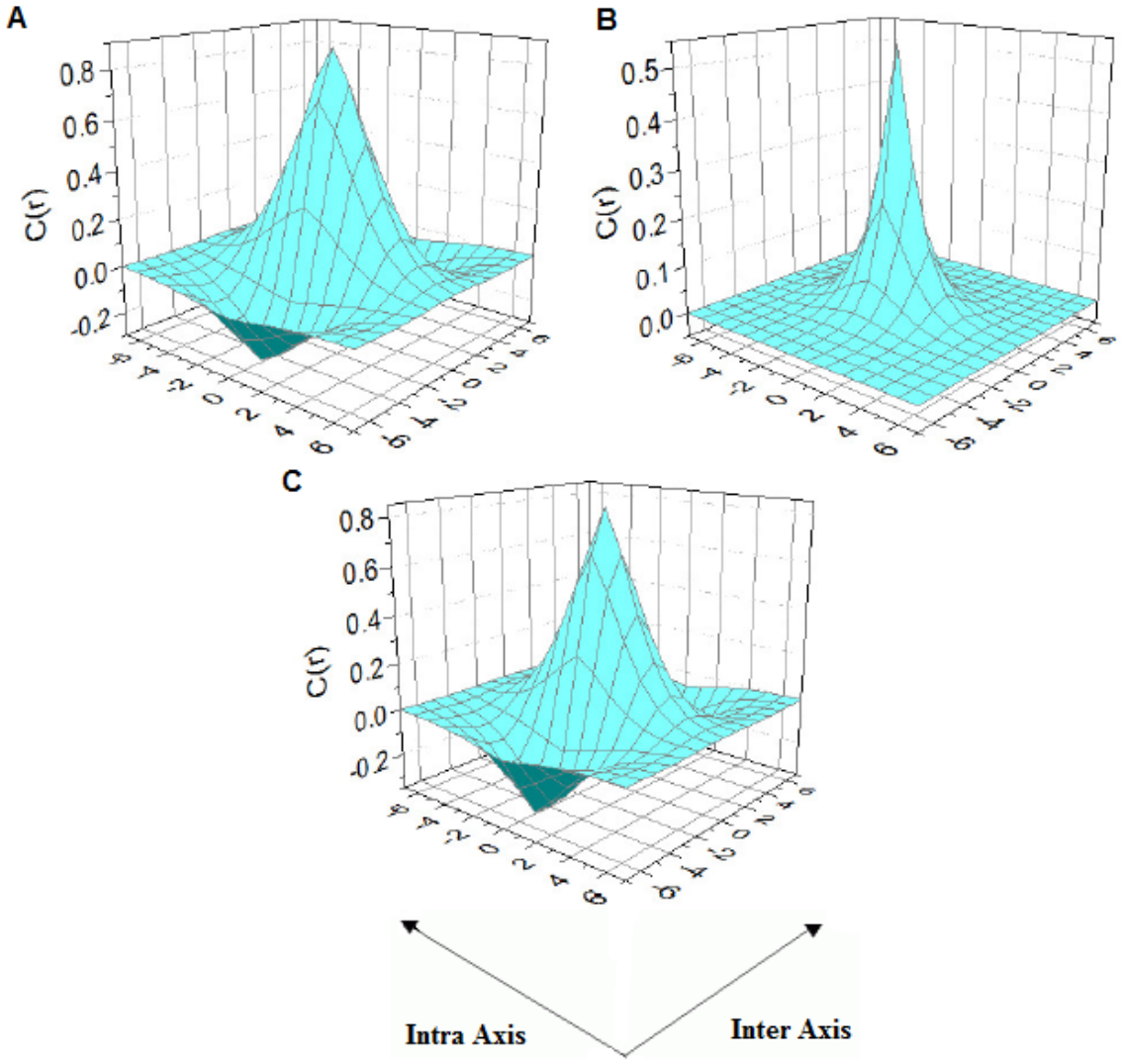

Figure 5-3A depicts the coherence function of a hole in a high MW, 37 kD, and low disorder system. Its interchain and intrachian coherence lengths are 20.4 angstroms and 17.6 angstroms, respectively. Figure 5-3B depicts the coherence function of a hole in a low MW, 15 KD, and high disorder system. Its interchain and intrachain coherence lengths are 6.7 and 9.31 angstroms, respectively. Figure 5-2C depicts the coherence function of a hole in P3HT thin film that had an unreported MW, and a low amount of disorder compared to the film in 5-2B. . Its interchain and intrachain coherence lengths 23 and 15 angstroms, respectively.

This is supported by the experimental CMS spectra, which display a larger peak for the DP_1 interchain transition as compared to the P_1 intrachain transition. We also showed that high disorder films have a lower coherence length, consistent with a measured lower mobility,[1] as was expected. It was also shown that intrachain coherence lengths are larger than interchain coherence lengths in low MW P3HT, where paracrystallinity is not present, and disorder comes entirely from site energy diagonal disorder.

Finally, we examined the coherence functions of the polaron eigenstates responsible for the DP_1 transition in CMS spectra. We found that in more ordered films, which exhibit a non-isotropic distribution of diagonal site energies, the coherence function of the DP_1 state has negative dips along the interchain axis, but still has approximately the same inter- and intrachain coherence lengths as the corresponding ground state polarons. Negative dips were not present for the low MW P3HT polaron, because an isotropic disorder model was used for that film, but the coherence numbers were still very similar to those of the ground state polaron in the same system. These are theoretical extremes, in reality the disorder may not be completely non-isotropic in high MW films, and may not be completely isotropic in low molecular weight films, but the approximation used here is that they are, in order to simplify the model and to cut down on the size of the phase space of the adjustable parameters.

We have shown that holes in P3HT films are delocalized over a significantly large number of thiophene sites, both in the interchain and intrachain directions. When combined with the results of our previous work,[6] the present results show that the intensity of CMS spectral transitions are proportional to the coherence lengths of both the initial and final states of the hole. We found that the coherence lengths of hole type

polarons to be 10-20 Angstroms, along both the inter- and intrachain axes, depending on the molecular weight and amount of disorder in the sample. In this way, CMS can be used as a probe of the mobility of the hole, that is sensitive to inter- and intrachain directional mobility.

REFERENCES

1. Chang, J.-F.; Sirringhaus, H.; Giles, M.; Heeney, M.; & McCulloch, I. Phys. Rev. B 2007, **76**, p. 205204.

2. Kaake, L. G.; Moses, D.; Heeger, A. J. Phys. Chem Lett. 2013, **4** (14), p. 2264-2268.

3. Niklas, J.; Mardis, L. K.; Banks, B. P.; Grooms, G. M.; Sperlich, A.; Dyakonov, V.; et al. Phys. Chem. Chem. Phys. 2013, **15**(24), p. 9562-9574.

4. Osterbacka, R.; An, C.; Jiang, X.; Vardeny, Z. Science 2000, **287**, p. 839.

5. Paqyub, F.; Yamagata, H.; Hestand, N.; Sakowicz, M.; Berube, M. C.; Reynolds, L.; et al. Phys. Rev. B 2013, p. 155202.

6. Pochas, C. M. & Spano, F. C. J. Chem. Phys. 2014, **140**, p. 244902.

7. Pochas, C. M.; Yamagata, H.; Spano, F. SPIE Proceedings *2014*.

8. Yamagata, H., & Spano, F. J. Chem Phys. 2012, **136**(18), p. 184901.

9. Rivnay, J.; Noriega, R.; Northrup, J. E.; Kline, R. J.; Toney, M. F.; Salleo, A. Phys. Rev. B 2011, **83**(12), p. 121306.

10. Niklas, J.; Mardis, K. L.; Banks, B. P.; Grooms, G. M.; Sperlich, A.; Dyakonov, V.; Beaupre, S.; Leclerc, M.; Xu, T.; Yu, L.; Poluektov, O. G. Phys. Chem. Chem. Phys. 2013, 15, 9562−9574.

CHAPTER 6

SUMMARY AND OUTLOOK

The attention received by organic electronics from both academia and industry will only increase in the coming years. As it does, so too will the demand for a better understanding of the physical properties of electronic excitations in these systems. In furthering our understanding of those properties, we investigated a robust variety of small PDI aggregates without any disorder, and showed that in that limit the model quantitatively reproduces relevant observables such as absorption and emission spectra. A few of these aggregates constituted classical J-aggregates as first described by E.E. Jelley,[1] even though they were in fact covalently bound oligomers. We extended these insights to a two-dimensional model of hole states in P3HT, used in solar devices,[2-6] and were able to reproduce the charge modulation spectra (CMS) of hole type polarons. In the course of our polaron analysis we also provided insight into using CMS as a probe for polaron coherence length.

We began with a detailed study of a bent PDI dimer that exhibited both H- and J-aggregate signatures in its absorption spectrum. The coupling between the chromophores in this dimer was calculated using a novel method which sums up the interaction of Mullikan charges on all the various atoms. This highly accurate method of calculating the Coulombic coupling between two chromophores allowed us to use the Holstein Hamiltonian and one- and two-particle states to faithfully reproduce the absorption and emission spectra of the dimer system. Because the transition dipoles of the chromophores were not entirely parallel, nor entirely ant-parallel, its spectra had two polarization components, one which could be resolved and shown to be purely J- like,

and one which was purely H-like. This H- and J- aggregate behavior together in one aggregate of just two chromophores gives a unique insight into the photophysics of aggregated conjugated molecules in organic electronics. Our dimer studies can be viewed as a launching point for more advanced studies addressing more complex morphologies in the organic solid state.

Next we applied the same methods to a variety of small covalently bound PDI aggregates. These aggregates were divided into two series, a star shaped symmetric series, and a linear series. We showed that the linear series displayed the spectral signatures of a classical J-aggregate, and more generally we showed that covalently bound repeat units in a polymer or oligomer may be regarded as single molecules in a J-aggregate. The notion that a single polymer chain can be a J-aggregate has been explored in other works from this group as well.[7] The symmetric series could not be classified in terms of simple H- or J-aggregate terms, as its spectral signatures were more complex. Nevertheless, our model reproduced those spectral signatures with a very high degree of accuracy. This shows that our model is quantitative and accurate in the limit of a well-known system with no disorder.

With the knowledge and confidence gained from these studies, we moved on to a more practical application and studied the CMS of hole type polarons in P3HT thin films. The properties of these films can vary widely depending on a number of factors[8] including the solvent used in film preparation, the temperature and amount of time used in forming the film, as well as molecular properties such as the molecular weight of the P3HT. By reproducing the CMS of these systems, we were able to gain a great deal of insight into the nature of the molecular disorder in these thin P3HT films. The diagonal

disorder arises due to changes in the diagonal energy of a hole on a site due to the polarizing environment around that particular site. The off-diagonal disorder results from random fluctuations in the interchain distances in these films, also known as paracrystallinity, which changes the value of the interchain hole transfer integral. We found that in high MW films, paracrystallinity was important and the diagonal disorder was strongly correlated between chains, but not within a chain. For low MW, we found that paracrystallinity was not present and that the diagonal disorder was not correlated with a chain nor between chains. This shows that CMS is a good probe for the disorder in P3HT thin films.

Finally we used the parameters obtained in chapter 5 to generate the coherence functions of polarons in a 2D π-stack of P3HT molecules. We found that a higher intensity in the CMS (or induced transient absorption) meant a larger coherence length of both ground state and excited polarons in the film. Predictably, we also found that higher disorder in a particular direction in the π-stack led to a lower coherence length along that direction in the stack. This study also showed that CMS is not only a good probe for the coherence length of a polaron, but that, in P3HT, it has directional specificity. The intensity of the narrow low energy peak indicates the coherence length between chains, while the intensity of the broad high energy peak indicates the coherence length within a chain. The reason for this is that interchain coupling is weaker than intrachain coupling, and so the two peaks are placed at different energies. Since most polymer films have a stronger intrachain coupling than an interchain coupling, it is likely that CMS will exhibit this directional specificity in other systems as well.

Throughout this writing, we have developed theoretical models to better understand the photophysics of π-conjugated aggregates, such as small covalently bound complexes and thin films of polymers. We successfully explained some of the fundamental properties of these materials, such as superradiance, disorder, and coherence length, in terms of well-established ideas like J- and H-aggregation. Still there are challenges to be overcome. One such challenge is to be able to advise and guide new materials research to find ways to improve existing devices. One new avenue of research currently being explored is the time-dependent dynamics of excitation in π-conjuagted aggregates. Preliminary dynamics calculations are already giving us insight into the speed of excitations in these aggregates, which determines current in photovoltaic device, and has yielded insights into new phenomena, such as the interference between the Coulombic coupling and orbital overlap coupling of two nearest neighbor molecules. Ultimately, our goal is to account for the photophysical properties of a wide range of conjugated polymers, crystals, covalently bound complexes, and any other kind of organic electronic system.

In conclusion, my thesis research has accomplished the following: analysis of a bent PDI dimer wherein a novel method for calculating the Coulombic coupling was employed, and spectra were reproduced with quantitative accuracy. An analogy was used to explain Davydov splitting in terms of H and J aggregation. Investigation of a variety of small PDI aggregates was carried out, including a linear series and a star-shaped symmetric series. We showed that our model is quantitatively accurate for all these different systems, and also showed that a linear arrangement of covalently bound chromophores behaves like a classical J-aggregate. We successfully reproduced the

charge modulation spectra of a variety of P3HT thin films, which allowed us to gain insight into the nanoscale disorder in the films, and allowed us to characterize the differences in disorder between low molecular weight films, and high molecular weight films. Finally, we calculated the coherence functions and coherence lengths of polarons in P3HT π-stacks. We found that the coherence lengths of hole type polarons to be 1-2 nm, along both the inter- and intrachain axes, depending on the molecular weight and amount of disorder in the sample. In doing so we showed that CMS and induced transient absorption are useful probes for the coherence lengths of polarons in P3HT, and they allow for selective probing of both the intrachain and interchain coherence lengths separately.

REFERENCES

1. Jelley, E.E, Nature, 1936 **138**, p. 1009-1010.

2. Liang, Y.Y. and L.P. Yu, Accounts of Chemical Research, 2010. **43**(9): p. 1227-1236.

3. Yu, G., et al., Science, 1995. **270**: p. 1789-1791.

4. Yang, X. and J. Loos, Macromolecules, 2007. **40**(5): p. 1353-1362.

5. Granstrom, M., et al., Nature, 1998. **395**: p. 257-260.

6. Kim, Y., et al., Nature Materials, 2006. **5**(3): p. 197-203.

7. Yamagata, H., & Spano, F. J. Chem Phys. 2012, **136**(18), p. 184901.

8. Stingelin, N., et al. Macromolecules, 2014, **47** (19), pp 6730–6739.

BIBLIOGRAPHY

Chaper 1 References

1. Shirakawa, H., et al., Journal of the Chemical Society-Chemical Communications, **1977**(16): p. 578-580.

2. Burroughes, J.H., et al., Nature, 1990. **347**: p. 539-541.

3. Sirringhaus, H., et al., Nature, 1999. **401**(6754): p. 685-688.

4. Coakley, K.M. and M.D. McGehee, Chemistry of Materials, 2004. **16**(23): p. 4533-4542.

5. Scholes, G.D. and G. Rumbles, Nature Materials, 2006. **5**(9): p. 683-696.

6. Heeger, A.J., Chemical Society Reviews, 2010. **39**(7): p. 2354-2371.

7. Bredas, J.-L., et al., Acc. Chem. Res., 2009. **42**(11): p. 1691-1699

8. Malliaras, G. and R.H. Friend, Physics Today, 2005. **58**(5): p. 53-58.

9. Bao, Z., A. Dodabalapui, and A.J. Lovinger, Appl. Phys. Lett., 1996. **69**: p. 4108-4110.

10. Sirringhaus, H., N. Tessler, and R.H. Friend, Science, 1998. **280**: p. 1741-1744.

11. Tsumura, A., H. Koezuka, and T. Ando, Appl. Phys. Lett., 1986. **49**: p.1210-1212.

12. Zen, A., et al., Adv. Funct. Mater., 2004. **14**: p. 757-764.

13. Bao, Z., Adv. Mater., 2000. **12**: p. 227-230.

14. Mullen, K. and U. Scherf, eds. 2006, Wiley: New York.

15. Friend, R.H., et al., Nature, 1999, **397**: p. 121-128.

16. Z.H. Kafafi Proceedings of SPIE. 2002, **4464** Washington: Society of Photo-optical Instrumentation Engineers.

17. Adachi, C., et al., J. Appl. Phys., 2001. **90**: p. 5048-5052.

18. Liang, Y.Y. and L.P. Yu, Accounts of Chemical Research, 2010. **43**(9): p. 1227-1236.

19. Yu, G., et al., Science, 1995. **270**: p. 1789-1791.

20. Yang, X. and J. Loos, Macromolecules, 2007. **40**(5): p. 1353-1362.

21. Granstrom, M., et al., Nature, 1998. **395**: p. 257-260.

22. Kim, Y., et al., Nature Materials, 2006. **5**(3): p. 197-203.

23. Kim, J.Y., et al., Science, 2007. **317**(5835): p. 222-225.

24. Brabec, C.J., Solar Energy Materials and Solar Cells, 2004. **83**(2-3): p. 273-292.

25. Brabec, C.J., et al., 2003, Heidelberg: Springer.

26. Stingelin, N., et al., 2014, **47** (19), pp 6730–6739

27. Niles, E.T., et al., J. Phys. Chem. Lett., 2012. **3**(2): p. 259-263.

28. Kistler, K.A.; Pochas, C.M.; Yamagata, H.; Matsika, S.; Spano, F.C. Journal of Physical Chemistry B, 2012, **116** (1): p. 77-86

29. Pochas, C.M.; Kistler, K.A.; Yamagata H.; Spano, F.C. Journal of The Amercian Society, 2013, **135**, 8, p. 3056-3066.

30. Spano, FC.; Yamagata, H. Journal of Physical Chemistry B, 2011, **115** (18) p. 5133-5143.

31. Jelley, E.E, Nature, 1936 **138**, p. 1009-1010.

32. Kaiser, T. E.; Stepanenko, V.; Wurthner, F. J. Am. Chem. Soc. 2009, **131**, p. 6719-6732.

33. Ghosh, S.; Li, X.-Q.; Stepanenko, V.; Wurthner, F. Chem.—Eur. J. 2008, **14**, p. 11343–11357.

34. Shaller, A. D.; Wang, W.; Gan, H. Y.; Li, A. D. Q. Angew. Chem., Int. Ed. 2008, **47**, p. 7705–7709.

35. Rybtchinski, B.; Sinks, L. E.; Wasielewski, M. R. J. Phys. Chem A 2004, **108**, p. 7497.

36. Veldman, D.; Chopin, S. M. A.; Meskers, S. C. J.; Groeneveld, M. M.; Williams, R. M.; Janssen, R. A. J. J. Phys. Chem A 2008, **112**, p. 5846.

37. Giaimo, J.M.; Lockard, J. V.; Sinks, L. E.; Scott, A. M.;Wilson, T. M.; Wasielewski, M. R. J. Phys. Chem. A 2008, **112**, p. 2322.

38. Schlosser, F.; Sung, J.; Kim, P.; Kim, D.; Wurthner, F. Chem. Sci. 2012, **3**, p.

2778.

39. Montgomery, N. A.; Hedley, G. J.; Ruseckas, A.; Denis, J.-C.; Schumacher, S.; Kanibolotsky, A. L.; Skabara, P. J.; Galbraith, I.; Turnbull, G. A.; Samuel, I. D. W. Phys. Chem. Chem. Phys. 2012, **14**, p. 9176.

40. Metivier, R.; Nolde, F.; Mullen, K.; Basche, T. Phys. Rev. Lett. 2007, **98**, p. 047802.

41. Yoo, H.; Furumaki, S.; Yang, J.; Lee, J.-E.; Chung, H.; Oba, T.; Kobayashi, H.; Rybtchinski, B.; Wilson, T. M.; Wasielewski, M. R.; Vacha, M.; Kim, D. J. Phys. Chem. B 2012, **116**, p. 12878.

42. Yamagata, H., & Spano, F. J. Chem Phys. 2012, **136**(18), p. 184901.

Chaper 2 References

1. Hochstrasser, R. M.; Kasha, M. Photochem. Photobiol. 1964, **3**, p. 317–331.

2. Kasha, M. Radiat. Res. 1963, **20**, p. 55–70.

3. McRae, E. G.; Kasha, M. J. Chem. Phys. 1958, **28**, p. 721–722.

4. Spano, F. C. J. Am. Chem. Soc. 2009, **131**, p. 4267–4278.

5. Spano, F. C.; Clark, J.; Silva, C.; Friend, R. H. J. Chem. Phys. 2009, **130**, p. 074904.

6. Clark, J.; Silva, C.; Friend, R. H.; Spano, F. C. Phys. Rev. Lett. 2007, **98**, p. 206406.

7. Spano, F. C. Acc. Chem. Res. 2010, **43**, p. 429–439.

8. Langhals, H.; Hofer, A.; Bernhard, S.; Siegel, J. S.; Mayer, P. J. Org. Chem. 2011, **76**, p. 990–992.

9. Kaiser, T. E.; Stepanenko, V.; Wurthner, F. J. Am. Chem. Soc. 2009, **131**, p. 6719 6732.

10. Ghosh, S.; Li, X.-Q.; Stepanenko, V.; Wurthner, F. Chem.—Eur. J. 2008, **14**, p. 11343–11357.

11. Shaller, A. D.; Wang, W.; Gan, H. Y.; Li, A. D. Q. Angew. Chem., Int. Ed. 2008, **47**, p. 7705–7709.

12. Langhals, H.; Gold, J. Liebigs Ann./Rec. 1997, p. 1151–1153.

13. Giaimo, J. M.; Lockard, J. V.; Sinks, L. E.; Scott, A. M.; Wilson, T. M.; Wasielewski, M. R. J. Phys. Chem. A 2008, **112**, p. 2322–2330.

14. Veldman, D.; Chopin, S. M. A.; Meskers, S. C. J.; Groeneveld, M. M.; Williams, R. M.; Janssen, R. A. J. J. Phys. Chem. A 2008, **112**, p. 5846–5857.

15. Kawai, T.; Kawamura, K.; Tsumatori, H.; Ishikawa, M.; Naito, M.; Fujiki, M.; Nakashima, T. Chem Phys Chem 2007, **8**, p. 1465–1468.

16. Tsumatori, H.; Nakashima, T.; Kawai, T. Org. Lett. 2011, **12**, p. 2362–2365.

17. Wang, W.; Shaller, A. D.; Li, A. D. Q. J. Am. Chem. Soc. 2008, **130**, p. 8271–8279.

18. Zeidan, T. A.; Hariharan, M.; Siegmund, K.; Lewis, F. D. Photochem. Photobiol. Sci. 2010, **9**, p. 916–922.

19. Hariharan, M.; Zheng, Y.; Long, H.; Zeidan, T. A.; Schatz, G. C.; Vura-Weis, J.; Wasielewski, M. R.; Zuo, X.; Tiede, D. M.; Lewis, F. D. J. Am. Chem. Soc. 2009, **131**, p. 5920–5929.

20. Zheng, Y.; Long, H.; Schatz, G. C.; Lewis, F. D. Chem. Commun. 2005, p. 4795–4797.

21. Witkowski, A.; Moffitt, W. J. Chem. Phys. 1960, **33**, p. 872–875.

22. Fulton, R. L.; Gouterman, M. J. Chem. Phys. 1961, **35**, p. 1059.

23. Fulton, R. L.; Gouterman,M. J. Chem. Phys. 1964, **41**, p. 2280–2286.

24. Weigang, O. E. J. Chem. Phys. 1965, **43**, p. 3609.

25. Weigang, O. E. J. Chem. Phys. 1965, **43**, p. 71.

26. Seibt, J.; Marquetand, P.; Engel, V.; Chen, Z.; Dehm, V.; Wurthner, F. Chem. Phys. 2006, **328**, p. 354–362.

27. Fink, R. F.; Seibt, J.; Engel, V.; Renz,M.; Kaupp,M.; Lochbrunner, S.; Zhao, H. M.; Pfister, J.;Wurthner, F.; Engels, B. J. Am. Chem. Soc. 2008, **130**, p. 12858.

28. Guthmuller, J.; Zutterman, F.; Champagne, B. J. Chem. Phys. 2009, **131**, p. 154302.

29. Gao, F.;Zhao, Y.; Liang,W. J. Phys.Chem. B 2011, **115**, p. 2699–2708.

30. Hoffmann, M.; Soos, Z. G. Phys. Rev. B 2002, **66**, p. 024305.

31. Heinemeyer, U.; Scholz, R.; Gisslen, L.; Alonso, M. I.; Osso, J. O.; Garriga, M.; Hinderhofer, A.; Kytka, M.; Kowarik, S.; Gerlach, A.; Schreiber, F. Phys. Rev. B 2008, **78**, p. 085210.

32. Davydov, A. S. Theory of Molecular Excitons; Plenum Press: New York, 1971.

33. Agranovich, V. M. Excitations in Organic Solids; Oxford University Press: New York, 2009.

34. Spano, F. C.; Yamagata,H. J. Phys. Chem. B 2011, **115**, p. 5133–5143.

35. Holstein, T. Ann. Phys. 1959, **8**, p. 325–342.

36. Wong, C. Y.; Curutchet, C.; Tretiak, S.; Scholes, G. D. J. Chem. Phys. 2009, **130**, p. 081104.

37. Chang, J. C. J. Chem. Phys. 1977, **67**, p. 3901.

38. Patwardhan, S.; Sengupta, S.; Wurthner, F.; Siebbeles, L. D. A.; Grozema, F. J. Phys. Chem. C 2010, **114**, p. 20834–20842.

39. Li, H.; Malinin, S. V.; Tretiak, S.; Chernyak, V. Y. J. Chem. Phys. 2010, **132**, p. 124103.

40. Dunning, T. H. J. Chem. Phys. 1989, **90**, p. 1007–1023.

41. Philpott, M. R. J. Chem. Phys. 1971, **55**, p. 2039–2054.

42. Spano, F. C. J. Chem. Phys. 2002, **116**, p. 5877–5891.

43. Roden, J.; Eisfeld, A.; Dvorak,M.; Bunermann,O.; Stienkemeier, F. J. Chem. Phys. 2011, **134**, p. 054907.

44. Zhao, J.-S.; Ruan, Y.-B.; R., Z.; Jiang, Y.-B. Chem. Sci. 2011, **2**, p. 937–944.

45. Spano, F. C. J. Chem. Phys. 2005, **122**, p. 234701.

46. Spano, F. C. Chem. Phys. 2006, **325**, p. 22–35.

47. Yamagata, H.; Spano, F. C. J. Chem. Phys. 2011, **135**, p. 054906.

48. Taliani, C.; Gebauer, W., Handbook of Oligo and Polythiophenes; Wiley-VCN: Weinheim, Germany, 1999.

49. Petelenz, P.; Andrzejak, M. Chem. Phys. Lett. 2001, **343**, p. 139–142.

50. Sun, X. H.; Zhao, Z.; Spano, F. C.; Beljonne, D.; Cornil, J.; Shuai, Z.; Bredas, J.-L. Adv. Mater. 2003, **15**, p. 818–821.

51. Meinardi, F.; Cerminara,M.; Sassella, A.; Borghesi, A.; Spearman, P.; Bongiovanni, G.; Mura, A.; Tubino, R. Phys. Rev. Lett. 2002, **89**, p. 157403-1–157403-4.

52. Spano, F. C. J. Chem. Phys. 2003, **118**, p. 981–994.

53. Spano, F. C. Annu. Rev. Phys. Chem. 2006, **57**, p. 217–243.

54. Muccini, M.; Schneider, M.; Taliani, C.; Sokolowski, M.; Umbach, E.; Beljonne, D.; Cornil, J.; Bredas, J. L. Phys. Rev. B 2000, **62**, p. 6296–6300.

55. Stradomska, A.; Kulig, W.; Slawik, M.; Petelenz, P. J. Chem. Phys. 2011, **134**, 224505.

56. Yamagata, H.; Norton, J.; Hontz, E.; Olivier, Y.; Beljonne, D.; Bredas, J. L.; Silbey, R. J.; Spano, F. C. J. Chem. Phys. 2011, **134**, p. 204703.

57. Clark, L. B.; Philpott, M. R. J. Chem. Phys. 1970, **53**, p. 3790–3801.

58. Ahn, T. S.; Muller, A. M.; Al-Kaysi, R. O.; Spano, F. C.; Norton, J. E.; Beljonne, D.; Bredas, J. L.; Bardeen, C. J. J. Chem. Phys. 2008, **128**, p. 054505.

59. Lim, S.-H.; Bjorklund, T. G.; Spano, F. C.; Bardeen, C. J. Phys. Rev. Lett. 2004, **92**, p. 107402.

Chapter 3 References

1. Kanibolotsky, A. L.; Perepichka, I. F.; Skabara, P. J. Chem. Soc. Rev. 2010, **39**, p. 2695.

2. Oldham, W. J.; Lachicotte, R. J.; Bazan, G. C. J. Am. Chem. Soc. 1998, **120**, p. 2987.

3. Robinson,M. R.;Wang, S.; Bazan, G. C.; Cao, Y. Adv.Mater. 2000, **12**, p. 1701.

4. Roncali, J.; Leriche, P.; Cravino, A. Adv. Mater. 2007, **19**, p. 2045.

5. Mangold, H. S.; Richter, T. V.; Link, S.; Wurfel, U.; Ludwigs, S. J. Phys. Chem. B 2011, **116**, p. 154.

6. Tretiak, S.; Chernyak, V.; Mukamel, S. J. Phys. Chem. B 1998, **102**, 3310.

7. Minami, T.; Tretiak, S.; Chernyak, V.;Mukamel, S. J. Lumin. 2000, **87**−9, p. 115.

8. Badaeva, E.; Harpham, M. R.; Guda, R.; Suzer, O.; Ma, C. Q.; Bauerle, P.; Goodson, T.; Tretiak, S. J. Phys. Chem. B 2010, **114**, p. 15808.

9. Lee, C. C.; MacKay, J. A.; Frechet, J. M. J.; Szoka, F. C. Nat. Biotechnol. 2005, **23**, p. 1517.

10. Crooks, R.M.; Zhao,M.Q.; Sun, L.; Chechik, V.; Yeung, L. K. Acc. Chem. Res. 2001, **34**, .p 181.

11. Wilson, T.M.; Tauber,M. J.;Wasielewski,M. R. J. Am. Chem. Soc. 2009, **131**, p. 8952.

12. Langhals, H. Helv. Chim. Acta 2005, **88**, p. 1309.

13. Langhals, H.; Jona, W. Angew. Chem., Int. Ed. 1998, **37**, p. 952.

14. Langhals, H.; Gold, J. J. Prakt. Chem./Chem.-Ztg. 1996, **338**, p. 654.

15. Langhals, H.;Wagner, C.; Ismael, R. New J. Chem. 2001, **25**, p. 1047.

16. Kaiser, T. E.; Stepanenko, V.; Wurthner, F. J. Am. Chem. Soc. 2009, **131**, p. 6719−6732.

17. Ghosh, S.; Li, X.-Q.; Stepanenko, V.;Wurthner, F. Chem. Eur. J. 2008, **14**, 11343−11357.

18. Shaller, A. D.; Wang, W.; Gan, H. Y.; Li, A. D. Q. Ang. Chem. Int. Ed. 2008, **47**, p. 7705.

19. Rybtchinski, B.; Sinks, L. E.; Wasielewski, M. R. J. Phys. Chem A 2004, **108**, p. 7497.

20. Veldman, D.; Chopin, S. M. A.; Meskers, S. C. J.; Groeneveld, M. M.; Williams, R. M.; Janssen, R. A. J. J. Phys. Chem A 2008, **112**, p. 5846.

21. Giaimo, J.M.; Lockard, J. V.; Sinks, L. E.; Scott, A. M.;Wilson, T. M.; Wasielewski, M. R. J. Phys. Chem. A 2008, **112**, p. 2322.

22. Schlosser, F.; Sung, J.; Kim, P.; Kim, D.; Wurthner, F. Chem. Sci. 2012, **3**, p. 2778.

23. Montgomery, N. A.; Hedley, G. J.; Ruseckas, A.; Denis, J.-C.; Schumacher, S.; Kanibolotsky, A. L.; Skabara, P. J.; Galbraith, I.; Turnbull, G. A.; Samuel, I. D. W. Phys. Chem. Chem. Phys. 2012, **14**, p. 9176.

24. Metivier, R.; Nolde, F.; Mullen, K.; Basche, T. Phys. Rev. Lett. 2007, **98**, p. 047802.

25. Yoo, H.; Furumaki, S.; Yang, J.; Lee, J.-E.; Chung, H.; Oba, T.; Kobayashi, H.; Rybtchinski, B.; Wilson, T. M.; Wasielewski, M. R.; Vacha, M.; Kim, D. J. Phys. Chem. B 2012, **116**, p. 12878.

26. Kistler, K. A.; Pochas, C. M.; Yamagata, H.; Matsika, S.; Spano, F. C. J. Phys. Chem. B 2011, **116**, p. 77.

27. Langhals,H.; Hofer, A.; Bernhard, S.; Siegel, J. S.;Mayer, P. J. Org. Chem. 2011, **76**, p. 990.

28. Kasha, M. Radiat. Res. 1963, **20**, p. 55.

29. Spano, F. C. Chem. Phys. 2006, **325**, p. 22.

30. Spano, F. C. Acc. Chem. Res. 2010, **43**, p. 429.

31. Clark, J.; Silva, C.; Friend, R.H.; Spano, F. C. Phys. Rev. Lett. 2007, **98**, p. 206406.

32. Spano, F. C. J. Am. Chem. Soc. 2009, **131**, p. 4267.

33. Spano, F. C. J. Chem. Phys. 2002, **116**, p. 5877.

34. Philpott, M. R. J. Chem. Phys. 1971, **55**, p. 2039.

35. Stradomska, A.; Petelenz, P. J. Chem. Phys. 2009, **131**, p. 044507.

36. Dunning, T. H. J. Chem. Phys. 1989, **90**, p. 1007.

37. Wong, C. Y.; Curutchet, C.; Tretiak, S.; Scholes, G. D. J. Chem. Phys. 2009, **130**, p. 081104.

38. Chang, J. C. J. Chem. Phys. 1977, **67**, p. 3901.

39. Patwardhan, S.; Sengupta, S.; Wurthner, F.; Siebbeles, L. D. A.; Grozema, F. J. Phys. Chem. C 2010, **114**, p. 20834.

40. Li, H.; Malinin, S. V.; Tretiak, S.; Chernyak, V. Y. J. Chem. Phys. 2010, **132**, p. 124103.

41. Guthmuller, J.; Zutterman, F.; Champagne, B. J. Chem. Phys. 2009, **131**, p. 154302.

42. Diehl, F. P.; Roos, C.; Jankowiak, H. C.; Berger, R.; Kohn, A.; Diezemann, G.; Basche, T. J. Phys. Chem B 2010, **114**, p. 1638.

43. Pope, M.; Swenberg, C. E. Electronic processes in organic crystals and polymers, 2nd ed.; Oxford University Press: New York, 1999; Vol. **56**.

44. Spano, F. C. J. Chem. Phys. 2005, **122**, p. 234701.

45. Spano, F. C.; Yamagata, H. J. Phys. Chem. B 2011, **115**, p. 5133−5143.

46. Gao, F.; Zhao, Y.; Liang, W. J. Phys. Chem. B 2011, **115**, p. 2699.

47. Zheng, Y.; Long, H.; Schatz, G. C.; Lewis, F. D. Chem. Commun. 2005, p. 4795−4797.

48. Fink, R. F.; Seibt, J.; Engel, V.; Renz, M.; Kaupp, M.; Lochbrunner, S.; Zhao, H. M.; Pfister, J.; Wurthner, F.; Engels, B. J. Am. Chem. Soc. 2008, 130, p. 12858.

Chapter 4 References

1. Braun, D. and Heeger, A. J. Appl. Phys. 1991, Lett. **58**(18), p. 1982–1984.

2. Sirringhaus, H.; Tessler, N.; Friend, R. H. Science 1998, **280**(5370), p. 1741–1744

3. Bredas, J.-L.; Norton, J. E; Cornil, J.; Coropceanu, V. Acc. Chem. Res. 2009, **42**(11), p. 1691–1699.

4. Ma, W. L.; Yang, C. Y.; Gong, X.; Lee, K.; Heeger, A. J. Adv. Funct. Mater. 2005, **15**(10), p. 1617–1622.

5. Brabec, C. J.; Gowrisanker, S.; Halls, J. J. M.; Laird, D.; Jia, S. J.; Williams, S. P. Adv. Mater. **22**(34), P. 3839–3856 (2010).

6. Brabec, C. J.; Sariciftci, N. S.; Hummelen, J. C. Adv. Funct. Mater. 2001, **11**(1), p. 15–26.

7. Bredas, J. L. and Street, G.B. Acc. Chem. Res. 1985, **18**(10), p. 309–315

8. Beljonne, D.; Cornil, J.; Sirringhaus, H.; Brown, P.J.; Shkunov, J. L.; Friend, R. H.; Bredas, J.L. Adv. Funct. Mater 2001, **11**(3), p. 229–234.

9. Gomes da Costa, P.; Dandrea, R. G.; Conwell, E. M. Phys. Rev. B 1993, **47**(4), p. 1800–1810.

10. Vogl, P. and Campbell, D. K. Phys. Rev. Lett. 1989, **62**(17), p. 2012–2015.

11. Noriega, R.; Rivnay, J.; Vandewal, K.; Koch, F. P. V.; Stingelin, N.; Smith, P.; Toney; M. F.; Salleo, A. Nat. Mater. 2013, **12**(11), p. 1038–1044.

12. Chang, J.-F.; Sirringhaus, H.; Giles, M.; Heeney, M.; McCulloch, I. Phys. Rev. B 2007, **76**, P. 205204.

13. Rivnay, J.; Noriega, R.; Northrup, J. E.; Kline, R. J.; Toney, M. F.; Salleo, A. Phys. Rev. B 2011, **83**(12), p. 121306.

14. McMahon, D. P.; Cheung, D. L.; Goris, L.; Dacuña, J.; Salleo, A.; Troisi, A. J. Phys. Chem. C 2011, **115**(39), p. 19386–19393.

15. Poelking, C. and Andrienko, D. Macromolecules 2013, **46**(22), p. 8941–8956.

16. Meisel, K. D.; Vocks, H.; Bobbert, P.A. Phys. Rev. B 2005, **71**(20), p. 6.

17. Fishchuk, I. I.; Kadashchuk, A.; Hoffmann, S. T.; Athanasopoulos, S.; Genoe, J.; Bassler, H.; Kohler, A. Phys. Rev. 2013, B **88**, 125202.

18. Osterbacka, R.; An, C. P.; Jiang, X. M.; Vardeny, Z. V. Science 2000, **287**, p. 839–842.

19. Jiang, X. M.; Osterbacka, R.; Korovyanko, O.; An, C. P.; Horovitz, B. ; Janssen, R. A. J.; Vardeny, Z.V. Adv. Funct. Mater. 2002, **12**(9), p. 587–597.

20. Chang, J. F.; Clark, J.; Zhao, N.; Sirringhaus, H.; Breiby, D. W.; Andreasen, J. W.; Nielsen, M. M.; Giles, M.; Heeney, M.; McCulloch, I. Phys. Rev. B 2006, **74**(11), p. 115318.

21. Sirringhaus, H.; Brown, P. J.; Friend, R. H.; Nielsen, M. M.; Bechgaard, K.; Langeveld-Voss, B. M. W.; Spiering, A. J. H.; Janssen, R. A. J.; Meijer, E. W.; Herwig, P.; de Leeuw, D. M. Nature 1999, **401**, p. 685.

22. Prosa, T. J.; Winokur, M. J.; McCullough, R. D. Macromolecules 1996, **29**, p. 3654–3656.

23. Prosa, T. J.; Winokur, M. J.; Moulton, J.; Smith, P.; Heeger, A. J. Macromolecules 1992, **25**, p. 4364–4372.

24. Piepho, S. B. J. Am. Chem. Soc. 1990, **112**(11), p. 4197–4206.

25. Piepho, S. B. J. Am. Chem. Soc. 1988, **110**(19), p. 6319–6326.

26. Piepho, S. B.; Krausz, E. R.; Schatz, P. N. J. Am. Chem. Soc. 1978, **100**(10), p. 2996–3005.

27. Creutz, C. and Taube, H. J. Am. Chem. Soc. 1969, **91**(14), p. 3988–3989.

28. Holstein, T. Ann. Phys. 1959, **8**, p. 325–342.
29. Philpott, M. R. J. Chem. Phys. 1971, **55**, p. 2039–2054.

30. Spano, F. C. J. Chem. Phys. 2002, **116**, p. 5877–5891.

31. Stradomska, A. and Petelenz, P. J. Chem. Phys. 2009, **131**(4), p. 044507.

32. Spano, F. C. J. Chem. Phys. 2005, **122**, p. 234701.

33. Spano, F. C. Chem. Phys. 2006, **325**, p. 22–35.

34. Clark, J.; Silva, C.; Friend, R. H.; Spano, F. C. Phys. Rev. Lett. 2007, **98**(20), p. 206406.

35. Yamagata, H and Spano, F. C. J. Chem. Phys. 2012, **136**(18), p. 184901
.
36. Paquin, F.; Yamagata, H.; Hestand, N. J.; Sakowicz, M.; Bérubé, N.; Côté, M.; Reynolds, L. X.; Haque, S. A.; Stingelin, N.; Spano, F. C.; Silva, C. Phys. Rev. B 2013, **88**(15), p. 155202.

37. Hush, N. S. Coord. Chem. Rev. 1985, **64**, p. 135–157.

38. Wu, M. W. and Conwell, E. M. Phys. Rev. B 1997, **56**(16), p. 10060–10062.

39. We note that tintra corresponds to the hole transfer between the local HOMO's of adjacent thiophene rings and is therefore substantially smaller than the value of approximately −2.5 eV between p-orbitals involved in a double bond. Since a single-ring HOMO is delocalized over four carbon p-orbitals, tintra should be less than about 1/4 of the p-orbital value, or about −0.6 eV.

40. Northrup, J. E. Phys. Rev. B 2007, **76**(24), p. 245202.

41. Wohlgenannt, M.; Jiang, X. M.; Vardeny, Z. V. Phys. Rev. B 2004, **69**(24), p. 4.

42. Mizes, H. A.; Conwell, E. Phys. Rev. Lett. 1993, **70**, p. 1505–1508.

43. Emin, D. Phys. Rev. B 1986, **33**, p. 3973–3975.

44 Hoffmann, S. T.; Bassler, H.; Kohler, A. J. Phys. Chem. B 2010, **114**(51), p. 17037–17048.

45. Bassler, H. Phys. Status Solidi B 1981, **107**, p. 9.

46. Beenken, W. J. D. Phys. Status Solidi A 2009, **206**(12), p. 2750–2756.
47. Coropceanu, V.; Cornil, J.; da Silva, D. A.; Olivier, Y.; Silbey, R.; Bredas, J. L.; Chem. Rev. 2007, **107**(4), p. 926–952.

48. Knapp, E. W. Chem. Phys. 1984, **85**, p. 73–82.

49. Spano, F. C.; Clark, J.; Silva, C.; Friend, R. H. J. Chem. Phys. 2009, **130**(7), p. 074904.

50. Brown, P. J.; Thomas, S. D.; Kohler, A.; Wilson, J. S.; Kim, J.S.; Ramsdale, C. M.; Sirringhaus, H.; Friend, R. H. Phys. Rev. B 2003, **67**, p. 064203.

51. Reid, O. G.; Pensack, R. D.; Song, Y.; Scholes, G. D.; Rumbles, G. Chem. Mater. 2014, **26**, p. 561.

52. Goh, C.; Kline, R. J.; McGehee, M. D.; Kadnikova, E. N.; Frechet, J. M. J. Appl. Phys. Lett. 2005, **86**(12), p. 122110.

53. Koch, F. P. V.; Rivnay, J.; Foster, S.; Müller, C.; Downing, J. M.; Buchaca-Domingo, E.; Westacott, P.; Yu, L; Yuan, M. J.; Baklar, M.; Fei, Z. P.; \ Luscombe, C.; McLachlan, M. A.; Heeney, M.; Rumbles, G.; Silva, C.; Salleo, A.; Nelson, J.; Smith, P.; Stingelin, N. Prog. Polym. Sci. 2013, **38**, p. 1978–1989.

Chapter 5 References

1. Chang, J.-F.; Sirringhaus, H.; Giles, M.; Heeney, M.; & McCulloch, I. Phys. Rev. B 2007, **76**, p. 205204.

2. Kaake, L. G.; Moses, D.; Heeger, A. J. Phys. Chem Lett. 2013, **4** (14), p. 2264-2268.

3. Niklas, J.; Mardis, L. K.; Banks, B. P.; Grooms, G. M.; Sperlich, A.; Dyakonov, V.; et al. Phys. Chem. Chem. Phys. 2013, **15**(24), p. 9562-9574.

4. Osterbacka, R.; An, C.; Jiang, X.; Vardeny, Z. Science 2000, **287**, p. 839.

5. Paqyub, F.; Yamagata, H.; Hestand, N.; Sakowicz, M.; Berube, M. C.;

Reynolds, L.; et al. Phys. Rev. B 2013, p. 155202.

6. Pochas, C. M. & Spano, F. C. J. Chem. Phys. 2014, **140**, p. 244902.

7. Pochas, C. M.; Yamagata, H.; Spano, F. SPIE Proceedings *2014*.

8. Yamagata, H., & Spano, F. J. Chem Phys. 2012, **136**(18), p. 184901.

9. Rivnay, J.; Noriega, R.; Northrup, J. E.; Kline, R. J.; Toney, M. F.; Salleo, A. Phys. Rev. B 2011, **83**(12), p. 121306.

10. Niklas, J.; Mardis, K. L.; Banks, B. P.; Grooms, G. M.; Sperlich, A.; Dyakonov, V.; Beaupre, S.; Leclerc, M.; Xu, T.; Yu, L.; Poluektov, O. G. Phys. Chem. Chem. Phys. 2013, 15, 9562−9574.

Chapter 6 References

1. Jelley, E.E, Nature, 1936 **138**, p. 1009-1010.

2. Liang, Y.Y. and L.P. Yu, Accounts of Chemical Research, 2010. **43**(9): p. 1227-1236.

3. Yu, G., et al., Science, 1995. **270**: p. 1789-1791.

4. Yang, X. and J. Loos, Macromolecules, 2007. **40**(5): p. 1353-1362.

5. Granstrom, M., et al., Nature, 1998. **395**: p. 257-260.

6. Kim, Y., et al., Nature Materials, 2006. **5**(3): p. 197-203.

7. Yamagata, H., & Spano, F. J. Chem Phys. 2012, **136**(18), p. 184901.

8. Stingelin, N., et al. Macromolecules, 2014, **47** (19), pp 6730–6739.